9-23-2021 11:00 AM

Inter-disciplinary Characterization of Streambed Heterogeneity and its Influence on Groundwater-Stream Water Interactions

Kyle Robinson, *The University of Western Ontario*

Supervisor: Robinson, Clare, *The University of Western Ontario*
: Power, Christopher, *The University of Western Ontario*

A thesis submitted in partial fulfillment of the requirements for the Master of Engineering Science degree in Civil and Environmental Engineering

ABSTRACT

It is well recognized that groundwater-surface water interactions influence the quantity and quality of various hydrogeological systems (rivers, lakes, streams). Groundwater-stream systems are an important investigative area for understanding fate and transport of nutrients and chemicals within the stream. While traditional methodologies are established to provide measurement and mapping of the spatial distribution of groundwater-stream interactions and exchange fluxes across a streambed, many can be invasive, labour intensive and suffer from low sampling density. The complexity in such systems is due largely to the heterogeneous nature both spatially and temporally. Given the strong control by streambed lithology on groundwater-surface water interactions, an improved measure of the spatial and temporal variations is desired. Geophysical techniques of DC-IP are an intriguing option as they can provide rapid, non-invasive and continuous information about the subsurface. The overall thesis objective was to evaluate the potential of 3D DC-IP for characterizing the structural heterogeneities within a streambed to inform assessment of groundwater-stream water interactions.

High-resolution 3D DC-IP surveys were conducted in a 50 m long headwater stream reach located in Kintore, Ontario. The resulting 3D distributions of resistivity and chargeability highlighted the heterogeneous nature of the streambed. Traditional characterization techniques were employed to evaluate the performance of DC-IP for mapping streambed composition and its associated influence on groundwater-stream exchanges. Strong concordance between DC-IP imaging and all the other traditional methods were determined, providing increased confidence in the ability of DC-IP to provide a valuable, non-invasive site tool to improve characterization of streambed heterogeneity and interpretation of groundwater-stream exchange patterns.

Keywords

DC resistivity, induced polarization, streambed heterogeneity, streambed characterization, groundwater-surface water interactions, groundwater-surface water exchange fluxes

SUMMARY FOR LAY AUDIENCE

Groundwater and surface water interact nearly everywhere on earth. These interactions take place in rivers, lakes, streams and more. It is understood that through these interactions the quality and quantity could be affected in either water body. Groundwater-stream systems are of particular interest to understand how nutrients and contaminants may transport across streambeds. Investigations of groundwater and stream water systems have been long established and traditional techniques are used to determine the interactions involved. However, many of these traditional techniques have various limitations, such as: being labour intensive, destructive and invasive to the stream or subsurface and do not provide characterization throughout an entire investigative site. The difficulty with understanding groundwater-stream water systems is that the conditions affecting the interactions change with regards to space and time. The specific changes in the sediments of a streambed or aquifer are thought to heavily affect the interactions and exchanges between groundwater and stream water. Therefore, an improved way of measuring these changes in space and time are desired. This was achieved using geophysical techniques, which use electrical current to produce an image of the subsurface. This can be done to better seen inside/beneath a streambed, similar to an x-ray, but of the ground.

This study used geophysical techniques to create 3D images of the subsurface of a stream located in Kintore, Ontario. These images were used to help understand the interactions involved in the groundwater-stream water system.

CO-AUTHORSHIP STATEMENT

This thesis is written in accordance with the guidelines and regulations for an Integrated Article format stipulated by the School of Graduate and Postgraduate Studies at the University of Western Ontario. The candidate is responsible for the collection and analysis of field data, as well as writing the drafts of all chapters of this thesis. Dr. Christopher Power and Dr. Clare Robinson provided the initial motivation for this research, assisted with fieldwork, provided suggestions for data analysis, and provided revisions for improvement of the thesis. The co-authorship breakdown of Chapter 3 is as follows:

Authors: Kyle Robinson, Christopher Power, Clare Robinson

Contributions:

Kyle Robinson conducted collection and analysis of field data, model computations, interpretation of the results, and was the lead author for writing the chapter.

Christopher Power supervised field data collection, analysis, provided insight and interpretation of results, and reviewed the draft of chapter.

Clare Robinson supervised field data collection, analysis, provided insight and interpretation of results, and reviewed the draft of chapter.

Jim Roy provided input on field site selection, field methods and assisted in analysis and interpretation of results.

Uwe Schneidewind assisted with initial field set up of traditional groundwater-surface water exchange methodologies and conducting data analysis.

DEDICATION

This thesis is dedicated to my family. Thank you for everything.

ACKNOWLEDGMENTS

I would like to express my sincere gratitude to my supervisors Dr. Chris Power and Dr. Clare Robinson, for your advice, encouragement, and support over the last two years. I truly appreciated your continued support, influence and mentorship, especially throughout these unprecedented times. I am incredibly grateful to have been able to call you both my supervisors.

I would like to extend a thank you to Dr. Jason Gerhard and to all of the RESTORE research group for the friendships, inspiration and continued encouragement that so noticeably extends to everyone who becomes involved with the group. It was truly an honour to work with each and every member. The support displayed throughout the group, especially during these unprecedented times, is second to none and never goes unnoticed.

Thank you to NSERC, who provided financial aid through the Strategic Project Grant (STPG 506523), which made this project possible.

I would like to express my gratitude to Jim Roy, Uwe Schneidewind, Meghan Vissers, Shuyang Wang, Ethan Kamps and Angelos Almpanis for their specific assistance in conducting all the field work needed to complete this project.

Thank you to my close friends for their continued understanding, support and motivation.

Finally, I would like to thank my family for their unconditional love and support. Thank you for instilling strong values within our family, allowing for me to continue to grow as a person.

TABLE OF CONTENTS

LIST OF TABLES

LIST OF FIGURES

LIST OF APPENDICIES

1 INTRODUCTION

1.1 RESEARCH BACKGROUND

Groundwater and stream water can interact across a variety of scales, ranging from heterogeneities within centimeters to meters, to entire catchments. Characterization of subsurface geology of varying scale sizes is important as properties such as the hydraulic conductivity, porosity, permeability, and the hydraulic gradients within a porous medium are used in quantifying groundwater-stream water (GW-SW) exchange fluxes (Khan & Khan, 2019; Sophocleous, 2002; Woessner, 2000).

At the stream reach scale, sediment compositions are highly spatially heterogeneous, and these heterogeneities can influence the water chemistry and ecological conditions within the streambed and the stream itself. Physical properties of streambed sediments, such as sediment surface area, grain size distribution and cation exchange capacity, can control the fate of chemicals discharging, or cycling, across streambeds. This is due to their influence on the residence time of chemical constituents, nutrients, preferential pathways, and the geochemical conditions along discharge or hyporheic flow paths (Conant et al., 2004; Irvine et al., 2020; Wang et al., 2021).

At the local scale, the connectivity between the groundwater and stream water, and therefore the quantity and direction of the fluxes, is dependent on: (i) head difference of the water table and stream surface levels, and (ii) hydraulic properties of the connected aquifer system, including any geological material separating the aquifer from the stream, and its ability to transmit water to or from the stream (Reid et al., 2009; Schmidt et al., 2006). While attempting to understand and quantify GW-SW interactions, there is much more uncertainty involved, which ultimately arises from the inherent spatial and temporal heterogeneity of physical and reactive properties present in sediments throughout the subsurface, and at the GW-SW interface.

Spatial variabilities can exist on a scale of centimeters to meters, adding to the complexity of properly characterizing and evaluating a system. Large-scale investigations may not include the detailed features that exist at a localized scale, while local investigations could omit information on larger ‘outside’ properties that influence GW-SW exchanges. Exchanges between groundwater and stream water can vary temporally over time scales of hours, days, or months. Seasonal basis,

or extreme weather events, can also cause a reverse in flow direction. This adds to the complexity and challenge of accurately characterizing water and chemical fluxes across streambeds (Cremeans et al., 2020; González-Pinzón et al., 2015).

Common approaches used to characterize spatial heterogeneity within streambeds still rely on the extraction and analysis of soil corings, which can provide information on lithology and hydraulic properties such as porosity and intrinsic permeability (Dara et al., 2019). However, these techniques are invasive, labor intensive and require sometimes excessive assumptions between the sparsely distributed sampling locations. Approaches used to examine GW-SW exchanges typically include seepage meters, hydraulic gradient measurements, and thermal profiling, but again they suffer from low sampling density. Alternative approaches such as stream discharge and tracer techniques can provide greater spatial coverage, they are limited by low resolution and often miss the true heterogeneities that represent flow anomalies, such as low and high mobility zones (Kurylyk et al., 2019; Rosenberry, 2008).

Geophysical techniques can provide rapid, cost-effective and continuous information and are transforming our ability to image the composition of the subsurface and monitor dynamic processes occurring within it (e.g., McLachlan et al., 2017; Binley et al., 2005). DC resistivity and induced polarization (IP) are now the most widely used geophysical techniques, with significant advancements in the past decade leading to their increased popularity for hydrogeological and geoenvironmental investigations (Binley et al., 2015). DC and IP measure the subsurface distribution of electrical resistivity and chargeability, respectively, which can then be used to infer hydrogeological features and processes of interest (Nyquist et al., 2009).

DC and IP exhibit strong promise for improving characterization of streambed lithology and heterogeneity, which can then be used to improve understanding on water and chemical fluxes across streambed (McLachlan et al., 2017). DC resistivity can be used to identify streambed variations influenced by pore-water and grain conductivity, while IP complements DC resistivity by discriminating between clayey and non-clayey soils. Currently, the application of DC-IP for streambed characterization has been limited. Standalone DC resistivity has been applied to map streambed lithology but has been limited to two-dimensional (2D) surveys that are unable to accurately capture the 3D complexity within streambeds that typically exhibit significant

variability in the longitudinal and transverse directions (e.g., Earon et al., 2020). While time-domain IP has not been employed for streambed characterization, frequency-domain IP was recently employed by Wang et al. (2021) to characterize physical properties of streambed sediments such as surface area; however, the dataset was limited to raw 1D measurements.

DC and IP should be combined (referred to as DC-IP) and performed in 3D is to adequately capture the high complexity and heterogeneity of streambeds. In addition to mapping lithology, it is highly beneficial to assess the relationship between lithology and GW-SW exchange patterns. This can further reinforce the value of DC-IP for mapping streambeds as it can not only be used to directly infer lithology, but also provide indirect information on GW-SW exchange.

The objective of this thesis was to evaluate the potential of 3D DC-IP for improving the characterization of streambed composition, which can then indirectly improve the understanding of GW-SW exchanges. A multi-disciplinary investigation of a stream reach in Kintore, Ontario, was performed, with numerous approaches being applied alongside DC-IP, including soil corings, hydraulic gradient measurements, thermal mapping and GW-SW flux measurements. This allowed a comprehensive investigation of the streambed, while also assessing the performance of DC-IP relative to traditional approaches.

1.2 RESEARCH OBJECTIVES

The overall goal of this thesis is to evaluate the potential of 3D DC-IP for complete characterization of streambed structural heterogeneities at a localized scale, and how this technique can be integrated with traditional hydrogeological approaches to improve the understanding of GW-SW interactions at complex field sites. As part of this goal, the following sub-objectives were addressed:

1) Conduct DC-IP surveys at a stream reach site in Kintore, Ontario, with high-resolution 3D surveys being performed within the stream and in the adjacent riparian zone.

2) Conduct traditional hydrogeological approaches, such as hydraulic gradient mapping, temperature difference mapping, sediment corings and temperature flux monitoring, to characterize the streambed and assess GW-SW exchanges

3) Assess the connection between objectives 1 and 2, to both validate the performance of DC-IP and assess whether this integrated approach can enhance the understanding of GW-SW exchanges in a complex environment

1.3 THESIS OUTLINE

This thesis is written in an "Integrated Article" format. A brief description of the subsequent chapters presented are as follows:

- Chapter 2: summarizes the scientific literature relevant to GW-SW interactions on a variety of scales and the importance of understanding these processes. Traditional hydrogeological techniques used to quantify the GW-SW exchanges and geophysical methodologies used to characterize geologic variations that affect such exchanges are discussed.

- Chapter 3: details how various methodologies were used at the field site in Kintore, Ontario, to evaluate the performance of high-resolution DC-IP imaging to improve characterization of a stream reach and understanding of GW-SW exchanges.

- Chapter 4: summarizes the findings of this research and suggests recommendations for future work.

- Appendices: provides supplemental information for the work presented in Chapter 3. This information includes summaries and results from conducted field, laboratory and analytical methods that could not be included in their entirety within Chapter 3.

1.4 REFERENCES

Binley, A., & Kemna, A. (2005). *Hydrogeophysics* (Y. Rubin & S. S. Hubbard (eds.); Vol. 50, Issue October 2016). Springer Netherlands. https://doi.org/10.1007/1-4020-3102-5

Binley, A., Hubbard, S. S., & Huisman, J. a. (2015). The emergence of hydrogeophysics for improved understanding of subsurface processes over multiple scales. *Water Resources Research*, 1–30. https://doi.org/10.1002/2015WR017016.Received

Bigalke, J., & Junge, A. (1999). Using evidence of non-linear induced polarization for detecting extended ore mineralizations. *Geophysical Journal International*, *137*(2), 516–520. https://doi.org/10.1046/j.1365-246X.1999.00805.x

Binley, A., Hubbard, S. S., & Huisman, J. a. (2015). The emergence of hydrogeophysics for improved understanding of subsurface processes over multiple scales. *Water Resources Research*, 1–30. https://doi.org/10.1002/2015WR017016.Received

Binley, A., & Kemna, A. (2005). *Hydrogeophysics* (Y. Rubin & S. S. Hubbard (eds.); Vol. 50, Issue October 2016). Springer Netherlands. https://doi.org/10.1007/1-4020-3102-5

Brunke, M., & Gonser, T. (1997). The ecological significance of exchange processes between rivers and groundwater. *Freshwater Biology*, *37*(1), 1–33. https://doi.org/10.1046/j.1365-2427.1997.00143.x

Campbell, D. L., Fitterman, D. V., Hein, A. S., & Jones, D. P. (1998). Spectral Induced Polarization Studies of Mine Dumps Near Silverton, Colorado. *Symposium on the Application of Geophysics to Engineering and Environmental Problems 1998*, *6*(1), 761–769. https://doi.org/10.4133/1.2922567

Carrière, S. D., Chalikakis, K., Sénéchal, G., Danquigny, C., & Emblanch, C. (2013). Combining Electrical Resistivity Tomography and Ground Penetrating Radar to study geological structuring of karst Unsaturated Zone. *Journal of Applied Geophysics*, *94*, 31–41. https://doi.org/10.1016/j.jappgeo.2013.03.014

Chambers, J. E., Kuras, O., Meldrum, P. I., Ogilvy, R. D., & Hollands, J. (2006). Electrical

resistivity tomography applied to geologic, hydrogeologic, and engineering investigations at a former waste-disposal site. *Geophysics*, *71*(6). https://doi.org/10.1190/1.2360184

Conant, B., Cherry, J. A., & Gillham, R. W. (2004). A PCE groundwater plume discharging to a river: Influence of the streambed and near-river zone on contaminant distributions. *Journal of Contaminant Hydrology*, *73*(1–4), 249–279. https://doi.org/10.1016/j.jconhyd.2004.04.001

Conant, B., Robinson, C. E., Hinton, M. J., & Russell, H. A. J. (2019). A framework for conceptualizing groundwater-surface water interactions and identifying potential impacts on water quality, water quantity, and ecosystems. *Journal of Hydrology*, *574*(March), 609–627. https://doi.org/10.1016/j.jhydrol.2019.04.050

Coscia, I., Greenhalgh, S. A., Linde, N., Doetsch, J., Marescot, L., GuNther, T., Vogt, T., & Green, A. G. (2011). 3D crosshole ERT for aquifer characterization and monitoring of infiltrating river water. *Geophysics, 76*(2). https://doi.org/10.1190/1.3553003

Cremeans, M. M., Devlin, J. F., Osorno, T. C., McKnight, U. S., & Bjerg, P. L. (2020). A Comparison of Tools and Methods for Estimating Groundwater-Surface Water Exchange. *Groundwater Monitoring and Remediation*, *40*(1), 24–34. https://doi.org/10.1111/gwmr.12362

Crook, N., Binley, A., Knight, R., Robinson, D. A., Zarnetske, J., & Haggerty, R. (2008). Electrical resistivity imaging of the architecture of substream sediments. *Water Resources Research*, *46*(4), 1–11. https://doi.org/10.1029/2008WR006968

Dahl, M., Nilsson, B., Langhoff, J. H., & Refsgaard, J. C. (2007). Review of classification systems and new multi-scale typology of groundwater-surface water interaction. *Journal of Hydrology*, *344*(1–2), 1–16. https://doi.org/10.1016/j.jhydrol.2007.06.027

Dara, R., Kettridge, N., Rivett, M. O., Krause, S., & Gomez-Ortiz, D. (2019). Identification of floodplain and riverbed sediment heterogeneity in a meandering UK lowland stream by ground penetrating radar. *Journal of Applied Geophysics*, *171*, 103863. https://doi.org/10.1016/j.jappgeo.2019.103863

Fleckenstein, J. H., Krause, S., Hannah, D. M., & Boano, F. (2010). Groundwater-surface water interactions: New methods and models to improve understanding of processes and dynamics. *Advances in Water Resources*, *33*(11), 1291–1295. https://doi.org/10.1016/j.advwatres.2010.09.011

Friedel, S., Thielen, A., & Springman, S. M. (2006). Investigation of a slope endangered by rainfall-induced landslides using 3D resistivity tomography and geotechnical testing. *Journal of Applied Geophysics*, *60*(2), 100–114. https://doi.org/10.1016/j.jappgeo.2006.01.001

Gaffney, C. (2008). Detecting trends in the prediction of the buried past: A review of geophysical techniques in archaeology. *Archaeometry*, *50*(2), 313–336. https://doi.org/10.1111/j.1475-4754.2008.00388.x

Gazoty, A., Fiandaca, G., Pedersen, J., Auken, E., & Christiansen, A. V. (2012). Mapping of landfills using time-domain spectral induced polarization data: The Eskelund case study. *Near Surface Geophysics*, *10*(6), 575–586. https://doi.org/10.3997/1873-0604.2012046

González-Pinzón, R., Ward, A. S., Hatch, C. E., Wlostowski, A. N., Singha, K., Gooseff, M. N., Haggerty, R., Harvey, J. W., Cirpka, O. A., & Brock, J. T. (2015). A field comparison of multiple techniques to quantify groundwater-surface-water interactions. *Freshwater Science*, *34*(1), 139–160. https://doi.org/10.1086/679738

Hamilton, P. (2005). Groundwater and surface water: A single resource. *Water Environment and Technology*, *17*(5), 37–41.

Hannah, D. M., Malcolm, I. A., & Bradley, C. (2009). Seasonal hyporheic temperature dynamics over riffle bedforms. *Hydrological Processes*, *23*(15), 2178–2194. https://doi.org/10.1002/hyp.7256

Hemeda, S. (2013). Electrical Resistance Tomography (ERT) Subsurface Imaging for Non-destructive Testing and Survey in Historical Buildings Preservation. *Australian Journal of Basic and Applied Sciences*, *June*, 344–357.

Irvine, D. J., Kurylyk, B. L., & Briggs, M. A. (2020). Quantitative guidance for efficient vertical

flow measurements at the sediment–water interface using temperature–depth profiles. *Hydrological Processes*, *34*(3), 649–661. https://doi.org/10.1002/hyp.13614

Kalbus, E., Reinstorf, F., & Schirmer, M. (2006). Measuring methods for groundwater – surface water interactions: a review. *Hydrology and Earth System Sciences*, *10*(6), 873–887. https://doi.org/10.5194/hess-10-873-2006

Khan, H. H., & Khan, A. (2019). Groundwater and surface water interaction. In *GIS and Geostatistical Techniques for Groundwater Science* (Issue 2000). Elsevier Inc. https://doi.org/10.1016/B978-0-12-815413-7.00014-6

Kiberu, J. (2002). Induced polarization and Resistivity measurements on a suite of near surface soil samples and their empirical relationship to selected measured engineering parameters. *Interntional Institute for Geo-Information Science and Earth Observation Enschede, The Netherlands*, 119.

Krause, S., Hannah, D. M., Fleckenstein, J. H., Heppell, C. M., Kaeser, D., Pickup, R., Pinay, G., Robertson, A. L., & Wood, P. J. (2011). Inter-disciplinary perspectives on processes in the hyporheic zone. *Ecohydrology*, *4*(4), 481–499. https://doi.org/10.1002/eco.176

Krause, Stefan, Lewandowski, J., Grimm, N. B., Hannah, D. M., Pinay, G., McDonald, K., Martí, E., Argerich, A., Pfister, L., Klaus, J., Battin, T., Larned, S. T., Schelker, J., Fleckenstein, J., Schmidt, C., Rivett, M. O., Watts, G., Sabater, F., Sorolla, A., & Turk, V. (2017). Ecohydrological interfaces as hot spots of ecosystem processes. *Water Resources Research*, *53*(8), 6359–6376. https://doi.org/10.1002/2016WR019516

Kurylyk, B. L., Irvine, D. J., & Bense, V. F. (2019). Theory, tools, and multidisciplinary applications for tracing groundwater fluxes from temperature profiles. *Wiley Interdisciplinary Reviews: Water*, *6*(1), e1329. https://doi.org/10.1002/wat2.1329

Kurylyk, B. L., Irvine, D. J., Carey, S. K., Briggs, M. A., Werkema, D. D., & Bonham, M. (2017). Heat as a groundwater tracer in shallow and deep heterogeneous media: Analytical solution, spreadsheet tool, and field applications. *Hydrological Processes*, *31*(14), 2648–2661. https://doi.org/10.1002/hyp.11216

Li, Y., & Oldenburg, D. W. (2000). 3-D inversion of induced polarization data. *Geophysics*, *65*(6), 1931–1945. https://doi.org/10.1190/1.1444877

Loke M. H. (2015). 2-D and 3-D Electrical Imaging Surveys. *Tutorial*, *May*, 51–52.

McLachlan, P. J., Chambers, J. E., Uhlemann, S. S., & Binley, A. (2017). Geophysical characterisation of the groundwater–surface water interface. *Advances in Water Resources*, *109*(August), 302–319. https://doi.org/10.1016/j.advwatres.2017.09.016

Naudet, V., Revil, A., Rizzo, E., Bottero, J. Y., & Bégassat, P. (2004). Groundwater redox conditions and conductivity in a contaminant plume from geoelectrical investigations. *Hydrology and Earth System Sciences*, *8*(1), 8–22. https://doi.org/10.5194/hess-8-8-2004

Nyquist, J. E., Heaney, M. J., & Toran, L. (2009). *Characterizing lakebed seepage and geologic heterogeneity using resistivity imaging and temperature measurements*. 487–498.

Poole, G. C., O'Daniel, S. J., Jones, K. L., Woessner, W. W., Bernhardt, E. S., Helton, A. M., Stanford, J. A., Boer, B. R., & Beechie, T. J. (2008). Hydrologic spiralling: the role of multiple interactive flow paths in stream ecosystems. *River Research and Applications*, *24*(7), 1018–1031. https://doi.org/10.1002/rra.1099

Power, C., Tsourlos, P., Ramasamy, M., Nivorlis, A., & Mkandawire, M. (2018). Combined DC resistivity and induced polarization (DC-IP) for mapping the internal composition of a mine waste rock pile in Nova Scotia, Canada. *Journal of Applied Geophysics*, *150*, 40–51. https://doi.org/10.1016/j.jappgeo.2018.01.009

Reid, M., Cheng, X., Banks, E. W., Jankowski, J., Jolly, I., Kumar, P. B., Lovell, D., Mitchell, M., Mudd, G., Richardson, S., Silburn, M., & Werner, A. D. (2009). Catalogue of conceptual models for groundwater–stream interaction in eastern Australia. In *eWater Cooperative Research Centre Technical Report* (Issue May 2014).

Renard, P., & Allard, D. (2013). Connectivity metrics for subsurface flow and transport. *Advances in Water Resources*, *51*, 168–196. https://doi.org/10.1016/j.advwatres.2011.12.001

Robert, T., Caterina, D., Deceuster, J., Kaufmann, O., & Nguyen, F. (2012). A salt tracer test monitored with surface ERT to detect preferential flow and transport paths in fractured/karstified limestones. *Geophysics*, *77*(2). https://doi.org/10.1190/geo2011-0313.1

Schmidt, C., Bayer-Raich, M., & Schirmer, M. (2006). Characterization of spatial heterogeneity of groundwater-stream water interactions using multiple depth streambed temperature measurements at the reach scale. *Hydrology and Earth System Sciences*, *10*(6), 849–859. https://doi.org/10.5194/hess-10-849-2006

Seigel, H. O. (1959). MATHEMATICAL FORMULATION AND TYPE CURVES FOR INDUCED POLARIZATION. *GEOPHYSICS*, *24*(3), 547–565. https://doi.org/10.1190/1.1438625

Slater, L. D., & Lesmes, D. (2002). IP interpretation in environmental investigations. *Geophysics*, *67*(1), 77–88. https://doi.org/10.1190/1.1451353

Smith, J. W. N. (2005). Groundwater – surface water interactions in the hyporheic zone. In *Environment Agency Science report SC030155/SR1, Environment Agency: Bristol, UK*. www.environment-agency.gov.uk

Sogade, J. A., Scira-Scappuzzo, F., Vichabian, Y., Shi, W., Rodi, W., Lesmes, D. P., & Morgan, F. D. (2006). Induced-polarization detection and mapping of contaminant plumes. *Geophysics*, *71*(3). https://doi.org/10.1190/1.2196873

Sophocleous, M. (2002). Interactions between groundwater and surface water: The state of the science. *Hydrogeology Journal*, *10*(1), 52–67. https://doi.org/10.1007/s10040-001-0170-8

Stonestrom, D., & Constantz, J. (2003). Heat as a tracer to determine streambed water exchanges. *Water Resources Research*, *44*(4). https://doi.org/10.1029/2008WR006996

Storz, H., Storz, W., & Jacobs, F. (2000). Electrical resistivity tomography to investigate geological structures of the earth's upper crust. *Geophysical Prospecting*, *48*(3), 455–471. https://doi.org/10.1046/j.1365-2478.2000.00196.x

Tonina, D., & Buffington, J. M. (2007). Hyporheic exchange in gravel bed rivers with pool-riffle

morphology: Laboratory experiments and three-dimensional modeling. *Water Resources Research*, *43*(1), 1–16. https://doi.org/10.1029/2005WR004328

Tsokas, G. N., Tsourlos, P. I., Vargemezis, G., & Novack, M. (2008). Non-destructive electrical resistivity tomography for indoor investigation: The case of Kapnikarea Church in Athens. *Archaeological Prospection*, *15*(1), 47–61. https://doi.org/10.1002/arp.321

Tsourlos, P. (1995). Modelling, Interpretation and Inversion of Multielectrode Resistivity Survey Data. *University of York, November*, 294.

Vaudelet, P., Schmutz, M., Pessel, M., Franceschi, M., Guérin, R., Atteia, O., Blondel, A., Ngomseu, C., Galaup, S., Rejiba, F., & Bégassat, P. (2011). Mapping of contaminant plumes with geoelectrical methods. A case study in urban context. *Journal of Applied Geophysics*, *75*(4), 738–751. https://doi.org/10.1016/j.jappgeo.2011.09.023

Wang, C., Briggs, M. A., Day-Lewis, F. D., & Slater, L. D. (2021). Characterizing Physical Properties of Streambed Interface Sediments Using In Situ Complex Electrical Conductivity Measurements. *Water Resources Research*, *57*(2), 1–19. https://doi.org/10.1029/2020WR027995

Winter, T. C. (1999). Relation of streams, lakes, and wetlands to groundwater flow systems. *Hydrogeology Journal*, *7*, 28–45.

Winter, T. C., Harvey, J. W., & Alley, W. M. (1998). *Ground water and surface water a single resource: U* (Issue May). https://doi.org/10.3133/cir1139

Woessner, W. W. (2000). Stream and Fluvial Plain Ground Water Interactions: Rescaling Hydrogeologic Thought. *Ground Water*, *38*(3), 423–429. https://doi.org/10.1111/j.1745-6584.2000.tb00228.x

Wondzell, S. M., Herzog, S. P., Gooseff, M. N., Ward, A. S., & Schmadel, N. M. (2019). Geomorphic Controls on Hyporheic Exchange Across Scales—Watersheds to Particles. In *Reference Module in Earth Systems and Environmental Sciences*. Elsevier. https://doi.org/10.1016/B978-0-12-409548-9.12135-9

2 LITERATURE REVIEW

This chapter summarizes the scientific literature relevant to the characterization of groundwater-surface water interactions with specific focus in headwater streams. Many stream system characterization methodologies exist and are well established in hydrogeology, but the scale of groundwater-surface interactions is largely varied, resulting in methodologies that are site specific. The importance of accurate characterization of groundwater-stream water (GW-SW) is discussed and the linkages that exist to solute transport, such as phosphorus (P). The use of geophysical techniques such as DC resistivity (DC) and induced polarization (IP) have been increasing in popularity in hydrogeological studies and have been described to provide background information for this thesis. This review will examine the current state of knowledge with respect to hydrogeological techniques in GW-SW characterization, the applicability and use of geophysical methodologies in hydrogeological studies and the combination of techniques used in headwater systems. A summary is presented which identifies research gaps and opportunities.

2.1 GROUNDWATER-SURFACE WATER INTERACTIONS

2.1.1 INTRODUCTION

Groundwater and surface water are complex interconnected components of hydrologic systems. Interactions between surface waters (streams, rivers, lakes, etc.) and groundwater occur nearly everywhere on earth, in a variety of hydrological, geochemical, or biological settings. (Khan & Khan, 2019; Sophocleous, 2002; Winter et al., 1998). The connection between groundwater-surface water is understood to impact the quantity and quality in both entities and emphasizes the need for an understanding of interactions in a range of settings (Conant et al., 2019).

2.1.2 GROUNDWATER-STREAM

Ground water and streams interact in a variety of landscapes. These interactions occur in three situations: (i) loss of surface water to groundwater, (ii) seepage of groundwater to the surface water body, and (iii) combination of both. Therefore, groundwater-stream systems can be defined as ‘gaining’, ‘losing’, or both (Winter et al., 1998). According to Woessner (2000), the interactions between groundwater and streams is controlled by: (i) the distribution of hydraulic conductivity in

channel sediments, (ii) the position of the stream stage with respect to the adjacent groundwater, and (iii) the position and geometry of the stream channel within the fluvial plain.

Groundwater upwelling to a stream (i.e., gaining stream) occurs when the hydraulic head of the groundwater is higher than the stream water, whereas downwelling (i.e., losing stream) occurs when hydraulic head of the stream is higher relative to the adjacent groundwater. This is shown in Figure 2-1. Other classifications may be given to a stream reach, such as a flow through reach, parallel flow reach or a disconnected losing reach (Khan & Khan, 2019). Flow through reaches occur when the hydraulic gradient between groundwater levels vary from opposite banks. This condition is more common when a stream is perpendicular to regional groundwater flow (Woessner, 2000). A parallel flow reach exits when the groundwater and adjacent stream water have nearly equivalent hydraulic head levels, resulting in little to no exchange. A disconnected losing reach is a special case, where the stream is higher than the groundwater and is separated by an unsaturated sediment zone (Kalbus et al., 2006). Seasonal variability in precipitation and severe storm events can cause changes to the hydraulic heads and reverse exchange flow directions within a GW-SW system (Hamilton, 2005). Within a GW-SW system, the exchanges are typically categorized as regional, local (hyporheic), or both, which is discussed further in section 2.1.4.

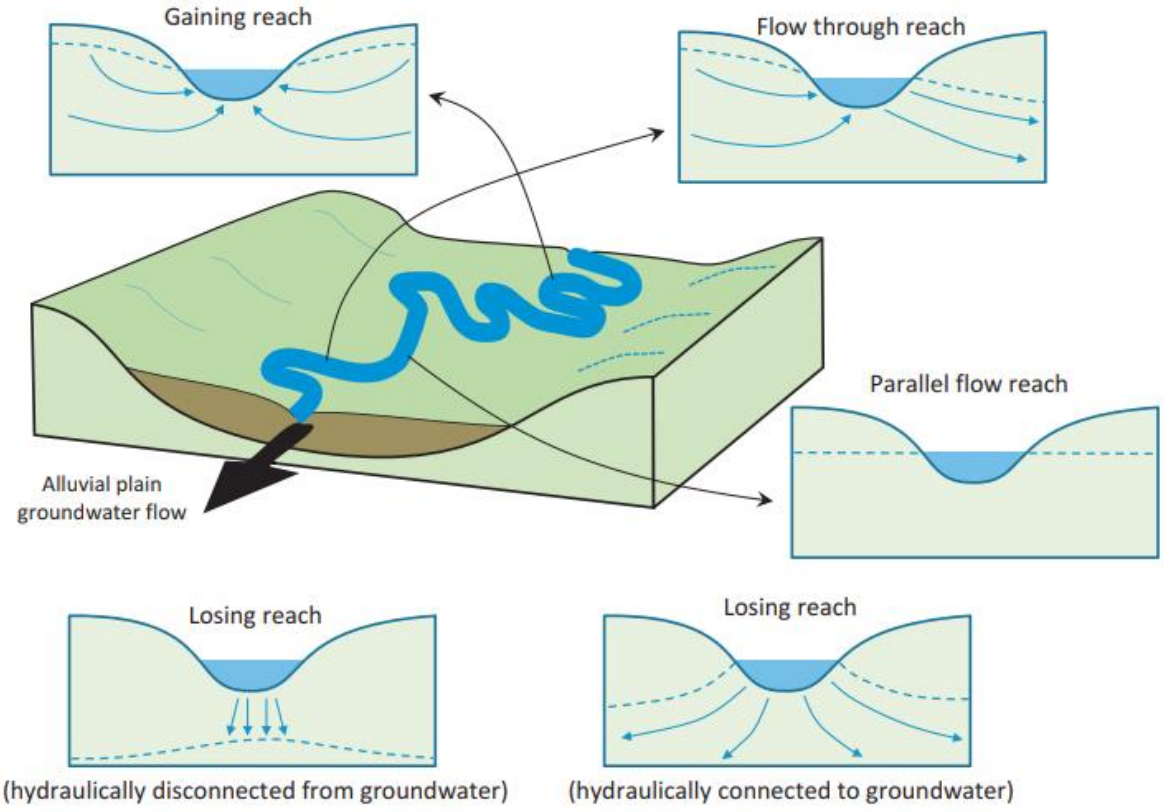

Figure 2-1: Various characterizations of groundwater-stream water interactions (source: Khan & Khan, 2019)

2.1.3 HYPORHEIC ZONE

The interface between groundwater and surface water is characterized as the physical boundary between the two water bodies, i.e., the top of subsurface materials where SW is in contact. The area within the underlying sediments comprised of mixing between subsurface water and surface water is defined as the hyporheic zone (Sophocleous, 2002). The interactions in the hyporheic zone are typically independent of larger scale reactions, and therefore areas of a reach or catchment that are considered 'gaining' or 'losing' may still have areas of upwelling or downwelling, due to hyporheic exchanges. Interactions are mainly controlled by the localized topography of the stream bed and the hydraulic conductivity distribution of the underlying sediments (Woessner, 2000). The hyporheic zone is significant with respect to the surface and groundwater quality, and stream ecological functions. The interaction of water with minerals and organic bio-films is enhanced as the passage of stream water into underlying sediments increases the residence time of water within

the ground, leading to modifications in water quality and potential attenuation of pollutants. The downwelling and upwelling of stream water also dictates the faunal composition, distribution, and abundance within the hyporheic zone as well as surface-water body (Brunke and Gonser, 1997).

There has been deliberation with regards to characterization of the hyporheic zone, as it can be viewed from a hydrological, ecological or hydrogeological perspective (Smith, 2005). Hydrological studies are concerned with the exchange fluxes that occur within the hyporheic zone. Ecological studies have focused on the function of the hyporheic zone as a site development for benthic microorganisms. Hydrogeological studies are concerned with the hyporheic zone as a part of the groundwater system and also takes into the account the high presence of organic materials and microbial communities.

It is important to appreciate the variety of processes involved in the hyporheic zone, their driving factors and the interconnectivity of studies when determining the impacts of exchanges over time and space.

2.1.4 EXCHANGE FLUX

An essential parameter used when describing GW-SW interactions is the Darcy flux (specific discharge). Interactions between groundwater and surface water can vary in space and time and across a wide range of physical scales and accurately quantifying spatial and temporal flux variations can assist in various water management practices (quantity and quality). Fluxes between groundwater and streams are referred to as exchange fluxes. The exchange fluxes in a GW-SW system contain two components: groundwater-surface water exchange flux and hyporheic exchange flux (Hannah et al., 2009). As described in section 2.1.2, GW-SW exchange flux typically describes a gain or loss to the stream reach from water entering or leaving the stream, whereas hyporheic exchange flux occurs when stream water enter the HZ at an upstream point, and then exiting back to the stream at a downstream point. Differentiating between the exchange fluxes can be difficult and for the purpose of this study, they are lumped together.

Three arbitrary sized scales are often considered as boundaries for studies of GW-SW interactions: catchment (>1000 m), reach (1-1000 m), and sediment (<1 m), (Dahl et al., 2007). The

interconnected flow paths between GW-SW can vary in length from centimeters to more than a kilometer (Poole et al., 2008).

At the catchment scale, groundwater and surface water patterns are controlled predominately by topographic and geologic attributes, while recharge distribution and overland flow is attributed to the climatic region. Therefore, downwelling conditions are often found in the upper stream reach, as topography causes unsaturated conditions. Conversely, middle reach groundwater often have higher contribution to stream flow increases and are considered gaining reaches. In low reaches, groundwater and surface water hydraulic gradients are often small and therefore result in parallel flows. These tendencies can vary due to local geography.

At the reach scale flow conditions will depend on several factors including the geometrical properties of the stream (width, depth, wetted perimeter, etc.), streambed sediment heterogeneity, streambed morphology and local characteristics of connected aquifers (Buss et al., 2009). Flow conditions are more effluent when streams have a large meandering path or when the stream width to depth ratio is small. Variations in streambed heterogeneity define the hydraulic conductivity distribution and the behaviour of local flow paths. Streambed morphology influences exchange flows and discharge patterns depending on the pool-riffle-run sequences present. Local climatic and land use conditions influence discharge and recharge patterns.

At the sediment scale flow patterns are predominately defined by sediment physical properties. Grain size, shape, distribution and compaction directly influence the permeability, porosity and hydraulic conductivity throughout a stream, causing the formation of preferential pathways. Flow patterns at sediment and reach scale are also influence by local features such as pool-riffle-runs, or due to obstructing obstacles such as wood, rocks, etc.

2.1.5 MAPPING AND MONITORING GROUNDWATER-STREAM WATER PROPERTIES

Various techniques exist to aide in characterizing GW-SW interactions and understanding the hydrological, biological and/or ecological characteristics at various spatial and temporal scales. This is challenging as GW-SW systems are dynamic in time and space and measurements and certain scales may not be representative across the system. Accurate determination of parameters such as hydraulic gradients, hydraulic conductivity, porosity or grain size distribution is needed.

Additionally, exchange fluxes can be assessed using both direct and indirect measurements. These techniques are listed in Table 2-1, including their desired parameter measurement, the spatial scale of application and additional resources. It is noted that a number of assessment methods measurements are collected on the sediment scale, indicating that these traditional techniques are susceptible to limited sampling density.

Table 2-1: Commonly mapped GW-SW parameters, their respective assessment method, the typical associated scale and relevant literature.

Classification Area	Property	Assessment Method	Scale	Reference
Determining GW-SW Exchange	Darcy Flux	Seepage meter measurements	Sediment	Rosenberry and LaBaugh (2008)
		Tests with environmental traces	Reach	Berryman (2005)
		Incremental streamflow	Reach to catchment	Harvey and Wagner (2000)
		Hydrograph separation	Reach to catchment	Hornberger et al. (1998)
	Hydraulic gradient	Water level measurements in piezometers	Sediment	Rosenberry and LaBaugh (2008)
		Potenio-manometer boards	Sediment	Winter et al. (1988)
Determining Reach Property	Hydraulic conductivity	Grain size analysis	Sediment	Vienken and Dietrich (2011)
		Pumping tests	Sediment to reach	Fetter (2001)
		Permeameter tests	Sediment	Freeze and Cherry (1979)
	Porosity	Laboratory tests on sediment samples	Sediment	Fetter (2001)
	Flow Velocity	In-situ tracer tests	Reach	Berryman (2005)

2.1.5.1 HEAT AS A TRACER

The quantification of exchange fluxes has become an integral part in many investigations as magnitudes of exchanges and how they vary spatially and temporally can indicate connectivity between GW-SW systems. Heat can be used as a tracer to indirectly quantify exchange fluxes. With this method, temperature as a measure of heat is used in combined water flow and heat transport models to deduce the flow of water from a measured temperature distribution in the streambed. Main advantages of this method are that temperature is an easy, inexpensive and accurate property to measure, and that the thermal parameters needed for the coupled model have a very limited range.

Temperature-based analytical solutions are commonly used in various models, to infer the direction and estimate the magnitude of groundwater-surface water exchange fluxes (Irvine et al., 2020; Stonestrom & Constantz, 2003). For the purpose of this study, Flux in Layered Media (Flux-LM) automated spreadsheet tool was used (Kurylyk et al., 2017). The Flux-LM tool uses temperature depth (TD) profiles to solve the one-dimensional (1D) subsurface heat transport equation by Bredehoeft and Papadopulos (1965),

$$\lambda_0 \frac{\partial^2 T}{\partial z^2} - q C_w \frac{\partial T}{\partial z} = 0, \qquad (2.1)$$

Where λ_0 is the bulk thermal conductivity of the saturated sediment (W m^{-1} $°C^{-1}$), T is the temperature (°C), z is the sediment depth (m), q is the vertical flux (positive downwards, m s^{-1}), and C_w is the volumetric heat capacity of the water (J m^{-3} $°C^{-1}$).

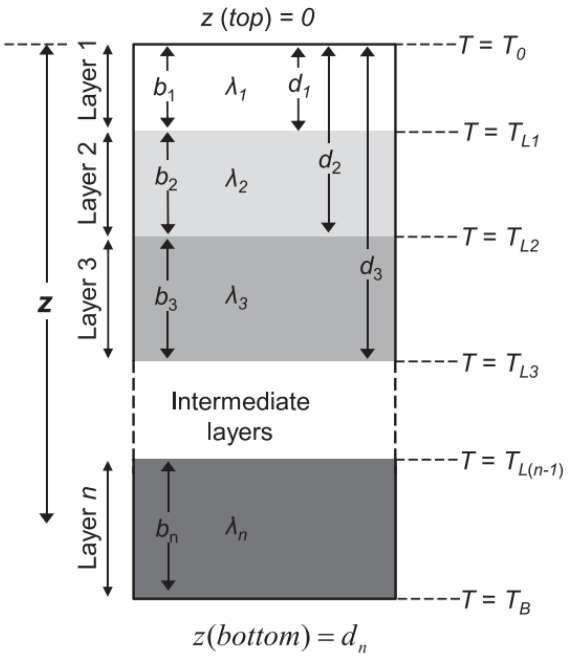

Figure 2-2: Diagram of an n-layered medium. (From Kurylyk et al., 2017)

The boundary conditions at the top and bottom of the domain are as follows:

$$T_1(z = 0) = T_0 \tag{2.2}$$

$$T_n(z = d_n) = T_B \tag{2.3}$$

The analytical solution provided by Bredhoeft and Papadopulous has been extended to allow for variations in thermal conductivity with layers in depth (Kurylyk et al., 2017). Temperature distributions must converge at the layer interfaces and the boundary conditions are as follows.

$$T_i(z = d_i) = T_{i+1}(z = d_i) = T_{Li} \quad (i = 1, 2, \dots, n-1), \tag{2.4}$$

The Flux-LM spreadsheet tool solves the homogenous ordinary differential Equation 2.1 with a standard solution.

$$T_i(z) = C_{i1} \exp\left(\frac{qz}{\gamma_i}\right) + C_{i2} \quad (i = 1, 2, \dots, n) \tag{2.5}$$

2.1.6 SPATIAL HETEROGENEITY

The parameters used in describing flow and transport are most commonly heterogeneous in practice. This is often difficult to accurately represent or model and methodologies may be simplified through assumptions. The heterogeneity of porous media is directly related to the connectivity patterns of a GW-SW system (Renard & Allard, 2013).

Geologic heterogeneity causes spatial and temporal variability when delineating various parameters. This influences understanding and characterizing the GW-SW interactions. Most notably, variations in the hydraulic conductivity parameter, a direct relationship of the streambed sediments, will cause variability in GW-SW exchange flow paths (Tonina & Buffington, 2007). Spatial changes in hydraulic conductivity will result in distinct areas of upwelling or downwelling, caused by varying levels of preferential flow paths within a streambed (Wondzell et al., 2019) . These spatial variations can exist both vertically and laterally, adding to the complexity. Sediment layering caused by fluvial deposition along the streambed can cause vertical anisotropy, creating differences in lateral and vertical flow paths (Krause et al., 2011).

2.2 GEOPHYSICAL TECHNIQUES

2.2.1 DC RESISTIVITY

DC resistivity is one of the oldest and most well-established geophysical methods. In essence, it involves the induction of electrical current into the subsurface through an external source, and variations in subsurface resistivity are measured. Interpretation of field measurements are used in a vast range of applications, such as: archaeological investigations (Gaffney, 2008; Hemeda, 2013; Tsokas et al., 2008), geological investigations (Carrière et al., 2013; Storz et al., 2000), hydrogeological exploration and monitoring (Coscia et al., 2011; Robert et al., 2012), contaminant investigation (Naudet et al., 2004; Vaudelet et al., 2011) and various engineering applications (Chambers et al., 2006; Friedel et al., 2006). ERT is so widely appreciated because the surveys are relatively easy to carry out, instrumentation is inexpensive, data processing tools are widely available, and the relationships between resistivity and hydrological properties, such as porosity

and moisture content, are reasonably well established (Binley & Kemna, 2005). This section examines the basic theory of ERT and characterizing measurements in subsurface investigations.

2.2.1.1 BASIC THEORY

DC resistivity surveys operate on the basis of Ohm's Law that governs the flow of current in the ground. The equation for Ohm's Law in vector form for current flow in a continuous medium is given by (Tsourlos, 1995):

$$J = \sigma E, \tag{2.6}$$

where σ is the conductivity of the medium, J is the current density and E is the electric field intensity. In field practice, electric field potential (Φ) is measured. The relationship between the electric potential and the field intensity is determined by:

$$E = -\nabla\Phi \tag{2.7}$$

Combining Equations 2.1 and 2.2 results in:

$$J = -\sigma\nabla\Phi \tag{2.8}$$

The DC method is used by introducing an electrical current into the subsurface to create an artificial field in which the potential difference is measured between injection and monitoring electrodes. Figure 2-3 illustrates a single injection point source of current on the surface of a semi-infinite conducting layer of a homogenous medium.

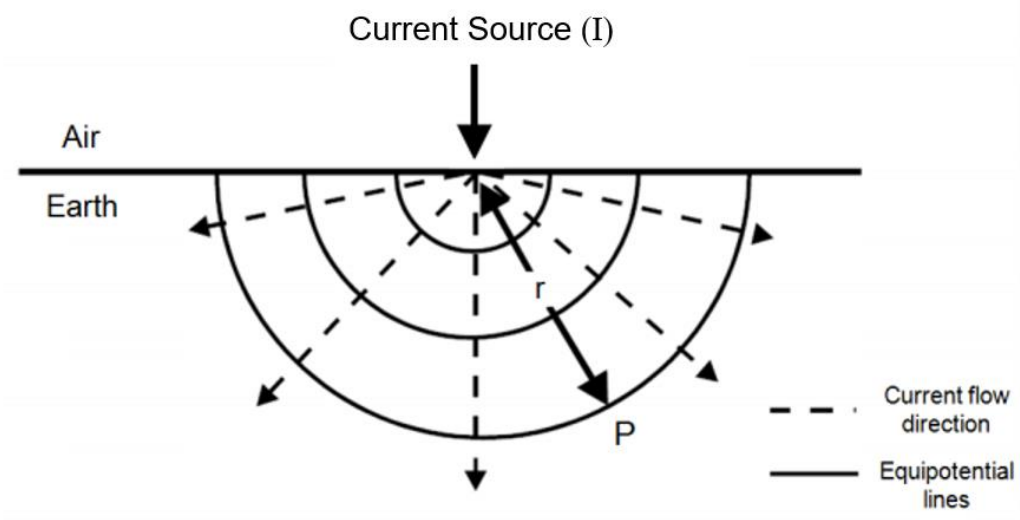

Figure 2-3: Current propagation from point source and resulting equipotential surfaces.

Located above the injection site is the surrounding atmosphere with infinite resistance. Therefore, the injected current source I flows radially in all directions (in a homogenous and isotropic medium), creating a hemispherical distribution shell of resistivity ρ. At a radial distance r from the current point source, the surface area of the hemisphere is $2\pi r^2$, resulting in the electrical potential at point P represented by (Tsourlos, 1995):

$$\Phi_P = \frac{I\rho}{2\pi r} \tag{2.9}$$

Surveys use at least two current electrodes, one positive and one negative. This is illustrated in Figure 2-4 as electrode A is positive and sends current into the subsurface and electrode B is negative and collects the returning current, acting as the source and sink, respectively.

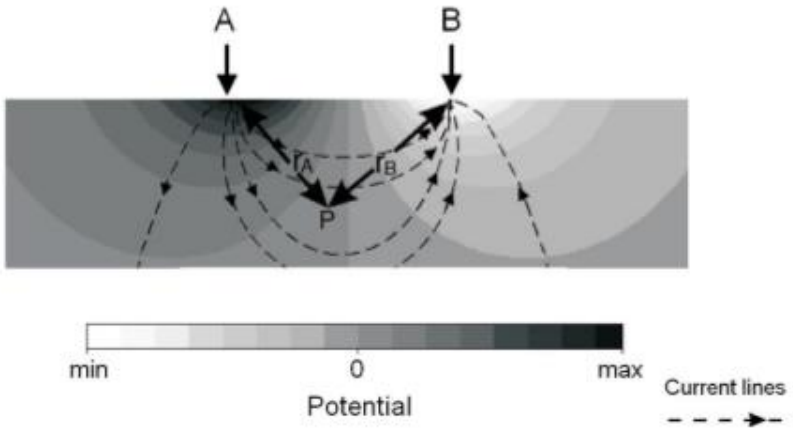

Figure 2-4: Equipotential surfaces and current propagation lines from two point source electrodes (Tsourlos, 1995)

The electrical potential at point P is represented by:

$$\Phi_P = \frac{I\rho}{2\pi}\left(\frac{1}{r_A} - \frac{1}{r_B}\right) \tag{2.10}$$

where r_A and r_B are the radial distances from electrodes A and B, respectively. In practice two pairs of electrodes are used. Similar to the above, but now the first pair is used to inject the current into the ground and the second to measure potential difference in the vicinity of current flow. This is shown in Figure 2-4, where electrodes A and B inject current I, while electrodes M and N act as potential electrodes, measuring the potential voltage, over an assumed homogenous and isotropic medium.

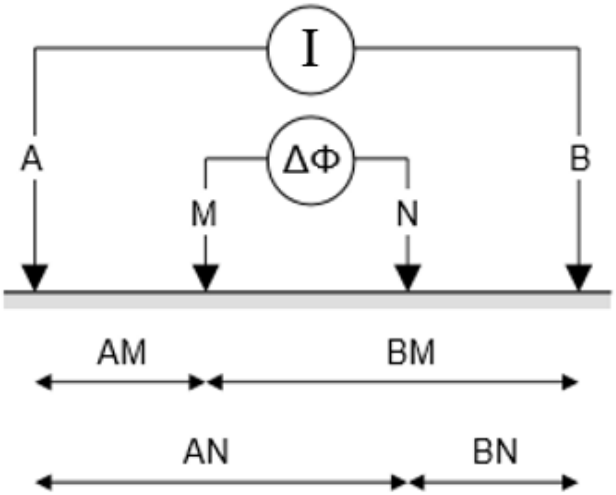

Figure 2-5: Example of simple four-electrode array. A and B are current electrodes, M and N are potential electrodes.

The electrical potential measured by electrodes M and N can be determined using equation.

$$\Phi_M = \frac{I\rho}{2\pi}\left(\frac{1}{AM} - \frac{1}{BM}\right) \tag{2.11}$$

$$\Phi_N = \frac{I\rho}{2\pi}\left(\frac{1}{AN} - \frac{1}{BN}\right) \tag{2.12}$$

The difference in electrical potential between M and N is therefore determined to be:

$$\Delta\Phi = \Phi_M - \Phi_N = \frac{I\rho}{2\pi}\left(\frac{1}{AM} - \frac{1}{BM} - \frac{1}{AN} + \frac{1}{BN}\right) \tag{2.13}$$

It is understood that in nearly all field surveys the subsurface is a heterogeneous medium, where the sediments are changing spatially in three dimensions. The observed resistivity values are considered the 'apparent' resistivity, which is not the true resistivity of the subsurface but instead can be thought of a weighted average of the subsurface. The apparent resistivity is represented by:

$$\rho_a = \mathrm{k}\left(\frac{\Delta\Phi}{I}\right) \tag{2.14}$$

Where k is a geometrical factor that is dependent on the electrode configuration. Examples of various configurations are discussed in section 2.2.3.

2.2.1.2 TYPICAL MEASUREMENTS

Measured resistivity values represent the difficulty in which electrical current is passing through the subsurface. This parameter is generally most affected by certain characteristics of the subsurface such as: the distribution of the water table, chemical composition and concertation of salts within the water, the soil grain sizes, porosity, consolidation and temperature. Typical resistivity ranges of rocks, soils and mineral are shown in Figure 2-6.

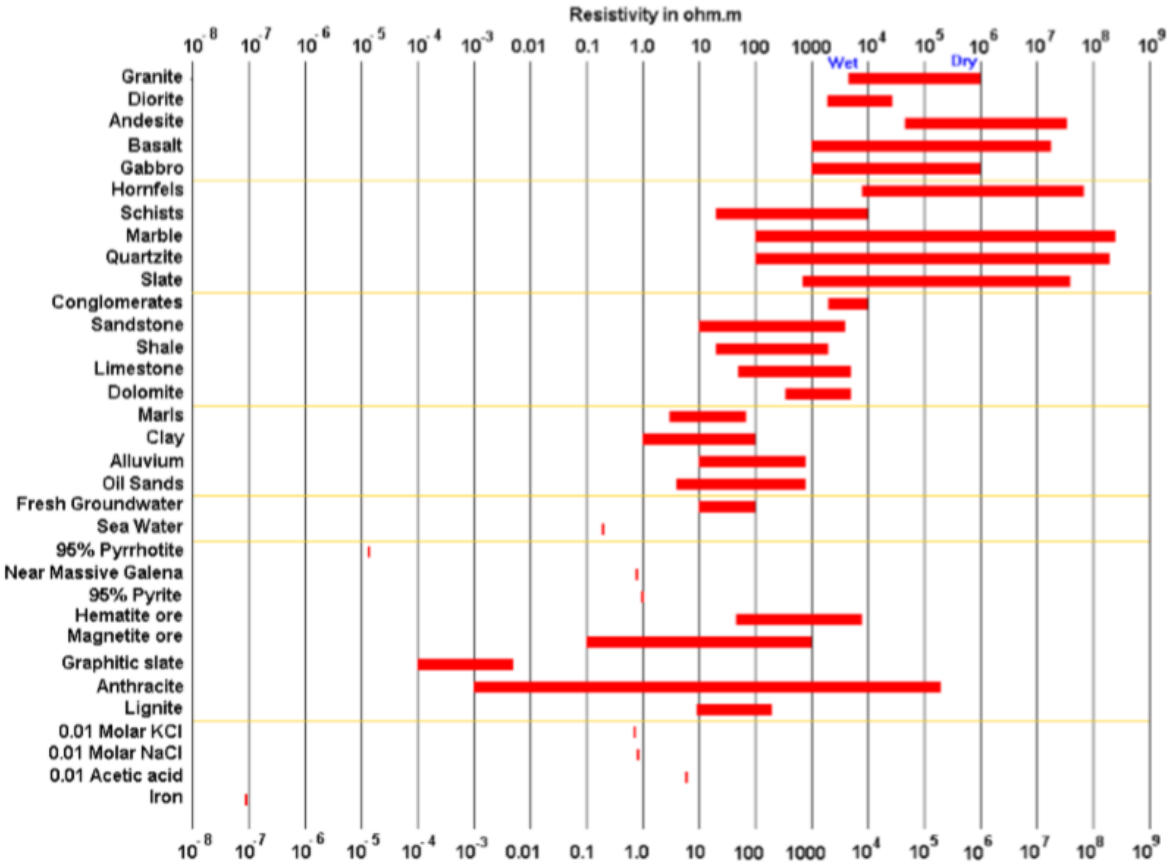

Figure 2-6: Resistivity ranges of rocks, soils, minerals and water (From Loke, 2015)

2.2.2 INDUCED POLARIZATION

Induced polarization (IP) is conducted and measured in a similar fashion to DC resistivity but measures the chargeability. Chargeability is affected by the induced polarization effect, which represents the degree to which the subsurface can receive and store an electric charge. The understanding of the combined physical and chemical characteristics causing the phenomenon are

quite complex, but it is generally thought to be affected by two main mechanisms: membrane polarization, caused largely due to clay and minerals present, and electrode polarization, caused by conductive materials (Kiberu, 2002; Loke et al., 2013). Several of the benefits of ERT are also advantageous in IP surveys, making them a popular geophysical method in applications of mineral exploration (Bigalke & Junge, 1999), contaminant monitoring (Sogade et al., 2006), mining investigations (Campbell et al., 1998; Power et al., 2018) and various environmental and engineering applications (Gazoty et al., 2012; Slater & Lesmes, 2002). This section examines the basic theory of IP and characterizing measurements in subsurface investigations.

2.2.2.1 BASIC THEORY

Induced polarization is a dimensionless quantity in theory. However, in practice it is measured as a change in voltage with respect to either time or frequency.

Time-Domain Method

In the time-domain method, the IP effect measures the residual voltage after the current is removed. It is expressed by the term chargeability *m* and is given by (Seigel, 1959):

$$m = \frac{V_s}{V_P} \tag{2.15}$$

where V_p is the on-time measured voltage and V_s is the off-time measured voltage. In practice, it is very difficult to measure V_s at the exact moment the current is switch off due to electromagnetic effects. Therefore, it is generally measured at a specific time after removing current (e.g. 1s after), and measurements are taken of the decay of V_s over a short time-frame. The integration of the voltage over a discrete time interval (t_1 - t_2) is shown in Figure 2-7 and describes the measured chargeability:

$$m = \frac{1}{V_P}\int_{t1}^{t2} V_s * dt \tag{2.16}$$

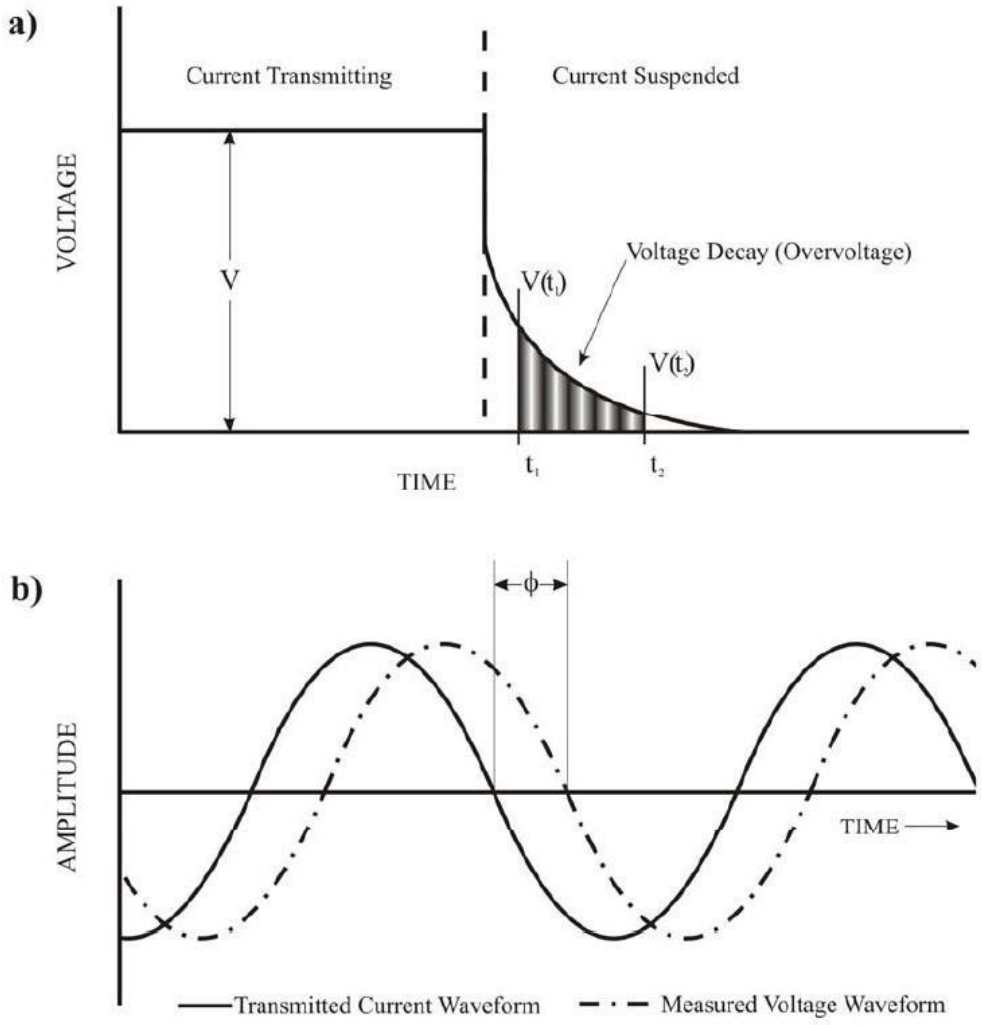

Figure 2-7: Measurement of a) time-domain induced and b) frequency-domain polarization. (Modified from Kiberu, 2002)

Frequency-Domain Method

In frequency-domain methods, measurements are made using at least two different frequencies, a high and low frequency. Comparative measurements are taken of either the steady stage voltage response or of the apparent resistivity values at the assigned high and low frequencies. This can be described as the Frequency Effect (Kiberu, 2002):

$$FE = \frac{V_{lo} - V_{hi}}{V_{hi}}, FE = \frac{\rho_{lo} - \rho_{hi}}{\rho_{hi}} \quad (2.17)$$

Typically, the Frequency Effect is expressed as the Percentage Frequency Effect:

$$PFE = \frac{\rho_{lo} - \rho_{hi}}{\rho_{hi}} * 100 \quad (2.18)$$

2.2.2.2 TYPICAL MEASUREMENTS

As previously mentioned, chargeability is a materials ability to secure and hold an electric charge. Similar to DC, IP measurements are affected by lithology, pore fluid chemistry and water content, but are more affected by the presence of clay and minerals present in the subsurface than DC results. Typical chargeability ranges of rocks and minerals are shown in Figure 2-8.

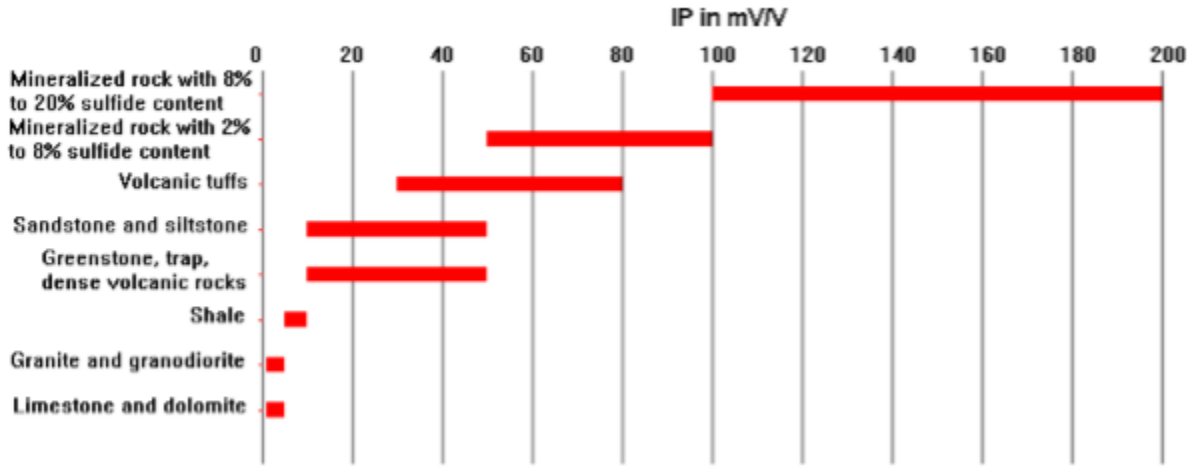

Figure 2-8: IP ranges of rocks, soils, minerals and water (From Loke, 2015)

2.2.3 ELECTRODE CONFIGURATIONS

The electrode configuration selected will depend on the aim of a given survey, as differing array configurations are more suitable depending on the geometrical shape, size and resolution of the desired 'image'. Each electrode array results in different sensitivities in regard to lateral and vertical variations in resistivity, depth of investigation and signal-to-noise ratios. DC surveys are generally identified according to the arrangement of the current and potential electrodes. The most common arrays include Wenner, Schlumberger, dipole-dipole, pole-dipole, and pole-pole. The configurations of these arrays are shown in Figure 2-9. As mentioned in Section 2.2.1.1, the geometrical factor is dependent on the array configuration, and is given as:

$$k = \frac{2\pi}{\left(\frac{1}{AM} - \frac{1}{BM} - \frac{1}{AN} + \frac{1}{BN}\right)} \quad (2.19)$$

where AM, BM, AN and BN are the radial distances to a point P in the subsurface, based on the respective array.

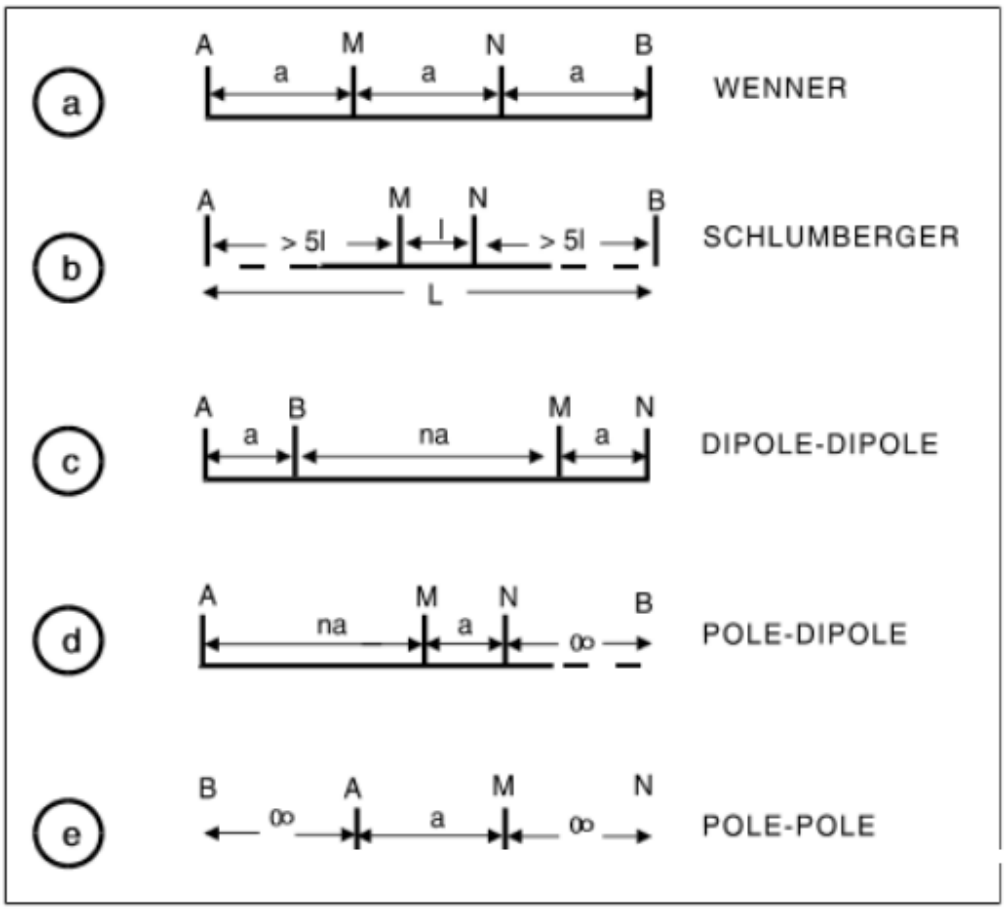

Figure 2-9: Basic resistivity arrays. (Tsourlos, 1995)

In the field, the IP electrode system is the same as the resistivity system, so electrode arrays such as Wenner, Schlumberger, Pole–dipole and double dipole are used.

2.2.4 MODELLING AND INVERSION

As previously mentioned, the ultimate goal of geophysical methods is to produce an ‘image’ of the target area within the subsurface. The theoretical outcome of measurements can be determined (modeled) for given electrical properties. This is referred to as the “forward modelling” problem. Conversely, given a set of collected field measurements, the distribution of electrical properties is sought to be determined that accurately represent the measurements, within an acceptable error.

This is referred to as the “inversion” problem. The following section describes various techniques to solve both problems.

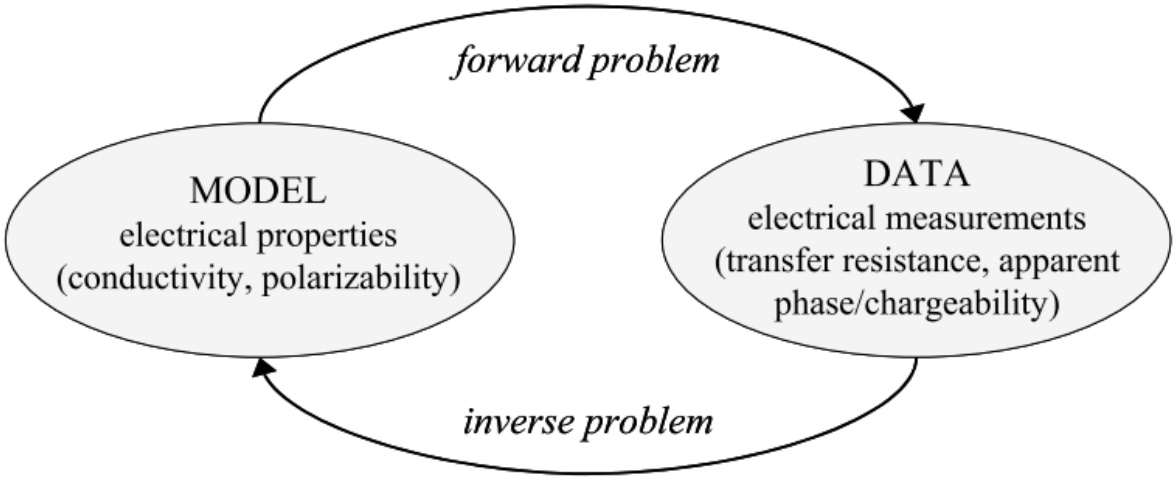

Figure 2-10: Linkage between forward and inverse modelling.

2.2.4.1 FORWARD MODELLING

To predict a theoretical value that would provide a solution to the below defined equations is considered forward modelling. There are several methods to solve the forward modelling problem. They are generally separated into two groups: analytical solutions and numerical models. Analytical solutions are more accurate but are restricted to relatively simplistic geological geometries. It is understood that in practice, site investigations are seldom truly homogenous and isotropic, making them complex and more suitable to be solved using numerical modelling.

DC Resistivity

In the majority of resistivity surveys, current sources are in the form of point sources. In this case, over an elemental volume surrounding the current source I, located at (x_s, y_s, z_s), the relationship between the current density and the current is given by (Dey and Morrison, 1979a):

$$\nabla \mathrm{J} = \left(\frac{I}{\nabla V}\right)\delta(x - x_s)\delta(y - y_s)\delta(z - z_s) \qquad (2.20)$$

where δ is the Dirac delta function. Equation 3 can be rewritten as:

$$\nabla[\sigma(x,y,z)\nabla\Phi(x,y,z)] = \left(\frac{I}{\nabla V}\right)\delta(x-x_s)\delta(y-y_s)\delta(z-z_s) \qquad (2.21)$$

This partial differential equation represents the potential distribution in the ground due to a current point source.

IP

Forward modelling solutions are also available for IP data, an example is given by Li & Oldenburg (2000):

$$m = \frac{f[(1-m)\sigma]-f[\sigma]}{f[(1-m)\sigma]} \qquad (2.22)$$

where f represents the forward modelling operator for the conductivity distributions mentioned in section 2.2.1.

2.2.4.2 INVERSION

Inversion is required to invert the apparent electrical values obtained during ERT surveys to obtain the distribution of true electrical properties. Inversion is a very rich field of research and inversion schemes are being continuously improved and developed, resulting in more accurate and valuable results from electrical measurements. Numerous inversion codes have been developed over the years and can be applied to the various survey approaches, including 2D and 3D surveys (e.g., Loke and Barker, 1996; Tsourlos and Ogilvy, 1999), in surface, borehole and underwater surveys (e.g., LaBrecque et al., 1996), and in static and time-lapse modes (e.g., Karaoulis et al., 2013).

2.3 GEOPHYSICAL TECHNIQUES USED IN GROUNDWATER-STREAM WATER INVESTIGATIONS

Using geophysical techniques in various hydrogeological investigations has been explored and developed within the field of 'hydrogeophysics'. The use of geophysical 'imaging' of the structural subsurface of a GW-SW system is a non-invasive technique in characterization of exchanges (Binley et al., 2015). Table 2-2 shows some typical geophysical techniques and the environmental parameters that are to be investigated. Also shown are the typical resolution depths and investigation time required. The use of geophysical techniques allows for more understanding of the spatial and temporal heterogeneities that exist in GW-SW systems subsurface. The

measurement density of these methods are not well achieved by traditional hydrogeological methods as mentioned in section 2.1.5, many of which are also indirect. Coring techniques can provide the most assured site data but is spatially limited and invasively destructive (Crook et al., 2008).

The most effective geophysical survey would be a high resolution, 3-Dimensional time-lapse investigation. This would allow for the most information regarding a GW-SW system to be collected and interpreted. However, this extent of a survey would be time consuming and not the most cost effective approach, and therefore is seldom used.

Table 2-2: Geophysical techniques, their associated measured geophysical property and the hydraulic parameters which they relate to. Typical investigation depths and acquisition times are also included. (Modified from McLachlan et al., 2017)

Geophysical technique	**Geophysical properties**	**Examples of derived environmental parameters**	**Typical Investigation Depths**	**Typical acquisition time for 100 m transect**
Electrical Resistivity	Electrical Conductivity	Water content, clay content, pore water conductivity, porosity, stratigraphy	Metres to tens of metres	Tens of minutes
Induced Polarization	Electrical Conductivity, chargeability	Water content, clay content, pore water conductivity, porosity, stratigraphy	Metres to tens of metres	Tens of minutes to hours
Ground penetrating radar	Dielectric permittivity, electrical conductivity	Water content, porosity, stratigraphy	Metres to tens of metres	Minutes to tens of minutes
Seismic	Bulk density, elastic moduli	Porosity, stratigraphy	Metres to tens of metres	Tens of minutes

2.4 SUMMARY & DATA GAPS

This chapter highlighted the importance of understanding GW-SW interactions on a local scale. As identified in Section 2.1.5, a major challenge in GW-SW investigations is determining the hydraulic properties of the subsurface. Traditional techniques are usually spatially limited and can often times be invasive and compromising of local interactions. Given the true spatial and temporal heterogeneity of the subsurface, many of these techniques do not provide the sampling density to accurately characterize subsurface properties in space or time. The direct observation of spatial exchange fluxes between groundwater and streams remains a challenge.

There is a need to combine the traditional hydrogeological techniques with high-sampling density geophysical techniques to assess the areas of connectivity most effectively, to aide in the characterization of GW-SW interactions. Chapter 3 of this thesis presents a study focused on a headwater stream located in southwestern Ontario in which high activities of GW-SW exchanges well recorded. It is also noted that high levels of nutrient contaminants (phosphorous) were detected in the stream reach, allowing for the potential linkages to be made with this study and a partnered research study. High resolution, 3D DC and IP surveys were conducted in the stream reach and the adjacent riparian zone, as well as several traditional hydrogeological techniques. Following detailed analysis, concordances were identified in various methodologies to characterize the GW-SW relations most effectively.

2.5 REFERENCES

Berryman, C. J. (2005), Tracer tests for investigating flow and transport in the hyporheic zone, Science Report SC030155/8, 41 pp, Environment Agency, Bristol.

Bigalke, J., & Junge, A. (1999). Using evidence of non-linear induced polarization for detecting extended ore mineralizations. *Geophysical Journal International*, *137*(2), 516–520. https://doi.org/10.1046/j.1365-246X.1999.00805.x

Binley, A., Hubbard, S. S., & Huisman, J. a. (2015). The emergence of hydrogeophysics for improved understanding of subsurface processes over multiple scales. *Water Resources Research*, 1–30. https://doi.org/10.1002/2015WR017016.Received

Binley, A., & Kemna, A. (2005). *Hydrogeophysics* (Y. Rubin & S. S. Hubbard (eds.); Vol. 50, Issue October 2016). Springer Netherlands. https://doi.org/10.1007/1-4020-3102-5

Bredehoeft, J. D., and I. S. Papadopulos (1965), Rates of vertical ground-water movement estimated from the Earth's thermal profile, Water Resour. Res., 1(2), 325-328.

Buss SR, Cai Z, Cardenas MB, Fleckenstein JH, Hannah DM, Heppell K, H. P., Ibrahim T, Kaeser D, Krause S, Lawler DM, Lerner DN, Mant J, Malcolm IA, O. G., Parkin G, Pickup RJ, Pinay G, Porter J, Rhodes G, Richie A, Riley J, Robertson A, S. D., & Shields B, Smith JWS, Tellam JH, W. P. (2009). The Hyporheic Handbook A handbook on the groundwater – surface water interface and hyporheic zone for environment managers Integrated catchment science programme Science report : SC050070 The Environment Agency is the leading public body protecting and im. In *Hydrogeology Journal* (Vol. 11, Issue 3). https://assets.publishing.service.gov.uk/government/uploads/system/uploads/attachment_data/file/291621/scho1009brdx-e-e.pdf

Campbell, D. L., Fitterman, D. V., Hein, A. S., & Jones, D. P. (1998). Spectral Induced Polarization Studies of Mine Dumps Near Silverton, Colorado. *Symposium on the Application of Geophysics to Engineering and Environmental Problems 1998*, *6*(1), 761–769. https://doi.org/10.4133/1.2922567

Carrière, S. D., Chalikakis, K., Sénéchal, G., Danquigny, C., & Emblanch, C. (2013). Combining

Electrical Resistivity Tomography and Ground Penetrating Radar to study geological structuring of karst Unsaturated Zone. *Journal of Applied Geophysics*, *94*, 31–41. https://doi.org/10.1016/j.jappgeo.2013.03.014

Chambers, J. E., Kuras, O., Meldrum, P. I., Ogilvy, R. D., & Hollands, J. (2006). Electrical resistivity tomography applied to geologic, hydrogeologic, and engineering investigations at a former waste-disposal site. *Geophysics*, *71*(6). https://doi.org/10.1190/1.2360184

Conant, B., Robinson, C. E., Hinton, M. J., & Russell, H. A. J. (2019). A framework for conceptualizing groundwater-surface water interactions and identifying potential impacts on water quality, water quantity, and ecosystems. *Journal of Hydrology*, *574*(March), 609–627. https://doi.org/10.1016/j.jhydrol.2019.04.050

Coscia, I., Greenhalgh, S. A., Linde, N., Doetsch, J., Marescot, L., GuNther, T., Vogt, T., & Green, A. G. (2011). 3D crosshole ERT for aquifer characterization and monitoring of infiltrating river water. *Geophysics*, *76*(2). https://doi.org/10.1190/1.3553003

Crook, N., Binley, A., Knight, R., Robinson, D. A., Zarnetske, J., & Haggerty, R. (2008). Electrical resistivity imaging of the architecture of substream sediments. *Water Resources Research*, *46*(4), 1–11. https://doi.org/10.1029/2008WR006968

Dahl, M., Nilsson, B., Langhoff, J. H., & Refsgaard, J. C. (2007). Review of classification systems and new multi-scale typology of groundwater-surface water interaction. *Journal of Hydrology*, *344*(1–2), 1–16. https://doi.org/10.1016/j.jhydrol.2007.06.027

Fetter, C. W. (2001), Applied hydrogeology, 4th ed., 598 pp., Pearson Education, Upper Saddle River, NJ.

Freeze, R. A., and J. A. Cherry (1979), Groundwater, 604 pp., Prentice-Hall, Englewood Cliffs, NJ.

Friedel, S., Thielen, A., & Springman, S. M. (2006). Investigation of a slope endangered by rainfall-induced landslides using 3D resistivity tomography and geotechnical testing. *Journal of Applied Geophysics*, *60*(2), 100–114. https://doi.org/10.1016/j.jappgeo.2006.01.001

Gaffney, C. (2008). Detecting trends in the prediction of the buried past: A review of geophysical techniques in archaeology. *Archaeometry*, *50*(2), 313–336. https://doi.org/10.1111/j.1475-4754.2008.00388.x

Gazoty, A., Fiandaca, G., Pedersen, J., Auken, E., & Christiansen, A. V. (2012). Mapping of landfills using time-domain spectral induced polarization data: The Eskelund case study. *Near Surface Geophysics*, *10*(6), 575–586. https://doi.org/10.3997/1873-0604.2012046

Hamilton, P. (2005). Groundwater and surface water: A single resource. *Water Environment and Technology*, *17*(5), 37–41.

Hannah, D. M., Malcolm, I. A., & Bradley, C. (2009). Seasonal hyporheic temperature dynamics over riffle bedforms. *Hydrological Processes*, *23*(15), 2178–2194. https://doi.org/10.1002/hyp.7256

Harvey, J. W., and B. J. Wagner (2000), Quantifying hydrologic interactions between streams and their subsurface hyporheic zones, in Streams and ground waters, edited by J. B. Jones and P. J. Mulholland, pp. 3-44, Academic Press, San Diego.

Hemeda, S. (2013). Electrical Resistance Tomography (ERT) Subsurface Imaging for Non-destructive Testing and Survey in Historical Buildings Preservation. *Australian Journal of Basic and Applied Sciences*, *June*, 344–357.

Hornberger, G. M., J. P. Raffensberger, P. L. Wiberg, and K. N. Eshleman (1998), Elements of Physical Hydrology, 302 pp., The Johns Hopkins University Press, Baltimore.

Irvine, D. J., Kurylyk, B. L., & Briggs, M. A. (2020). Quantitative guidance for efficient vertical flow measurements at the sediment–water interface using temperature–depth profiles. *Hydrological Processes*, *34*(3), 649–661. https://doi.org/10.1002/hyp.13614

Kalbus, E., Reinstorf, F., & Schirmer, M. (2006). Measuring methods for groundwater – surface water interactions: a review. *Hydrology and Earth System Sciences*, *10*(6), 873–887. https://doi.org/10.5194/hess-10-873-2006

Karaoulis, M., A. Revil, P. Tsourlos, D.D. Werkema, and B.J. Minsley. 2013. IP4DI: A software

for time-lapse 2D/3D DC-resistivity and induced polarization tomography. Computers & Geosciences, 54(0): 164-170.

Khan, H. H., & Khan, A. (2019). Groundwater and surface water interaction. In *GIS and Geostatistical Techniques for Groundwater Science* (Issue 2000). Elsevier Inc. https://doi.org/10.1016/B978-0-12-815413-7.00014-6

Kiberu, J. (2002). Induced polarization and Resistivity measurements on a suite of near surface soil samples and their empirical relationship to selected measured engineering parameters. *Interntional Institute for Geo-Information Science and Earth Observation Enschede, The Netherlands*, 119.

Krause, S., Hannah, D. M., Fleckenstein, J. H., Heppell, C. M., Kaeser, D., Pickup, R., Pinay, G., Robertson, A. L., & Wood, P. J. (2011). Inter-disciplinary perspectives on processes in the hyporheic zone. *Ecohydrology*, *4*(4), 481–499. https://doi.org/10.1002/eco.176

Kurylyk, B. L., Irvine, D. J., Carey, S. K., Briggs, M. A., Werkema, D. D., & Bonham, M. (2017). Heat as a groundwater tracer in shallow and deep heterogeneous media: Analytical solution, spreadsheet tool, and field applications. *Hydrological Processes*, *31*(14), 2648–2661. https://doi.org/10.1002/hyp.11216

LaBrecque, D.J., M. Miletto, W. Daily, A. Ramirez, and E. Owen. 1996. The effect of noise on Occam inversion of resistivity tomography data. Geophysics, 61: 538-548.

Li, Y., & Oldenburg, D. W. (2000). 3-D inversion of induced polarization data. *Geophysics*, *65*(6), 1931–1945. https://doi.org/10.1190/1.1444877

Loke, M.H., and R.D. Barker. 1996. Practical techniques for 3D resistivity surveys and data inversion. Geophy. Prosp., 44: 499-524

Loke, M. H., Chambers, J. E., Rucker, D. F., Kuras, O., & Wilkinson, P. B. (2013). Recent developments in the direct-current geoelectrical imaging method. *Journal of Applied Geophysics*, *95*, 135–156. https://doi.org/10.1016/j.jappgeo.2013.02.017

Loke M. H. (2015). 2-D and 3-D Electrical Imaging Surveys. *Tutorial*, *May*, 51–52.

McLachlan, P. J., Chambers, J. E., Uhlemann, S. S., & Binley, A. (2017). Geophysical characterisation of the groundwater–surface water interface. *Advances in Water Resources*, *109*(August), 302–319. https://doi.org/10.1016/j.advwatres.2017.09.016

Naudet, V., Revil, A., Rizzo, E., Bottero, J. Y., & Bégassat, P. (2004). Groundwater redox conditions and conductivity in a contaminant plume from geoelectrical investigations. *Hydrology and Earth System Sciences*, *8*(1), 8–22. https://doi.org/10.5194/hess-8-8-2004

Poole, G. C., O'Daniel, S. J., Jones, K. L., Woessner, W. W., Bernhardt, E. S., Helton, A. M., Stanford, J. A., Boer, B. R., & Beechie, T. J. (2008). Hydrologic spiralling: the role of multiple interactive flow paths in stream ecosystems. *River Research and Applications*, *24*(7), 1018–1031. https://doi.org/10.1002/rra.1099

Power, C., Tsourlos, P., Ramasamy, M., Nivorlis, A., & Mkandawire, M. (2018). Combined DC resistivity and induced polarization (DC-IP) for mapping the internal composition of a mine waste rock pile in Nova Scotia, Canada. *Journal of Applied Geophysics*, *150*, 40–51. https://doi.org/10.1016/j.jappgeo.2018.01.009

Renard, P., & Allard, D. (2013). Connectivity metrics for subsurface flow and transport. *Advances in Water Resources*, *51*, 168–196. https://doi.org/10.1016/j.advwatres.2011.12.001

Robert, T., Caterina, D., Deceuster, J., Kaufmann, O., & Nguyen, F. (2012). A salt tracer test monitored with surface ERT to detect preferential flow and transport paths in fractured/karstified limestones. *Geophysics*, *77*(2). https://doi.org/10.1190/geo2011-0313.1

Seigel, H. O. (1959). MATHEMATICAL FORMULATION AND TYPE CURVES FOR INDUCED POLARIZATION. *GEOPHYSICS*, *24*(3), 547–565. https://doi.org/10.1190/1.1438625

Slater, L. D., & Lesmes, D. (2002). IP interpretation in environmental investigations. *Geophysics*, *67*(1), 77–88. https://doi.org/10.1190/1.1451353

Smith, J. W. N. (2005). Groundwater – surface water interactions in the hyporheic zone. In *Environment Agency Science report SC030155/SR1, Environment Agency: Bristol, UK*.

www.environment-agency.gov.uk

Sogade, J. A., Scira-Scappuzzo, F., Vichabian, Y., Shi, W., Rodi, W., Lesmes, D. P., & Morgan, F. D. (2006). Induced-polarization detection and mapping of contaminant plumes. *Geophysics*, *71*(3). https://doi.org/10.1190/1.2196873

Sophocleous, M. (2002). Interactions between groundwater and surface water: The state of the science. *Hydrogeology Journal*, *10*(1), 52–67. https://doi.org/10.1007/s10040-001-0170-8

Stonestrom, D., & Constantz, J. (2003). Heat as a tracer to determine streambed water exchanges. *Water Resources Research*, *44*(4). https://doi.org/10.1029/2008WR006996

Storz, H., Storz, W., & Jacobs, F. (2000). Electrical resistivity tomography to investigate geological structures of the earth's upper crust. *Geophysical Prospecting*, *48*(3), 455–471. https://doi.org/10.1046/j.1365-2478.2000.00196.x

Tonina, D., & Buffington, J. M. (2007). Hyporheic exchange in gravel bed rivers with pool-riffle morphology: Laboratory experiments and three-dimensional modeling. *Water Resources Research*, *43*(1), 1–16. https://doi.org/10.1029/2005WR004328

Tsokas, G. N., Tsourlos, P. I., Vargemezis, G., & Novack, M. (2008). Non-destructive electrical resistivity tomography for indoor investigation: The case of Kapnikarea Church in Athens. *Archaeological Prospection*, *15*(1), 47–61. https://doi.org/10.1002/arp.321

Tsourlos, P. (1995). Modelling, Interpretation and Inversion of Multielectrode Resistivity Survey Data. *University of York, November*, 294.

Tsourlos, P., and R. Ogilvy. 1999. An algorithm for the 3-D inversion of tomographic resistivity and induced polarization data: preliminary results. Journal of the Balkan Geophysical Society, 2: 30-45.

Vaudelet, P., Schmutz, M., Pessel, M., Franceschi, M., Guérin, R., Atteia, O., Blondel, A., Ngomseu, C., Galaup, S., Rejiba, F., & Bégassat, P. (2011). Mapping of contaminant plumes with geoelectrical methods. A case study in urban context. *Journal of Applied Geophysics*, *75*(4), 738–751. https://doi.org/10.1016/j.jappgeo.2011.09.023

Vienken, T., and P. Dietrich (2011), Field evaluation of methods for determining hydraulic conductivity from grain size data, J. Hydrol., 400(1-2), 58-71, doi: 10.1016/j.jhydrol.2011.01.022. Vieweg,

Winter, T. C., Harvey, J. W., & Alley, W. M. (1998). *Ground water and surface water a single resource: U* (Issue May). https://doi.org/10.3133/cir1139

Woessner, W. W. (2000). Stream and Fluvial Plain Ground Water Interactions: Rescaling Hydrogeologic Thought. *Ground Water*, *38*(3), 423–429. https://doi.org/10.1111/j.1745-6584.2000.tb00228.x

Wondzell, S. M., Herzog, S. P., Gooseff, M. N., Ward, A. S., & Schmadel, N. M. (2019). Geomorphic Controls on Hyporheic Exchange Across Scales—Watersheds to Particles. In *Reference Module in Earth Systems and Environmental Sciences*. Elsevier. https://doi.org/10.1016/B978-0-12-409548-9.12135-9

3 IMPROVED CHARACTERIZATION OF GROUNDWATER-STREAM WATER INTERACTIONS THROUGH GEOPHYSICAL MEASUREMENTS OF HETEROGENEOUS STREAMBED-AQUIFER ARCHITECTURE

3.1 INTRODUCTION

Groundwater (GW) and stream (SW) water are complex interconnected components of various hydrologic systems. Understanding the interactions between GW and SW is at the forefront of many hydrogeological investigations as these interactions are intertwined in hydrological, biogeochemical and biological relationships, which have impacts on maintaining water quantity and quality standards (Conant et al., 2019; Sophocleous, 2002). For instance, harmful algae blooms from excess phosphorous are a critical issue for Lake Erie of the Great Lakes, and the Thames River watershed is known to be contributing to this issue. (Baker et al., 2019; Jarvie et al., 2017)

The complexity of GW-SW systems are due to the fact that a variety of factors can alter the outcome of interactions, including i) the distribution of hydraulic conductivity in streambed sediments, ii) the position of the stream stage with respect to the adjacent groundwater levels, and iii) the position and geometrical influence of the stream channel within the fluvial plain (Woessner, 2000). It is also understood that GW-SW interactions vary substantially in space and also potentially in time (Buss et al., 2009) , due to the variation in control factors. Therefore, to attempt to best understand the importance and potential impacts of GW-SW interactions, it is necessary to accurately characterize the streambed architecture and the connectivity and hydrogeological conditions of a streambed-aquifer system.

Streambed sediments are highly spatially heterogeneous with the physical properties of these sediments regulating GW-SW exchange fluxes and coupled abiotic/biotic reactions. As such, this streambed heterogeneity can influence the water chemistry and the ecological conditions within the streambed and in the stream itself. For instance, sediment surface area, porosity and permeability can control the fate and transport of chemicals, including nutrients, discharging or cycling across streambeds including preferential pathways, as they affect the residence time and

the geochemical conditions along discharge or hyporheic flow paths (Conant et al., 2004; Irvine et al., 2020). It is well established that at a stream-reach scale, variations in streambed lithology, and thus in streambed hydraulic properties, can impact GW-SW exchange patterns on a scale of meters to centimeters (Briggs et al., 2014; Stonestrom & Constantz, 2003). As a result, it is highly challenging to accurately characterize exchange fluxes across streambeds. While this study will focus on the physical characteristics that influence GW-SW interactions, a partner study was conducted to monitor the chemical characteristics.

Various methodologies are available to provide measurement and mapping of the spatial distribution of GW-SW exchanges across a streambed. Temperature methods (Rau et al., 2010), seepage meters (Rosenberry & LaBaugh, 2008), Darcy-based calculations with hydraulic head (Schmidt et al., 2007) and hydraulic property measurements (Tarnawski et al., 2011) are commonly used, however these methods can often be invasive, destructive, labour-intensive and difficult to properly conduct in various conditions. Furthermore, they can suffer from low sampling density and as a result, interpretations often require simplifying assumptions. For instance, temperature is often used as a tracer to identify and quantify water flux across streambeds. Several analytical solutions based on the 1-D vertical heat transport equation are available for estimating exchange fluxes using vertical temperature gradients (Gordon et al., 2012; Irvine & Lautz, 2015; Rau et al., 2010). However, the assumption in a number of analytical solutions is that the streambed is vertically homogenous (Kurylyk et al., 2017). This assumption is often required due to the lack of detailed understanding of the streambed lithology. Finally, it is noted that not all methodologies give information about the controlling factors, useful for predicting how GW-SW interactions may change with space and time.

Given the strong control by streambed-near aquifer lithology on the spatial variation in GW-SW interactions, it would be highly beneficial to have a better measure of this at small scale across an entire site, available under nearly all conditions. Geophysical techniques are an attractive option as they can provide rapid, non-invasive, and continuous information about the subsurface. Along with direct current (DC) resistivity, induced polarization (IP) in the time-domain, is the most widely applied geophysical technique in the field (e.g. Binley et al., 2015). Combined DC resistivity and time-domain IP, referred to as DC-IP, measures the variation of electrical and capacitive properties in the time-domain to produce both resistivity and chargeability distributions

of the subsurface (e.g., Soupios & Kokinou, 2017). Research and development in both DC resistivity and IP remain highly active and major advancements have helped to increase their popularity for geoenvironmental and hydrogeological investigations, including the mapping of lithology (Duvillard et al., 2018), hydraulic characteristics (e.g. Maurya et al., 2018), and subsurface contamination (e.g. Power et al., 2018).

DC-IP exhibits strong promise for improving characterization of streambed lithology and heterogeneity (e.g. Coscia et al., 2011; Crook et al., 2008), as needed to better interpret water and chemical fluxes across streambed. DC resistivity can be used to identify streambed variations due to (i) pore-water conductivity, which is a function of water saturation, ionic strength and porosity, and (ii) solid particle surface conductivity due to membrane polarization caused largely due to clay materials (Kiberu, 2002). Time-domain IP complements DC resistivity by describing mineralogy and discriminating between clayey and non-clayey soils (Slater & Lesmes, 2002; Yatini et al., 2018). Currently, the application of DC-IP for streambed characterization has been limited. Standalone DC resistivity has been applied to map streambed lithology but has been limited to two-dimensional (2D) surveys that are unable to accurately capture the 3D complexity within streambeds that typically exhibit significant variability in the longitudinal and transverse directions (Busato et al., 2019; Earon et al., 2020) While time-domain IP has not been employed for streambed characterization, frequency-domain IP was recently employed by Wang et al. (2021) to characterize physical properties of streambed sediments such as surface area; however, the dataset was limited to raw 1D measurements.

DC-IP imaging should be performed in 3D to adequately capture the high complexity and heterogeneity of streambeds. In addition to mapping lithology, it is highly beneficial to assess the relationship between lithology and GW-SW exchange patterns. This can further reinforce the value of DC-IP for mapping streambeds as it can not only be used to directly infer lithology, but also provide indirect information on GW-SW exchange.

The main objective of this study was to evaluate the potential of 3D DC-IP for characterizing the structural heterogeneities within a streambed to inform assessment of stream GW-SW interactions. A high-resolution 3D DC-IP underwater survey was conducted within a 50 m long headwater stream reach in Kintore, Ontario. The structural information from this survey was then compared

to soil characteristics from extracted soil cores, and to *in situ* temperature mapping, exchange flux measurements and vertical head differences collected within the stream, to assess the performance of 3D DC-IP relative to traditional approaches. Furthermore, this study will discuss the benefits of this integrated multi-disciplinary approach to improve interpretation of streambed heterogeneity and its influence on water exchange patterns across streambeds.

3.2 SITE DESCRIPTION

The study area was located within the Middle Thames River watershed, just north of the town of Kintore in Ontario, Canada. Geographically located in southwestern Ontario, Kintore is subjected to the Great Lakes and St. Lawrence lowlands climate region and has an average annual precipitation of 1011 mm with maximum and minimum monthly average temperatures of 20.8 °C and -5.6 °C, respectively, based on 30 years of historical data (Environment and Climate Change Canada, 2021). This 13 km^2 sub watershed lies within the Thames River watershed, which is one of the largest watersheds in the Lake Erie basin. As agriculture is the dominant land use in Kintore Creek, it was suspected that this sub watershed may be one source of phosphorous. Figure 3-1 indicates the location of Kintore Creek and its proximity to Lake Erie.

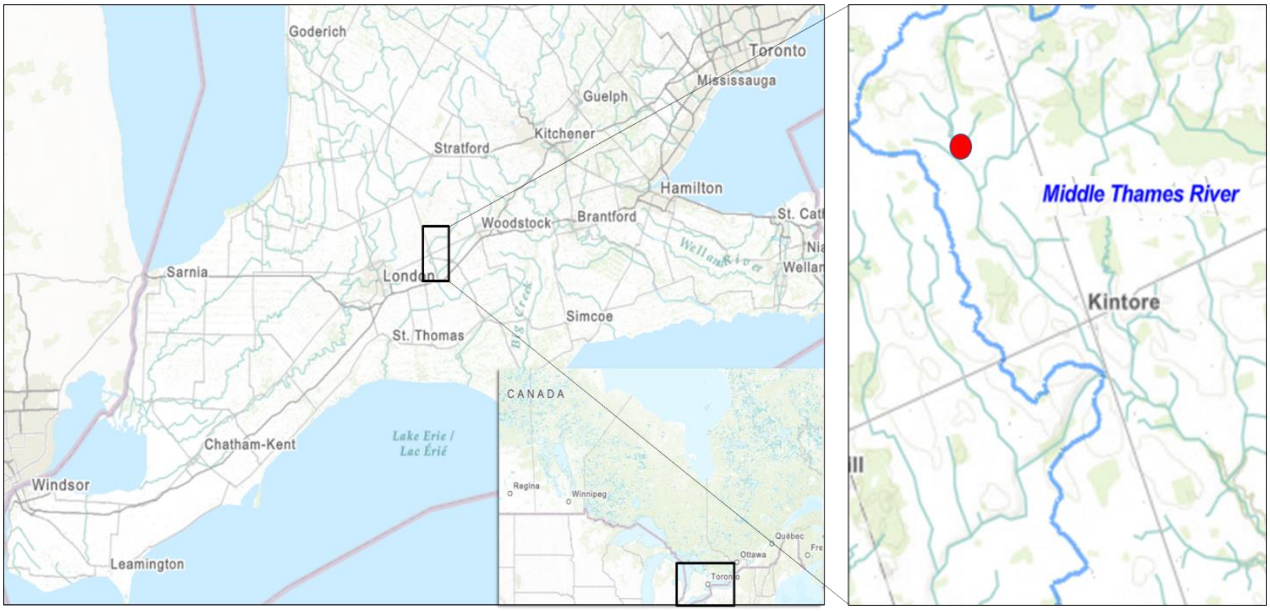

Figure 3-1: Site maps indicating the location of Kintore within southwestern Ontario.

The stream reach used in this study was identified from several preliminary surveys. First, 222-radon tracer sampling was conducted along the streams within Kintore Creek to identify areas with high GW-SW interaction. Vertical head difference measurements indicated high variability in GW-SW exchange patterns along a specific stream reach, and simultaneous streambed pore water sampling along this reach identified high concentrations of soluble reactive phosphorous (SRP) that were indicative of GW-SW exchange. Furthermore, a single DC survey line was imaged along

the center of the stream to provide an initial understanding of streambed heterogeneity and help to optimize the design of the high-resolution 3D DC imaging that would subsequently be performed.

Figure 3-2 presents a plan view of the study stream reach. The reach is 50 m long with a very slight meander, transverse widths vary from 1.2 m to 3.8 m. The stream stage varied seasonally with maximum and minimum depths of 0.47 m to 0.1 m, respectively, and an average depth of 0.21 m. Surficial geology was noted from fine sands to loose gravelly-sand with larger cobbles present upstream. Agricultural farmland for crops is maintained on either side of the stream, with riparian zones comprising of tall grasses and trees are directly adjacent to the stream on both sides. Elevation changes of up to 2 m exist from riparian zone to stream banks.

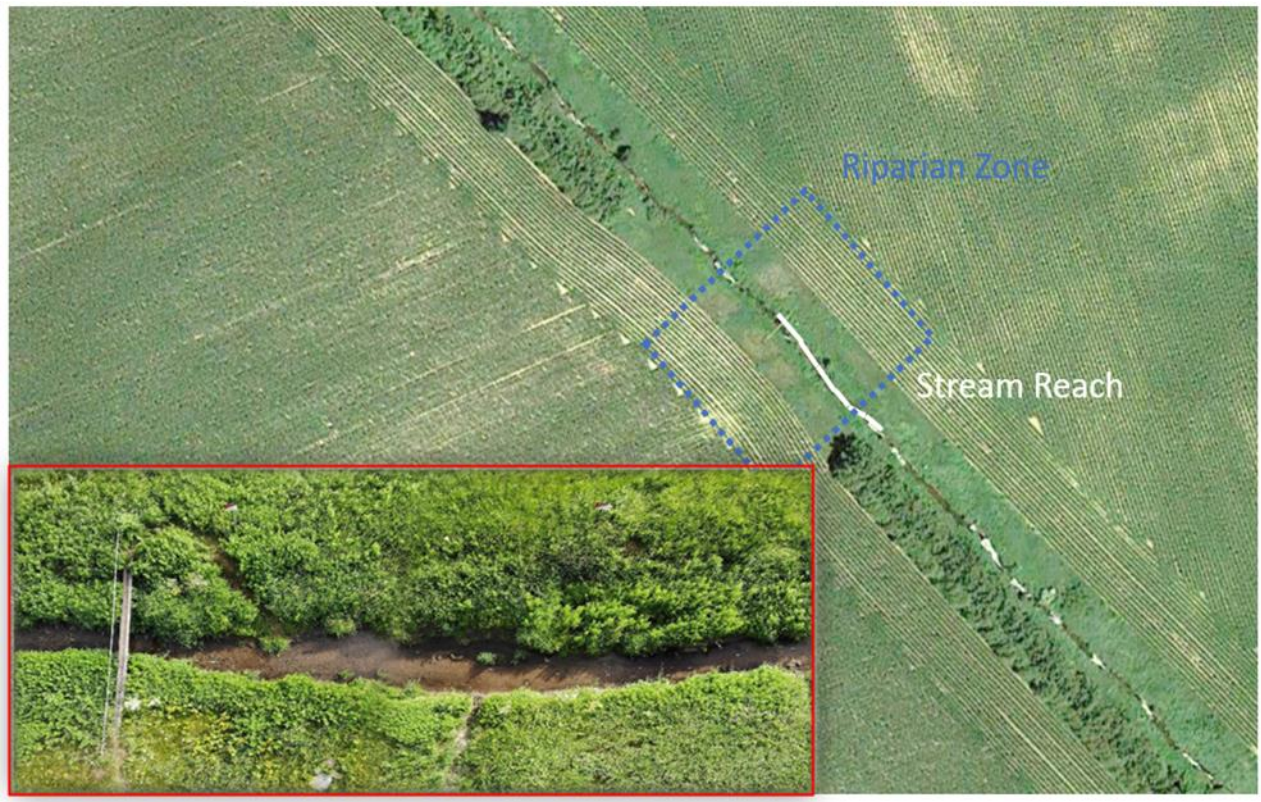

Figure 3-2: Aerial photographs of the stream reach and the bordering riparian zones. Stream border is from September 13th, 2019; it changed slightly through the monitoring period.

3.3 METHODOLOGY

A number of different field techniques were employed to measure the key parameters for this study: (i) geophysical surveys, (ii) spatial temperature mapping, (iii) potentio-manometer readings, (iv) stream stage measurements (v) soil coring and sieve analysis and (vi) vertical temperature profiling.

3.3.1 GEOPHYSICAL IMAGING

Stream Reach

A 3D underwater DC-IP survey was performed to determine the structural heterogeneity of the streambed. A surface grid was laid out in the stream reach, consisting of ten parallel lines, as shown in Figure 3-3. Each long survey line had an inline spacing of 0.2 m and contained a total of 240 electrodes with a length of 47.8 m. As a 48-electrode system was being used, each survey line was captured through nine smaller lines that progressed downstream using the roll-along method. A 50% overlap between each successive line was employed to ensure full image integrity (Loke, 2015). Each long survey line was then traversed across the stream width with an interline spacing of 0.2 m, with 10 parallel lines providing a width of 1.8 m. In total, 2400 electrodes were used to provide a 2D surface area of 86.04 m^2 (47.8 m x 1.8 m), and an approximate depth of investigation of 1.5 m. Preliminary modeling of the stream confirmed that a 'submerged electrode' survey provided improved resolving ability over a 'floating electrode' survey as it reduced current leakage direct to the stream channel (e.g., Crook et al., 2008). Each small stainless-steel electrode (2.5 cm long) was pushed into the streambed sediment and the head of water over each electrode was recorded. By assuming the stream stage was flat, the water head measurements over electrodes would incorporate topographical information into the survey.

Riparian Zone

A 3D DC resistivity survey was also performed to image the larger geological structure surrounding the stream. A 2D surface grid of 26 parallel survey lines was implemented to capture the edge of the field and riparian zone on both sides of the stream. The outline of the grid is shown in Figure 3-2. Each line comprised 48 electrodes with an inline spacing of 1 m and a length of 47 m that was centered on the stream. The interline spacing between parallel lines was 2 m to provide

a survey width of 50 m. A total station was used to obtain the elevation of all 1248 electrodes to incorporate topography into the data processing and inversion.

Twenty-six parallel lines were orientated perpendicular to the stream and designed to capture the edge of the field and riparian zone on both sides of the stream. Each 48-electrode line had an inline spacing of 1 m and a line length of 47 m, which was centered on the stream, as shown in Figure 3-3.

Geophysics Data Acquisition

A multi-channel Syscal Pro Switch 48 resistivity meter (IRIS Instruments, France) was used to record the apparent (DC) resistivity and apparent chargeability (IP) data. Both dipole-dipole and multi-gradient electrode arrays were used to acquire two sets of resistivity data to potentially improve interpretations. Chargeability data was only acquired with the dipole-dipole array. Dipole-dipole generally exhibits high lateral and vertical resolution, while multi-gradient has a higher signal-to-noise (S/N) ratio (Dahlin and Zhou, 2006), which may have been necessary for potential noise in the stream due to monitoring wells and/or tile drains from the adjacent fields. A time window of 0.5 s was used for resistivity measurements, while the time window for chargeability was 2 s. Strong ground coupling (<1 kΩ) was attained at all electrode locations, particularly in advance of IP measurements. Table 3-1 presents a summary of the geophysical surveys.

Geophysics Data Processing and Inversion

Pre-processing of all recorded resistivity and chargeability data was performed with BIN2IP (Nivorlis, 2017) which extended the DC resistivity data quality evaluation scheme of Kim et al. (2016) to handle both DC and time-domain IP data. The key filtering steps in this processing tool were as follows: (1) all data were filtered on the basis of their S/N ratio (i.e., measurements with low signal (high geometrical factor) and extreme apparent resistivity values were removed); (2) the mean of all measurement errors (using standard deviation of resistance) associated with every electrode was used to assess if any ‘bad’ electrodes existed (i.e., mispositioned or disconnected); (3) the shape of the decay curve associated with all 20 IP time windows was assessed for every measurement instead of simply using the intrinsic chargeability value. In addition to ignoring both the first two, and last five, time windows, measurements whose curve shape was erratic or did not decay monotonically to follow the assumed Cole-Cole model were rejected.

Table 3-1: Summary of geophysical survey lines conducted at the Kintore site

Location	# Lines	Elec. per Line	Electrode Spacing (m)		Area (m^2)	Array [a]	# Meas per Line
			Inline	Interline			
Stream	10	240	0.2	0.2	47.8 × 1.8	D-D	1194
						M-G	1395
						D-D (IP)	931
Riparian Zone	26	48	1	2	47 × 50	D-D	1194
						M-G	1395
						D-D (IP)	931

[a] D-D, M-G and D-D (IP) represent dipole-dipole, multi-gradient and dipole-dipole (for IP survey), respectively

The recorded data were inverted using the DC-IP inversion program DC_2DPro (Kim, 2016), which performs iterative least-squares smoothness-constrained inversion on the recorded datasets. The elevation at each electrode was applied to include topography in the inverted sections. The 3D datasets were inverted with DC_3DPro (Kim, 2016). All inversions were performed for a maximum of seven iterations and had low residual RMS errors. Both dipole-dipole and multi-gradient measurements generally exhibited good data quality and similar inversion model results. Only dipole-dipole data are shown in the results section, though multi-gradient data were used to assist with interpretation.

The measured time-domain chargeability is a measure of the magnitude of the IP effect, and is sensitive to both the bulk conduction (electrolytic) and surface polarization (structural) properties of a material. The chargeability M can be divided by the electrical resistivity ρ to obtain a normalized chargeability MN (i.e., $MN = M/\rho$). Normalized chargeability has been shown to be a valuable parameter in the interpretation of field-scale IP surveys as it can help to distinguish between IP effects due to lithology and IP effects due to pore-water salinity (e.g. Amaya et al., 2016; Slater & Lesmes, 2002). Since surface polarization processes at the mineral-fluid interface control normalized chargeability, it can be a useful parameter in detecting the presence of clayey materials.

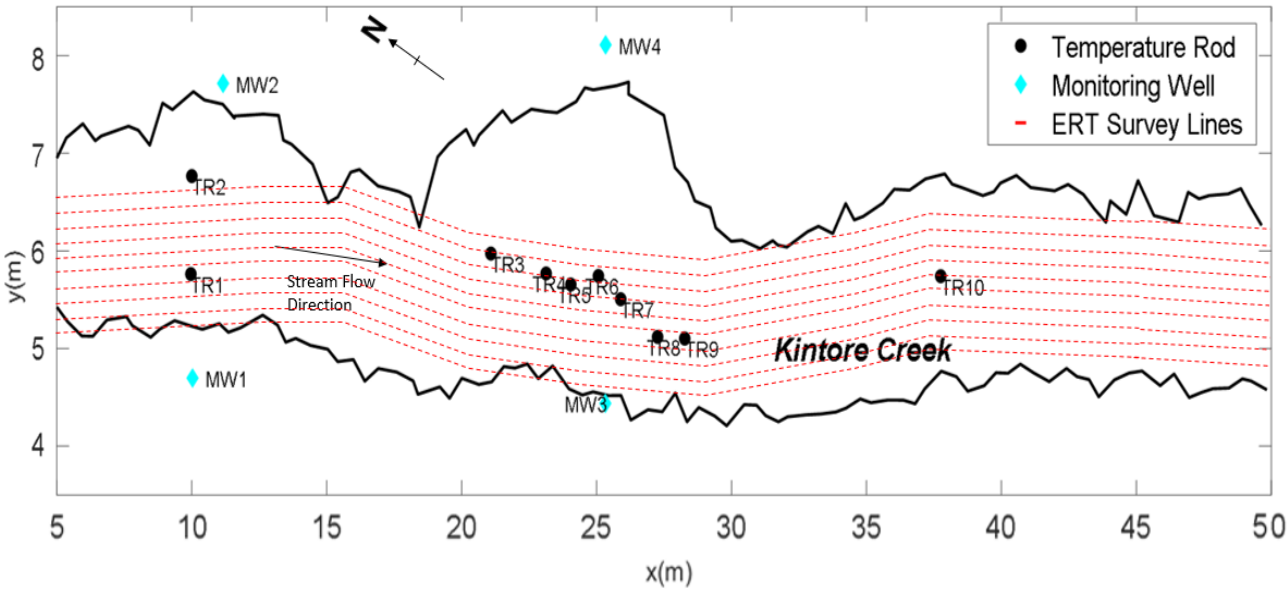

Figure 3-3: Digitized schematic of the stream reach indicating the outline of the stream and the locations of temperature rods (black circles), monitoring wells (blue diamonds), and the long 2D geophysical surveys lines of the Stream Reach Array.

3.3.2 SPATIAL STREAMBED TEMPERATURE MAPPING

Temperature mapping of the shallow streambed was conducted for qualitative evaluation of the GW-SW exchange patterns. Spatial temperature mapping was conducted on July 2, 2020 (summer event) and March 8, 2021 (winter event), with 339 and 358 measurements, respectively. These times were chosen to provide the highest temperature contrast between the streambed (potentially influenced by discharging groundwater) and surface water. In the summer, surface water temperatures will be higher than groundwater, whereas in the winter, surface water temperatures will be lower than groundwater. The temperatures at 0.1 m depths of the streambed were measured by temporarily inserting a high-accuracy thermometer (Hanna HI98509 Checktemp® 1 Digital Thermometer) into the sediment surface until the temperature stabilized. Measurements were recorded every 0.2 m along each line traversing the stream width, with a total of 36 parallel lines at 1 m offsets. Streambed measurements were recorded at each location while average surface water measurements were recorded for each transect, allowing the temperature difference between streambed and surface water to be determined.

Each mapping event was completed within a 3-hour period to limit the variation in the diurnal surface water temperature to provide an accurate characterization of temperature difference between surface and streambed temperatures. A spatial map showing the distribution of these temperature difference within the stream reach was then produced using kriging interpolation between data points.

3.3.3 VERTICAL HEAD DIFFERENCE AND HEAD WATER LEVELS

Vertical head difference within the shallow streambed were measured between the shallow groundwater and stream water with a potentiomanometer (e.g., Winter et al., 1988) attached to a drive-point piezometer (screen length = 10 cm). Positive gradients are representative of upwelling flow, while negative gradients represent downwelling flow. Each measurement was taken at a depth of 0.2 m below the streambed, with a total of 26 measurements taken at regular intervals along the stream reach.

Four fully-screened wells were installed along the banks of the stream reach to monitor water table elevations, as indicated in Figure 3-3. Temperature and pressure data were measured with Level 700 Data Loggers placed inside each well, with another logger attached to a vertical rebar and placed in the streambed, at the downstream end of the reach. A barometric logger was also employed on site to correct the well and stream pressure data for ambient air pressure, to derive water pressures and heights. Measurements were conducted every 15 minutes between December 6, 2019 and April 7, 2021. Temporal plots of GW-SW head elevations were produced for the duration of field investigations.

3.3.4 SOIL CORING AND SIEVE ANALYSIS

Soil cores were extracted from the stream reach to assess the lithological variation within the streambed and provide ground-truthing for the geophysical survey. A 5.7 cm diameter AMS Series Auger was used to extract cores to a depth of 0.6 m at each of the 10 locations where temperature rods were placed (within 15 cm of temperature rod). The cores were later separated based on distinguishable variations in lithology and prepared for sieve analysis (e.g. Smits et al., 2010). Each sample was oven-dried for a minimum of 12 hours and then placed in a stack of sieves, from #4 (4.75 mm opening) to #200 (0.075 mm opening), and mechanically shaken for 15 minutes. Each sieve was then weighed to measure the percent passing and a grain size distribution was

generated. From these distributions, the uniformity coefficient (C_u), mean grain size (D_{50}) and the percentages of gravel, sand, and fines (silt and clay) were determined.

3.3.5 VERTICAL TEMPERATURE PROFILING

3.3.5.1 INSTRUMENTATION AND DATA ACQUISITION

Vertical temperature profiles through the streambed were measured using a series of temperature rods (TR). Ten hollow steel TR with pointed tips were used with iButton temp loggers inside. Cardenas (2010), showed that the temperature profiles determined within steel rods are not sensitive to damping compared to outside sediment temperature. Each TR was 1.75 m long and contained a cross-linked polyethylene tubing of 0.65 m length and 0.02 m diameter that holds five iButton temperature loggers (DS1921H/DS1921Z High-Resolution Thermochron) with a resolution = 0.125 °C. The top iButton was placed at the streambed-surface water interface to measure the upper boundary temperature, while the rest of the iButtons were spaced vertically below that at depths of 0.05 m, 0.01 m, 0.2 m, 0.6 m. The higher resolution spacing near the surface was used to capture the variability in shallow temperature attenuation. Temperature measurements were logged every 30 mins between December 6, 2019 and May 20, 2021 and were manually downloaded each month. The 3D geophysical images were used to determine the locations for ten hollow steel temperature rods (TR1 – TR10) along the stream (see Figure 3-3), ensuring that the TRs were distributed between areas of the streambed with differing composition, likely leading to different water fluxes. Long-term vertical temperature profiling was performed within the stream reach and incorporated into a temperature-based analytical model to estimate the direction and magnitude of GW-SW exchange fluxes.

3.3.5.2 DATA ANALYSIS

Data Processing

The temperature offset between the different iButtons was determined by immersing all sensors in a plastic bag in a water bath with near-constant temperature. The sensors were kept in the water bath for 12 hours and logged at 5 min intervals. Differences between the individual sensors and the lowest standard deviated sensor were determined to generate appropriate calibration offsets which were applied to the raw data to provide comparative temperatures. Calibrations were completed on three separate occasions (June 17th 2019, May 16th 2020, April 18th 2021), to correct for any instrumental drift.

The temperature analysis software used assumes a steady-state vertical temperature profile. Thus, to provide appropriate data, rolling average of calibrated iButtons were analyzed. Low variation time periods of two to five days were isolated to create average temperature-depth profiles during each sampling period. To ensure consistency, two steady-state time periods were selected for each month of data, unless otherwise specified.

Temperature Flux Modeling

A number of temperature-based analytical models have been developed to assess GW-SW exchange fluxes, including 2DTempPro and VFlux (Irvine et al., 2020; Stonestrom & Constantz, 2003). In this study, the Flux in Layered Media (Flux-LM) automated spreadsheet tool (Kurylyk et al., 2017) was employed. Flux-LM uses temperature depth profiles to solve the following 1D subsurface heat transport equation by Bredehoeft and Papadopulos (1965):

$$\lambda_0 \frac{\partial^2 T}{\partial z^2} - qC_w \frac{\partial T}{\partial z} = 0, \quad (3.1)$$

where λ_0 is the bulk thermal conductivity of the saturated sediment [W m^{-1} °C^{-1}], T is the temperature [°C], z is the sediment depth [m], q is the vertical flux (positive downwards) [m/s], and C_w is the volumetric heat capacity of the water [J/m^3 °C].

Equation 3.1 has been extended to allow for variations in thermal conductivity of layers with depth (Kurylyk et al., 2017). In addition to the temperatures logged along the depth profiles of each TR,

other model inputs to FLUX-LM include the number, thickness, and thermal properties of the model layers.

Three different interpretations of streambed geology and associated thermal properties were modeled: (i) geology along the depth of each TR is fully homogenous and the thermal properties were based on the surficial streambed layer, (ii) geological variation is based on depth profiles of resistivity and chargeability at each TR, and (iii) geology is based on soil core analysis. The input parameters for each model were assigned based on their respective geological interpretation and associated thermal conductivities. A detailed review of the literature on the thermal properties of soils was used to understand and assign thermal conductivity values to different soil types, uniformities and levels of compaction (Tarnawski et al., 2011), with a summary presented in Table 3-2. Thermal conductivity is lower in soils with lower levels of compaction, such as near-surface streambed sediments, while it is higher for well-graded soils that typically exhibit higher porosity. The three models with differing input parameters were then simulated to determine the optimal Darcy flux (m/s) and the root mean square error (RMSE) (°C) for all depth profiles.

Table 3-2: Values of thermal conductivities applied to the different soil types and level of compaction for this study. [1] Tarnawski, 2011. [2] Moradifam, 2012

Compaction/Grading	Sediment Type	Estimated porosity	Thermal Conductivity (W m^{-1} $°C^{-1}$)
Packed/Graded	Fine Sand	0.4	2.75[1]
	Medium Sand	0.34	3.34[1]
	Coarse Sand	0.31	3.72[1]
	Gravely Sand	0.25	4.44[1]
Loose/Uniform	Fine Sand	0.43	2.52[2]
	Medium Sand	0.37	3.04[2]
	Coarse Sand	0.33	3.45[2]
	Gravely Sand	0.28	4.05[2]

3.4 RESULTS AND DISCUSSION

3.4.1 GEOPHYSICAL IMAGING

Two-dimensional cross-sectional slices were extracted from the 3D inverted domains of resistivity and chargeability to make the initial interpretation of the geophysical images easier. Figures 3-4a and 3-4b presents cross-sectional slices at 0.4 m (Line 3) and 1.2 m (Line 7) of inverted resistivity within the stream, respectively. The location and depth of the 10 soil cores (and TRs) that are adjacent to each line are indicated by grey boxes, while the black dashed line indicates the surface of the streambed. Both images infer three contrasting zones: (i) upstream zone with high resistivity, (ii) middle zone with low-to-moderate resistivity, and (iii) downstream zone with moderate resistivity on the west side of the stream and high resistivity on the east side.

The top layer of low resistivity (~20 ohm-m) represents the stream water and correlates to the measured stream water resistivity of 17 ohm-m. The upstream zone is located between 0 m and 12 m and indicates a very high resistivity (>400 ohm-m) layer to a depth of 0.8 m, which is representative of highly permeable sands and gravelly sands, that is underlain by a variation of very low resistivity (<40 ohm-m) and high resistivity (>400 ohm-m), which is indicative of fine, possibly clayey, material interspersed with more gravelly-sand material. The middle zone between 12 m and 36 m exhibits high variability in resistivity across the full depth of investigation, with areas of resistivity as low as 60 ohm-m (e.g., 18 m), and as high as 400 ohm-m (e.g., 23 m). This zone is indicative of highly heterogeneous soils with variations in permeability. The downstream zone between 36 m and 47.8 m shows a variation in resistivity across the stream width, with the west side of the stream exhibiting low-to-moderate resistivity (see Line 3) and the east side containing a layer of very high resistivity underlain by a layer of low resistivity (see Line 7).

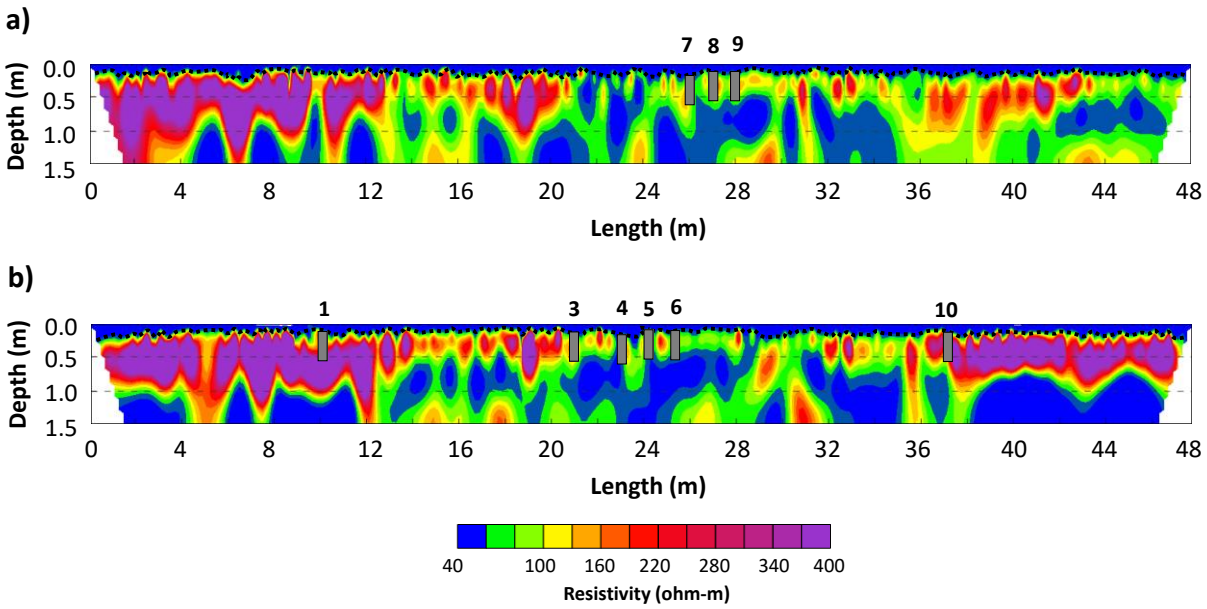

Figure 3-4: Inverted DC resistivity images of (a) Line 3, and (b) Line 7 of the Streambed Reach Array. The location of the various temperature rods that are adjacent to each line are also shown (grey boxes). The surface of the streambed is shown by the dashed black line; 0 m position is upstream. Note that a vertical exaggeration of 3x is used.

The inverted chargeability images (not shown) demonstrate that zones of highest chargeability (>20 mV/V) generally correspond to the zones of low resistivity shown in Figure 3-4. As discussed in Section 3.3.1, it is difficult to distinguish between the polarization effects due to pore-water salinity and lithology, and normalized chargeability is a better parameter for delineating the IP response from mineralogy only. Figure 3-5 presents the normalized chargeability images for the same cross-sectional slices at Lines 3 and 7. All zones of high normalized chargeability (>0.8 mS/m) are located at depths below 0.8 m, and generally correspond to those locations of very low resistivity in Figure 3-4. For example, the very low resistivity between 36 m and 46 m in Line 7 strongly correlates to high normalized chargeability. Conversely, the very high resistivity between 0 m and 12 m in Line 3 corresponds to negligible chargeability.

The normalized chargeability images strongly complement the resistivity images. Low chargeability zones infer non-clayey material, and as a result, zero surface conductivity. This means that resistivity is only influenced by pore-water salinity, saturation, and porosity. As the

streambed is fully saturated and has uniform low salinity, resistivity in non-chargeable zones is mainly influenced by porosity. Therefore, from Figures 3-4 and 3-5, material in low chargeability zones, which includes material within the top 0.6 m of the streambed, consists of sands and gravels. The uniformity of these sands and gravels is also a factor as it can control the porosity (e.g., higher uniformity equals higher porosity).

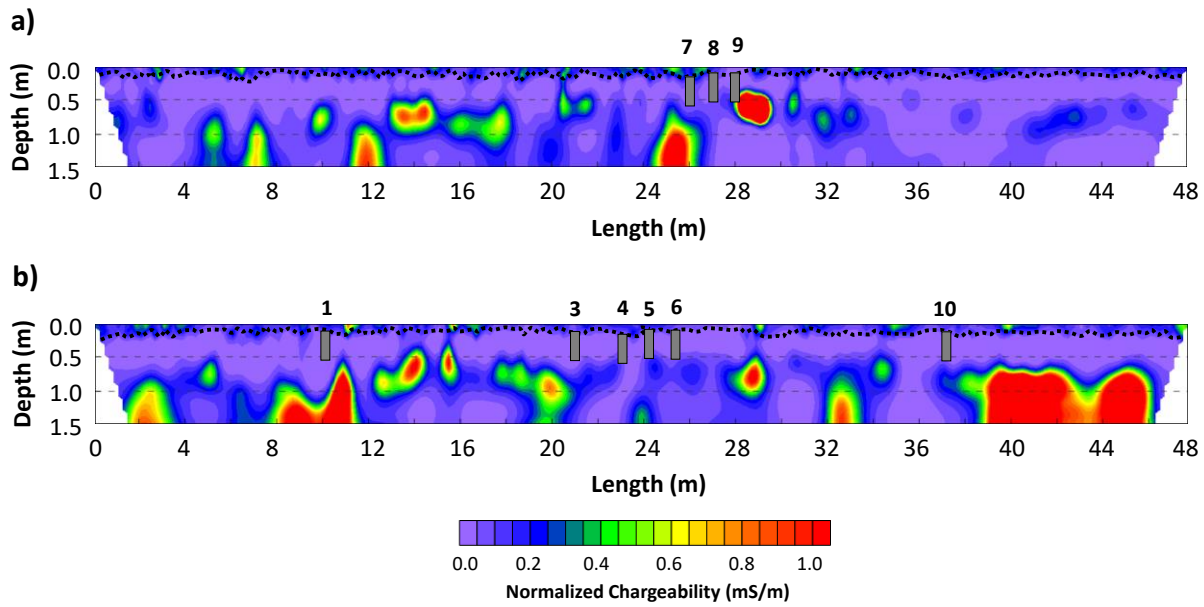

Figure 3-5: Normalized chargeability images of (a) Line 3, and (b) Line 7. The location of the various temperature rods that are adjacent to each line are also shown. The surface of the streambed is shown by the dashed black line. Note that a vertical exaggeration of 3x is used.

Figure 3-6a presents the 3D domain for inverted resistivity. A horizontal depth slice is presented at approximately 0.2 m below stream water elevations to coincide with the surface of the streambed. While this depth indicates high variability in resistivity, three zones of similar resistivity can be observed. Between 0 m and 12 m, higher resistivity exists. Lower resistivity occurs between 12 m and 36 m, with the lowest zones between 24 m and 32 m. Higher resistivity again exists downstream between 36 and 48 m, with notably higher measurements located on the east side of the stream.

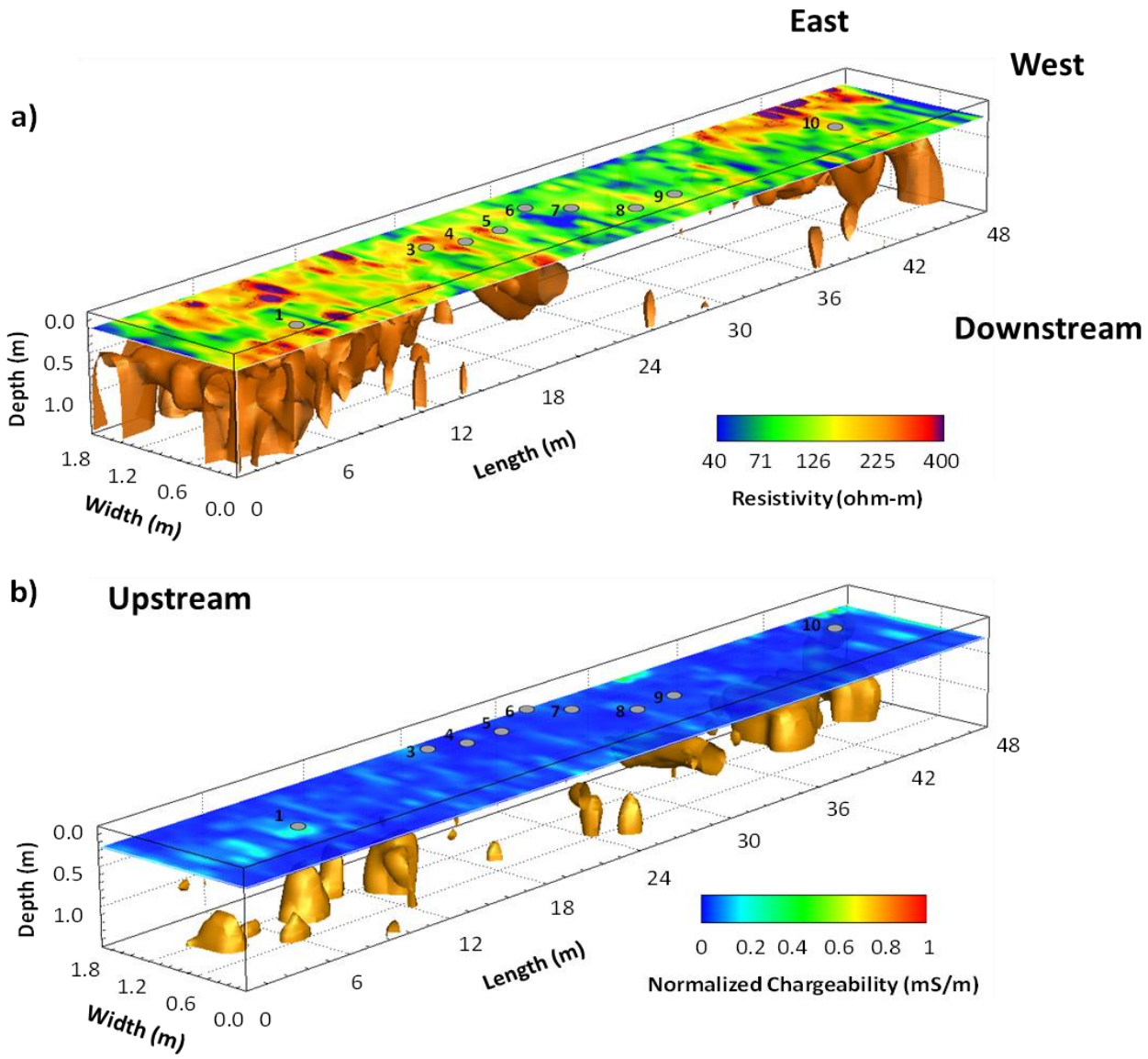

Figure 3-6: 3D inverted images of (a) resistivity, and (b) normalized chargeability. In each image, a slice of the streambed surface is shown (approximately to 0.2 m depth from top of water surface). 3D iso-volumes of resistivity (≥ 250 ohm-m) and normalized chargeability (≥ 0.6 mS/m) are also shown. Note that a vertical exaggeration of 3x is used.

Figure 3-7 presents a depth profile of resistivity and normalized chargeability at each TR, which can be used to infer characteristics of the soil at each location. As the normalized chargeability is generally negligible along the depth of all TRs, it is assumed that all soils within the top 0.6 m of the streambed are sands and gravels (i.e., zero clay). This is representative of a high porosity soil

with minimal clay content, which due to its depth, can be inferred as poorly compacted granular material. In the near surface of the streambed, the resistivity at all TRs is relatively low (< 80 ohm-m). Below this near-surface sediment, the resistivity is much higher at TR1 and TR10, which corresponds to the larger upstream and downstream zones. In contrast, the resistivity between TR3 and TR9 are much lower.

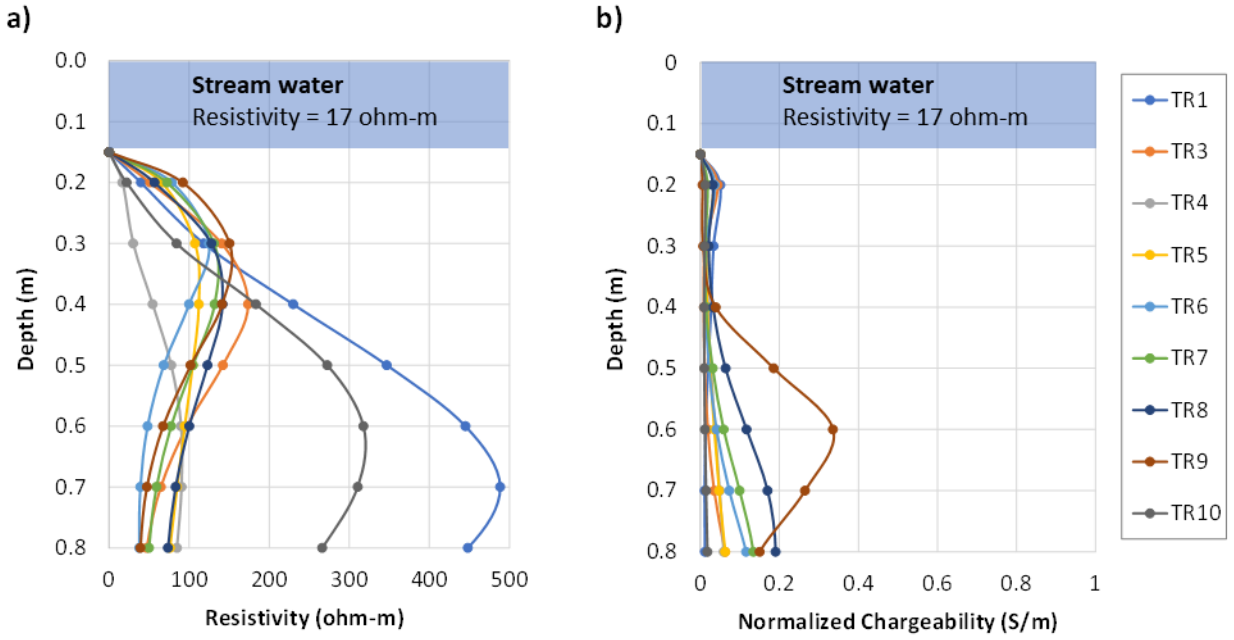

Figure 3-7: (a) inverted resistivity, and (b) normalized chargeability profiles along the depth (0 being top of the stream water) of each temperature rod location.

While the geophysical data collected across the riparian zone was fully inverted in 3D, a fence display of selected slices is beneficial to assist interpretation. Figure 3-8 presents a fence diagram of cross-sectional slices from Lines 20, 35 and 50 from the 3D riparian zone domain, along with Line 3 from the 3D streambed domain. It is evident that the resistivity and normalized chargeability distributions are coherent between all lines, with good lateral and vertical continuity evident at each intersection (e.g., low resistivity and low chargeability body at the intersection between Line 35 and Line 3).

The riparian zone, which lies between 20 m and 40 m, is highly heterogeneous with highest variability in resistivity and chargeability surrounding the stream. This is expected due to the irregular depositions occurring around streams and these geophysical variations have observed at

other stream studies (e.g., Busato et al., 2019; Dara et al., 2019). It is noted that at the upstream location of the stream, where Line 3 intersects with Line 20, high resistivity and negligible chargeability is evident on both sides of the stream, which correlates to the resistivity and chargeability shown in the streambed. Similarly, for the middle zone of the stream (Line 3 intersects with Line 35), the low resistivity zone within the streambed extends to both sides of the stream.

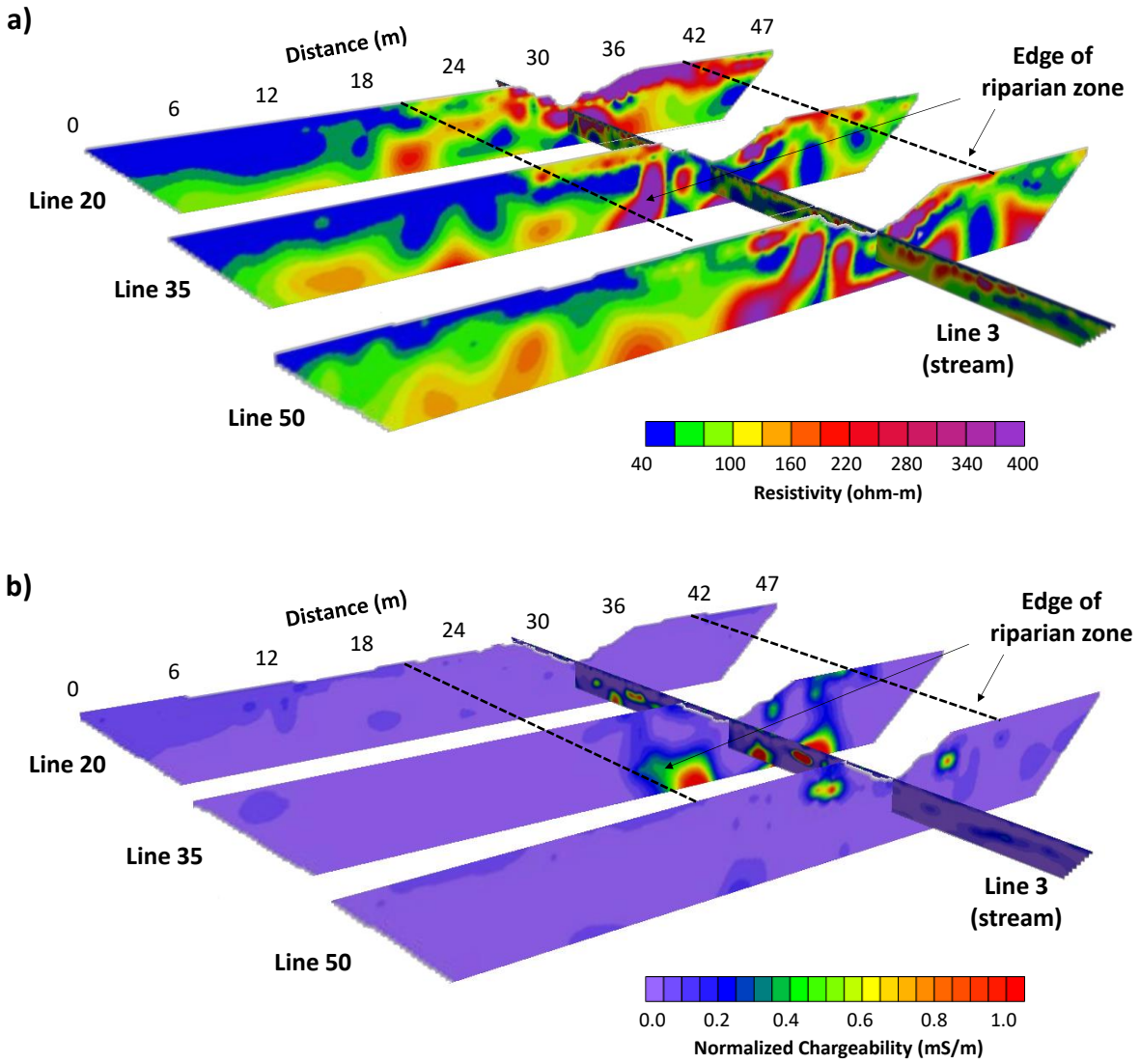

Figure 3-8: Fence diagram of (a) resistivity, and (b) normalized chargeability images of Lines 20, 35 and 50 from the riparian survey (Line 20 is furthest upstream), and Line 3 from the streambed survey. The black dashed lines indicate the edge of the riparian zone (boundary with agricultural field) on both sides of the stream.

While the focus of this study is on the streambed, the survey of the riparian zone provides additional information on the general geological structure surrounding the stream, confirming that: (i) upstream zone is characterized by high resistivity and high permeability material, which infers that this zone will provide the largest exchanges between GW and SW, (ii) the middle zone exhibits low resistivity and low permeability material that can limit GW-SW exchanges, and (iii) the downstream zone tends to have low resistivity and low permeability on the west side of the stream (Line 3 at 0.4 m), with high resistivity and high permeability on the east side (Line 7 at 1.2 m).

3.4.2 SPATIAL STREAMBED TEMPERATURE MAPPING

Figures 3-9a and 3-9b presents spatial maps of the temperature difference measured between streambed water (10 cm depth) and surface water in the summer and winter, respectively. In the summer, the stream water was warmer than groundwater and temperature difference varied spatially between 0.8 °C and 7.3 °C. A larger gradient (blue in Fig. 3.10a) indicates a larger difference between groundwater and stream water temperatures, and more significant upwelling of colder groundwater to the streambed. In the winter, with stream water colder than groundwater, temperature difference varied between -5.4 °C to 1.9 °C. In this case, larger negative gradients (blue in Fig. 3.10b) indicate more significant upwelling of relatively warmer groundwater to the streambed. Additional temperature maps were conducted in July 2019 and March 2020, results of which can be found in Appendix A.

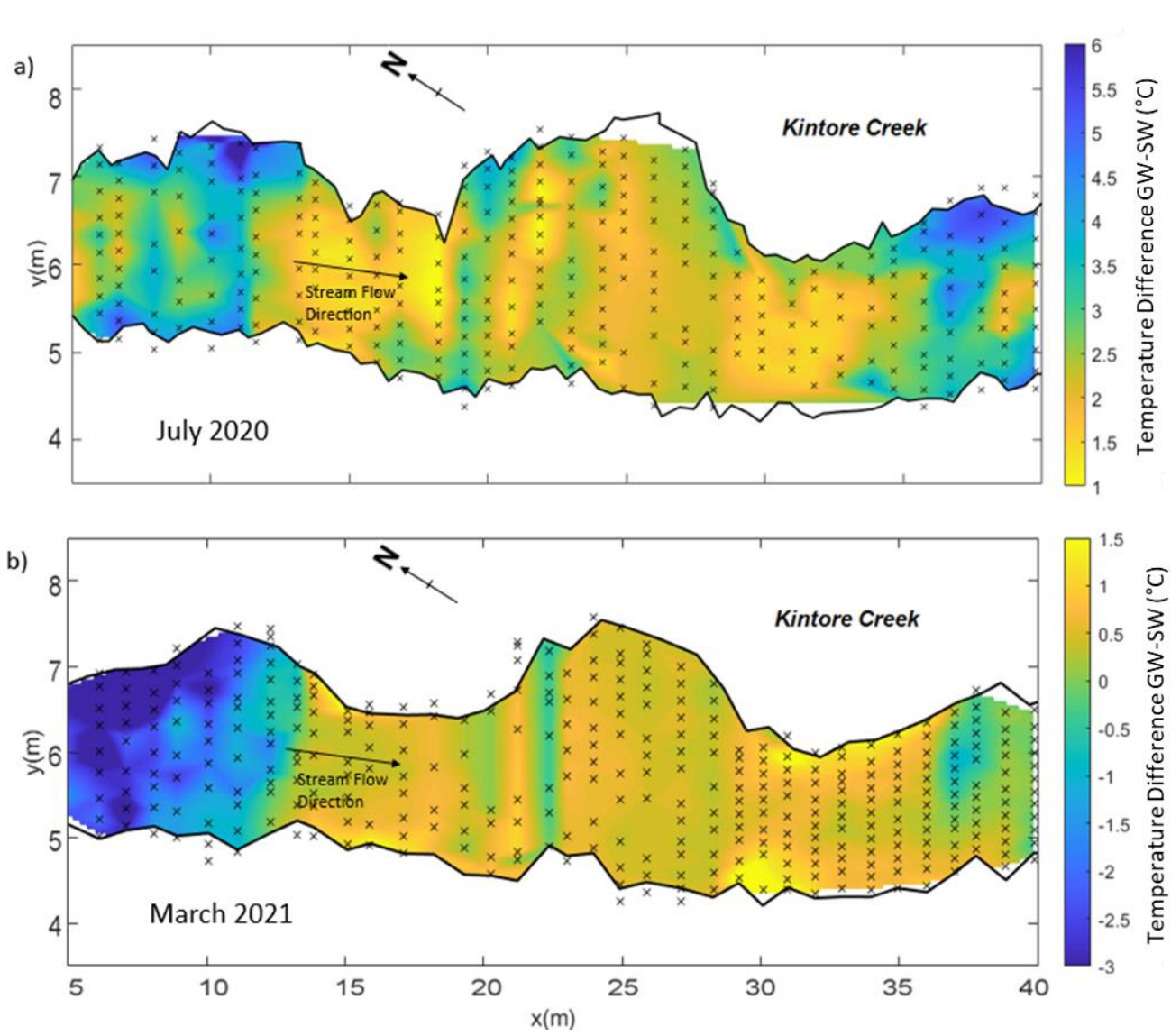

Figure 3-9: Spatial maps of temperature difference between groundwater and surface water during (a) summer baseflow conditions, and (b) winter baseflow conditions (note the different colour scales). The location of each temperature measurement is indicated by a black 'x'. Stream outline based on summer (low-flow) conditions; the stream width extended beyond this in places during the winter assessment.

It is evident from Figure 3-9 that the spatial maps show strong concordance with one another, with notable similarities in the patterns of temperature differences. This suggests continuity in the GW-SW exchange patterns for base flow, regardless of season.

Assessment of the stream reach temperature mapping indicates the existence of three zones. A distinct area of groundwater upwelling (>4 °C gradient in summer; <-1.5 °C gradient in winter) was observed from 5 m to 12 m along the length of the stream and extending its full width. Another area of groundwater upwelling (>4 °C in summer; -1 °C < gradient < 0 °C in winter) was observed from 36 m to 40 m, seemingly stronger on the east side. These upstream and downstream zones of groundwater upwelling were separated by a zone of lower gradients (< 2.5 °C in summer; > 0 °C in winter) between 13 m and 35 m. Within this middle zone lies two large areas at 15 m and 30 m with gradients of ~ 1 °C in both summer and winter, thereby indicating little exchange or higher recharge. Also within this zone were some small areas of groundwater influx between 17 m and 25 m, but significantly smaller in area and magnitude than the upstream and downstream zones. These observed spatial patterns of little to no flux could reflect hyporheic associated upwelling or GW discharge.

Comparisons of Figures 3-4, 3-5 and 3-6 to Figure 3-9 demonstrates the strong relation between streambed temperature difference and streambed composition inferred by geophysical imaging. For example, the highest temperature difference occur between 0 m and 12 m, which corresponds with the consistently high resistivity shown in this area (Figures 3-4 to 3-6). In the middle section of the stream, the temperature difference are generally much lower and more variable, which again corresponds to the low-to-moderate resistivity. In the downstream section, the geophysical images inferred low resistivity on the west side of the stream and high resistivity on the east side of the stream, which again supports the GW-SW exchange conditions which produced the temperature difference patterns.

3.4.3 VERTICAL HEAD DIFFERENCE AND HEAD WATER LEVELS

Figure 3-10 presents the location and magnitude of Vertical Head Differences (VHDs) between groundwater and surface water measured within the streambed sediments. Positive magnitudes (blue) indicate that the exchange flux moves from groundwater to surface water (GW > SW), while negative magnitudes (yellow) indicate that the exchange flux moves from surface water to groundwater (GW < SW). Large positive VHDs were measured at 10 m, 11 m and 37 m along the stream reach. In the middle zone, large negative VHDs were located at 21 m and 23 m, with all other locations alternating between low positive and low negative gradients. This interpretation

again provides confirmation of the suspected geologic conditions inferred by the geophysical surveys.

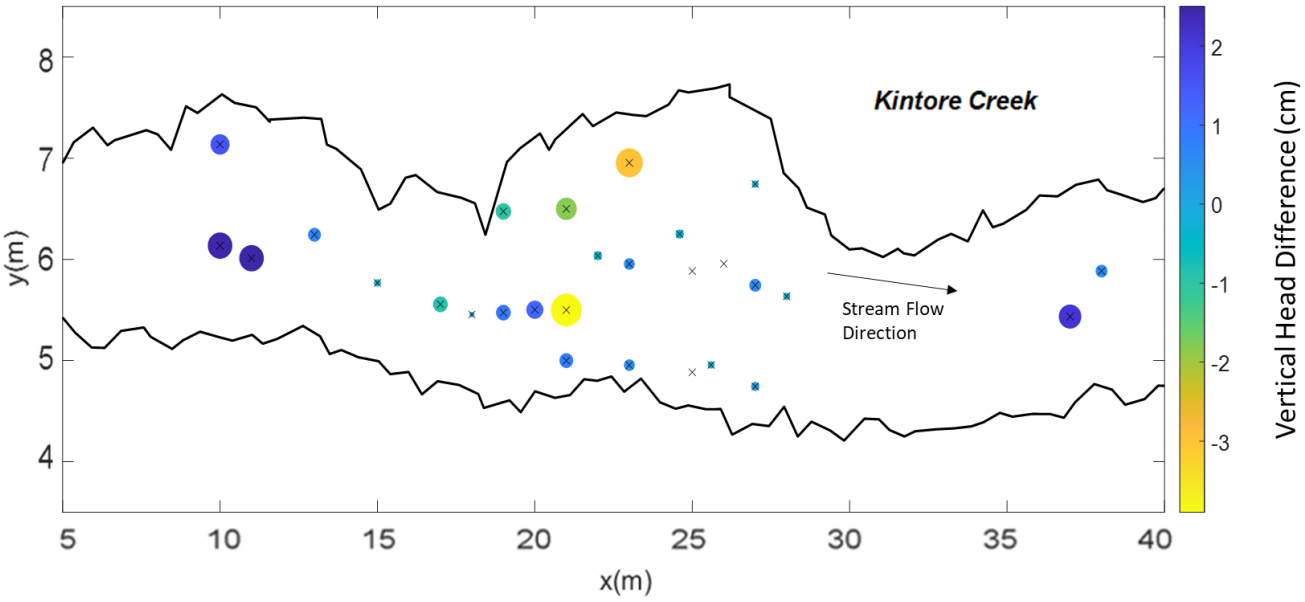

Figure 3-10: Vertical head difference measurements between groundwater and surface water. Positive values indicate the exchange flux direction is from groundwater to surface water. Magnitude of gradients are displayed by the corresponding symbol sizes and colour.

Figure 3-11 presents the temporal evolution of groundwater and surface water elevations in both the upstream and middle zones. When groundwater head is higher than the stream water, this suggests a drive for flow toward the stream, while when surface water head is higher than nearby groundwater suggests stream discharge.

Several anomalies exist throughout the time period which are associated with heavy rainfall, snowmelt and overland flow events; however, distinguishable overall trends are evident. In the upstream comparison groundwater levels are consistently higher between January 2020 and June 2020, producing positive head differences that indicate the potential for ‘gaining’ conditions in the stream. Between July 2020 and November 2020, the stream stage is higher than groundwater levels to indicate the potential for ‘losing’ conditions in the stream.

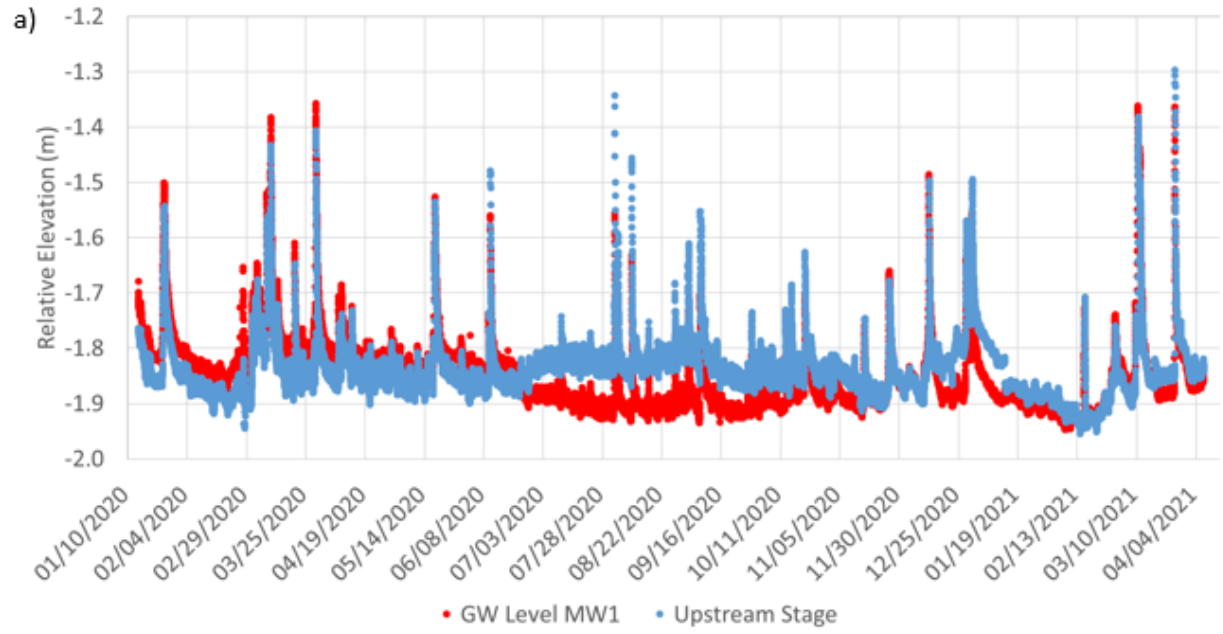

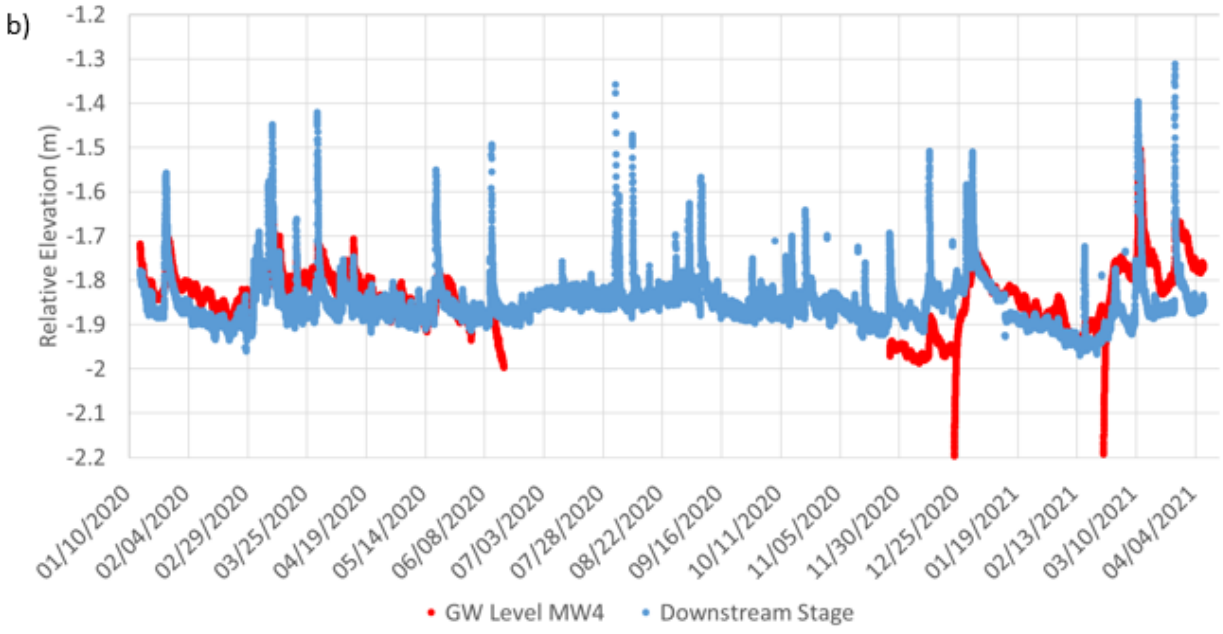

Figure 3-11: Temporal evolution of the head difference between groundwater and surface water at (a) 5 m (upstream zone), and (b) 30 m (middle zone) along the stream reach.

The downstream comparison of head levels follow similar seasonal trends as the upstream (shown from January 2020 to April 2020), with slightly lower groundwater levels. However, it is noted that groundwater took significantly longer in this downstream area to recharge following water

sample collection (for chemical analysis), as evident on December 23, 2020 and February 24, 2021. For this reason, groundwater data was removed between June 15, 2020 and November 25, 2020 as consistent sampling was conducted during this period.

3.4.4 SOIL CORING AND SIEVE ANALYSIS

Table 3-3 presents a summary of the soil characteristics at each of the 10 soil cores, indicating the uniformity coefficient, mean grain size and soil type. All locations consisted of soils ranging from fine sand to sandy gravel, with a maximum of 7% fines. This information will be used to assign thermal properties to 'Model 3' of the temperature flux modeling. This characterization was related well to the DC resistivity and chargeability images. For example, the chargeability images indicated very little clayey material within the top 0.6 m of the streambed, which was then confirmed by the soil analysis.

Table 3-3: Classification of the soil samples extracted at the 10 TR locations within the stream

TR	Depth Intervals (m)	Cu	D50	Soil Type	TR	Depth Intervals (m)	Cu	D50	Soil Type
1	0-0.15	12.5	3	gravelly sand	6	0-0.15	3.2	0.49	fine sand
	0.15-0.3	11.05	3.8	coarse sand		0.15-0.3	4.25	0.57	fine sand
	0.30-0.45	13.19	2.83	coarse sand		0.3-0.4	7.14	0.81	medium sand
						0.4-0.5	22.5	1.3	medium sand
2	0-0.15	12	1.35	medium sand	7	0-0.14	11.05	4.75	coarse sand
	0.15-0.3	11.4	1.4	medium sand		0.14-0.32	24.17	1.15	medium sand
	0.3-0.45	12.35	2.65	coarse sand		0.32-0.5	27.37	1.15	medium sand
3	0-0.15	24.71	2.3	coarse sand	8	0-0.09	18.27	4.4	coarse sand
	0.15-0.3	20.67	1.6	medium sand		0.09-0.19	12.69	0.77	fine sand
	0.3-0.4	12.14	2.25	coarse sand		0.19-0.29	5.08	0.42	fine sand
	0.4-0.48	9.25	1.1	medium sand		0.29-0.47	38.95	0.96	medium sand
4	0-0.2	11.54	2.45	coarse sand	9	0-0.1	10.74	1.7	medium sand
	0.2-0.35	25.88	2.75	coarse sand		0.1-0.22	11.76	1	medium sand
	0.35-0.15	13.93	0.81	medium sand		0.22-0.3	12.39	1.8	medium sand
						0.3-0.46	14.17	0.71	fine sand
5	0-0.2	10.42	0.68	medium sand	10	0-0.1	9.13	0.81	gravelly sand
	0.2-0.3	36.54	4.75	coarse sand		0.1-0.3	5.38	0.75	fine sand
	0.3-0.45	47.5	2.8	coarse sand		0.3-0.45	15.32	2.75	coarse sand

3.4.5 VERTICAL TEMPERATURE PROFILING

Temperature-Depth Profiles

A wide range of measured temperatures exist due to the spatial variation of the measurement locations as well as seasonal effects. Profiles of temperature versus depth were generated for all 10 locations throughout the stream reach. Temperatures ranged from 1°C to 12°C during winter periods and from 10°C to 22°C during summer periods.

Two TRs, one within a high permeability zone and another within a low permeability zone, were selected to highlight qualitative interpretation of the raw temperature profiles. Temperature profiles can be used to obtain preliminary information about the stream reach prior to calculating the vertical fluxes with the Flux-LM model (Briggs et al., 2014). Figure 3-12 presents the raw temperature-depth profiles for a year of sampling data at TR1, which is located along the 10 m transect, and TR8, which is located along the 27 m transect. TR1 exhibits strong variations with increasing depth, while TR8 show relatively weak variations. The TR1 profile is relatively sharp in curvature within the top 0.1 m to 0.2 m of the streambed, with the sharpest curvatures occurring during winter time periods, and these curvatures (convex upward) are indicative of medium to high groundwater discharge. In contrast, TR8 shows very little curvature across all seasons, which indicates low groundwater discharge or recharge conditions. With increasing depth, temperatures converge to 10°C at TR1, suggesting allowable exchange of GW and SW. In contrast, there is no convergence in temperature by 0.6 m depth at TR8. During winter, temperatures were 5°C while in the summer, temperatures were approximately 17°C to 20°C, which suggests that TR8 is more affected by seasonal variation, as opposed to the exchange between GW and SW.

It was noted that TR2 exhibited similar variations to TR1 (strong), TR4 to TR9 exhibited similar variations to TR8 (weak) and TR3 and TR10 showed low-to-medium variations. Additional temperature-depth profiles can be found in Appendix A.

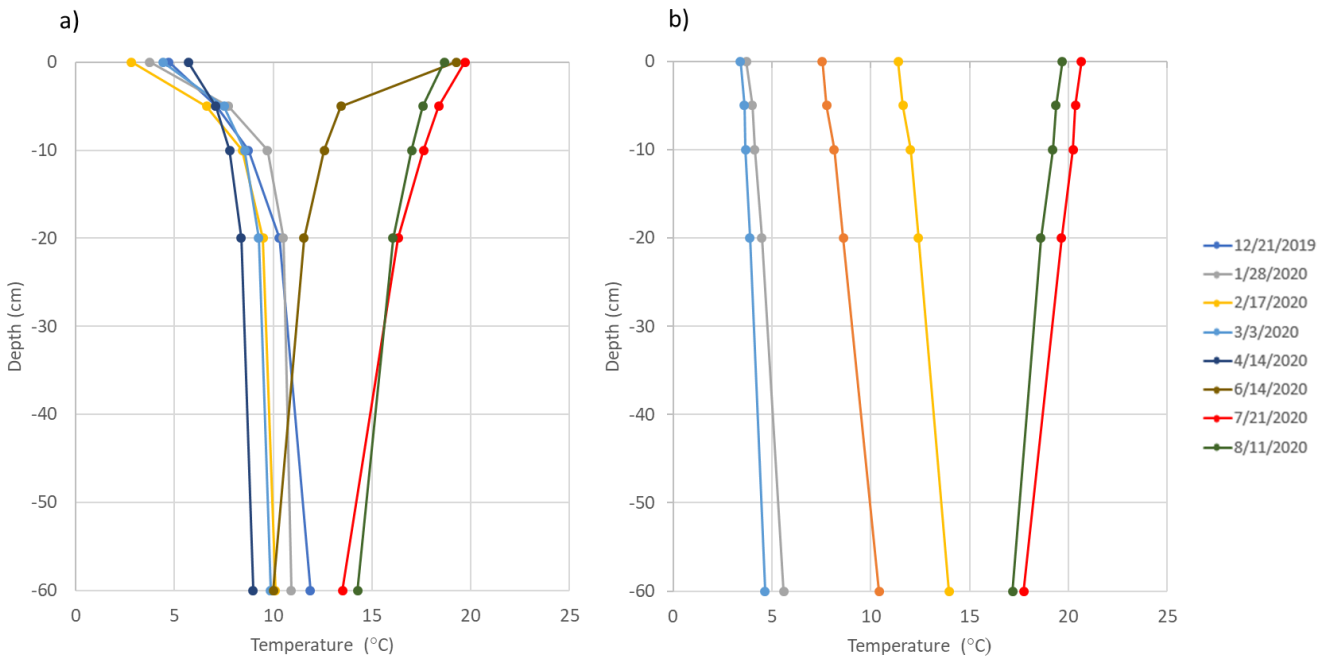

Figure 3-12 Temperature versus depth profiles at (a) TR1, and (b) TR8 over a year of collected data. Dates omitted are due to instrumental error.

FLUX-LM Modeling

The temperature-depth profiles for periods of near steady-state were used to calculate the vertical exchange fluxes at all TR locations. Fluxes were determined for the three different models of sediment compositions and thermal properties: (i) Model 1 was based on sediment surface observations only, (ii) Model 2 was based on surface observations plus geophysical imaging, and (iii) Model 3 was based on soil core characteristics. Table 3-4 present a summary of lithological interpretations and associated thermal properties for each of the three models. As shown, Model 1 assumes a homogeneous model domain that is represented by a single thermal conductivity, while Models 2 and 3 are able to better define the streambed composition and permit heterogeneous layered model domains.

Table 3-4: Lithological interpretation for all 10 TRs based on surficial observations (Model 1), geophysical imaging (Model 2), and soil core characteristics (Model 3)

TR	Interpretation 1			Interpretation 2			Interpretation 3		
	# Layers	Layer Thickness (cm)	Thermal Conductivity (W m-1 ℃-1)	# Layers	Layer Thickness	Thermal Conductivity (W m-1 ℃-1)	# Layers	Layer Thickness	Thermal Conductivity (W m-1 ℃-1)
1	1	0-0.6	4.05	2	0-0.2	4.05	2	0-0.1	4.05
					0.2-0.6	3.72		0.1-0.6	4.44
2	1	0-0.6	4.05	-	-	-	3	0-0.05	4.05
								0.05-0.3	3.04
								0.3-0.6	4.44
3	1	0-0.6	3.72	2	0-0.6	3.72	4	0-0.15	3.72
								0.15-0.3	3.34
								0.3-0.4	3.72
								0.4-0.6	3.04
4	1	0-0.6	4.05	2	0-0.2	4.05	3	0-0.05	4.05
					0.2-0.6	3.34		0.05-0.35	3.72
								0.35-0.6	3.34
5	1	0-0.6	3.04	2	0-0.1	3.04	2	0-0.2	3.04
					0.1-0.6	3.34		0.2-0.6	3.72
6	1	0-0.6	2.52	3	0-0.2	2.52	2	0-0.3	2.52
					0.2-0.4	3.72		0.3-0.6	3.34
					0.4-0.6	3.34			
7	1	0-0.6	3.45	3	0-0.1	3.45	2	0-0.14	3.45
					0.1-0.2	3.34		0.14-0.6	3.34
					0.2-0.6	3.72			
8	1	0-0.6	3.45	2	0-0.2	3.45	3	0-0.09	3.45
					0.2-0.6	3.72		0.09-0.29	2.75
								0.29-0.6	3.34
9	1	0-0.6	3.04	3	0-0.1	3.04	3	0-0.1	3.04
					0.1-0.5	3.72		0.1-0.3	3.34
					0.5-0.6	3.34		0.3-0.6	2.75
10	1	0-0.6	4.05	2	0-0.3	4.05	3	0-0.05	4.05
					0.3-0.6	3.72		0.05-0.3	2.75
								0.3-0.6	3.72

Two sampling periods, one during winter and one during summer, were selected to highlight the solution effects of the progressing models for differing temperature-depth profiles. Figure 3-13a compares the modeled temperatures to the observed temperatures in the field at TR1 during a winter period (December 23rd – 27th, 2019). As shown above, TR1 varies between a one-layer system (Model 1) and a two-layer system (Model 2 and 3). It is evident from qualitative interpretation, and the associated RMSE (°C) values, that each successive model improves the fit between modeled and observed temperatures. A similar progression of improved model fit occurs at TR8 during a summer period (July 23rd – July 27th, 2020), as shown in Figure 3-13b. It is noted that the distinguishable change in slope of the data for TR8 at the 10-cm depth was not captured well by any of the models, despite using multiple layers. This suggests that there is a stronger change in thermal properties than captured by geophysics or coring.

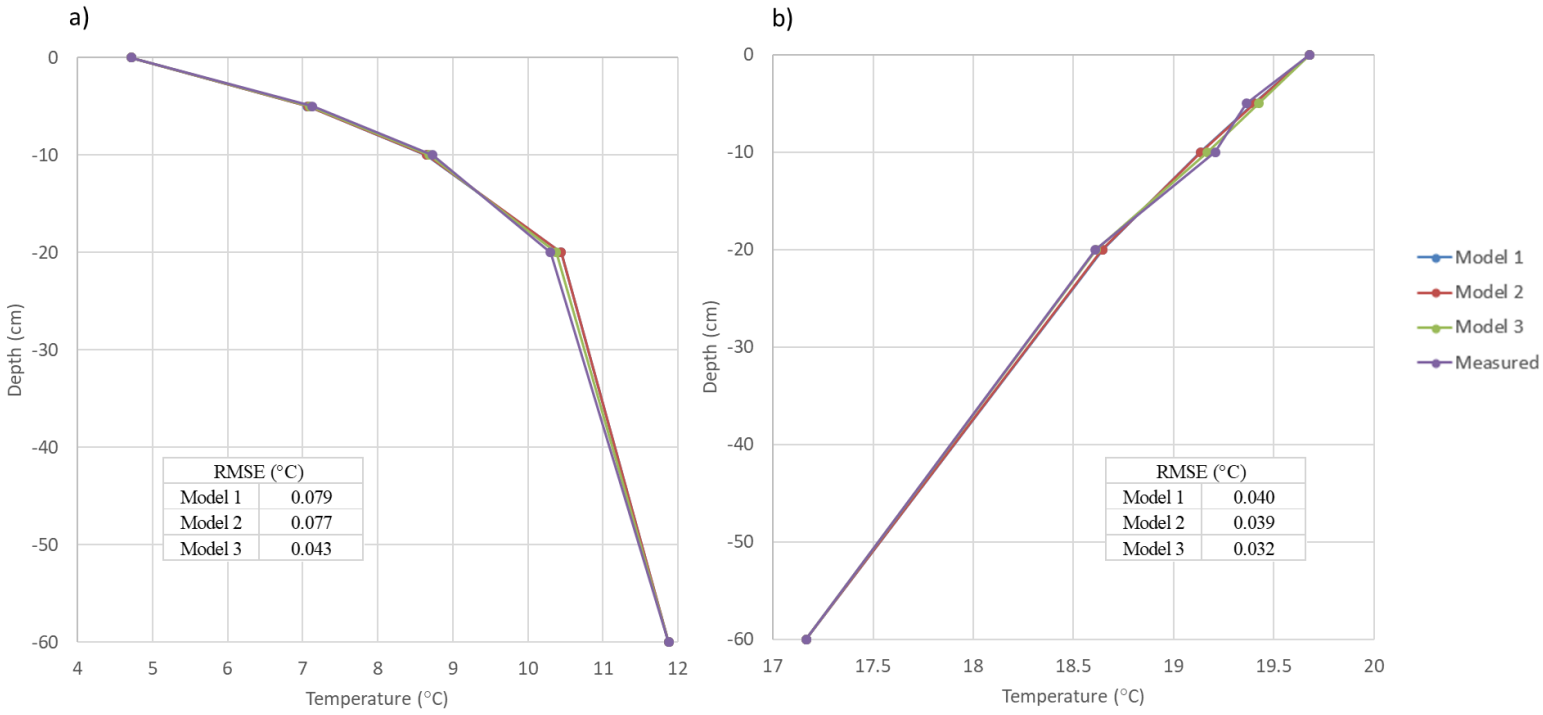

Figure 3-13: Comparison between observed temperatures and modeled temperatures produced by FLUX-LM for Models 1 to 3 at TR1 and TR8. The RMSE (°C) for each model is indicated in the boxes for TR1 and TR8.

It is evident that all three models provide a good fit between observed and modeled temperatures. This is due to the very small variation in thermal properties assigned here between the different soil types within the top 0.6 m of the streambed. As shown in Table 3-4, thermal conductivity only varies between 2.52 W m^{-1} $°C^{-1}$ (uniform fine sand) and 4.44 W m^{-1} $°C^{-1}$ (graded sandy gravel), resulting in only slight improvements between each successive model. This is further confirmed as the average RMSE (°C) for all temperature rods was between 0.04 °C and 0.22 °C. These results display confidence in the various interpretations as well as the Flux-LM calculated exchange fluxes. It is noted that TR1 and TR2 produced the most uncertainty while TR 4 and 7 were most consistent. This was expected as the temperature variations in the area of TR1 and TR2 were much higher due to the more permeable conditions.

The calculated temporal temperature flux over time at each TR location is presented in Figure 3-14. Positive fluxes indicate flux exchanges from SW to GW (i.e., groundwater recharge), while negative fluxes indicate exchanges from GW to SW (i.e., groundwater discharge). TR1 and TR2 demonstrated the highest flux magnitudes that are mostly negative, which was expected as they are located within the most permeable zones inferred by the geophysical images, further confirming exchange flux from GW to SW (i.e., groundwater discharge). For example, the fluxes at TR1 vary from -100 m/year during summer periods to -512 m/year during winter periods. The temperature fluxes at TR4 to TR9 exhibit much lower variability between summer and winter periods. For example, the fluxes at TR4 vary from -70 m/year to 42 m/year and at TR6 fluxes vary from -25 m/year to 30 m/year, between the summer and winter periods, respectively. The variance between positive and negative fluxes suggest some seasonal upwelling/downwelling trends. Finally, TR3 and TR10 show similar trends to TR 1 and 2, but with much smaller magnitudes as TR3 varied from -20 m/year to -95 m/year during the summer and winter periods. Additional exchange flux results and the associated RMSE values can be found in Appendix A.

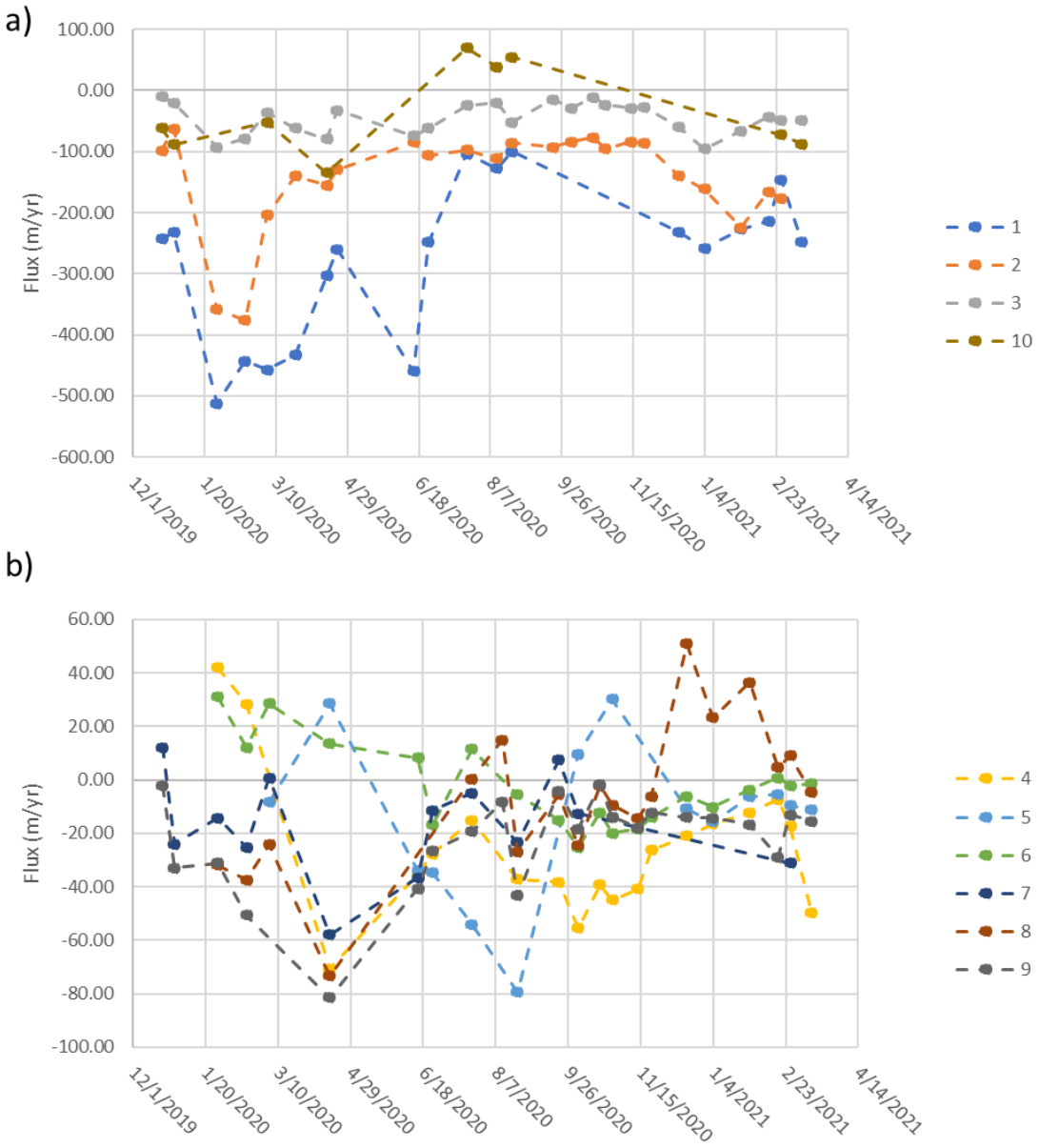

Figure 3-14: Temporal evolution of temperature exchange fluxes, calculated using the Model 3 interpretation, a) includes TR 1-3 and 10 and b) includes TR 4-9. Note the axis difference between a) and b).

It is understood that there is much variation (at least 2 times) in thermal conductivity for different materials and lack of data on compaction of the site sediments (not measured during coring), so uncertainty in the proper assignment of values may also contribute to the lack of difference in fits. Nevertheless, it is essential to always incorporate any additional information on the soil and thermal properties into the FLUX-LM model. Many other stream sites can contain a larger

variation in streambed composition, ranging from uniform clays to well-graded gravels, which would provide a greater range of thermal properties and ensure that stream heterogeneity is essential to obtain improved model fits.

It should also be acknowledged that while soil core characteristics (Model 3) can provide slightly improved model fits over geophysical imaging (Model 2) in this study, this is expected as direct physical information is obtained when soil cores are extracted at the exact location of the TRs. It is well-established that the benefit of geophysical imaging is the rapid, non-invasive continuous information it can provide between these sparsely distributed and invasive soil cores. In other studies, it may not be possible to collect soil cores at some locations. Furthermore, for 2D/3D temperature modeling, continuous spatial information is required, and geophysical imaging can easily provide this.

3.5 CONCLUSIONS

In this study, the potential of 3D DC-IP for investigating and characterizing streambed composition and structural heterogeneities, and consequently, providing additional information between groundwater and stream water interactions, was assessed. Traditionally, these investigations have relied on techniques such as streambed temperature mapping, seepage meters, modeling streambed temperature profiles, head gradient and soil coring, but these techniques can be invasive, costly and provide limited sampling density. These limitations are especially problematic in streambeds which can be highly heterogeneous and contain unconsolidated material that can easily lose integrity through invasive techniques. Geophysical techniques such as DC-IP exhibit significant potential for streambed investigations as they are non-invasive and provide rapid, continuous information on the subsurface. Despite this potential, DC-IP is yet to become commonly used at streams, due, in part, to a lack of information on its performance compared to more traditional techniques.

High-resolution 3D DC-IP surveys were conducted in a 50 m long headwater stream reach located in Kintore, Ontario. The resulting 3D distributions of resistivity and chargeability revealed the composition within the streambed. Resistivity images inferred three different zones within the stream reach: (i) upstream zone with high permeability and potential for high flux exchanges

between GW and SW, (ii) middle zone with lower permeability and reduced GW-SW flux exchanges, and (iii) downstream zone with high permeability on the eastern side of the stream.

Traditional characterization techniques were then employed to characterize the stream reach and assess GW-SW exchanges. GW-SW temperature differences measured within the top 0.1 m of the streambed were used to qualitatively identify areas of high and low GW-SW exchanges. Vertical head differences were measured between shallow groundwater and stream water to determine spatial upwelling/downwelling patterns. Soil coring and sieve analyses were performed to obtain direct empirical evidence of sediment characterization and to assist in improving model characterization. And vertical temperature profiles were used to evaluate the vertical exchange fluxes qualitatively and quantitatively between GW-SW throughout the stream reach.

The comparison between DC-IP imaging and all other traditional hydrogeological methods was continually assessed throughout the study. Resistivity images indicated variations throughout the streambed, stressing the sensitivity to spatial heterogeneity. These variations corresponded well with the results of the spatial streambed temperature maps, which indicated high resistivity related to high upwelling areas and low resistivity related to lower upwelling/downwelling areas. The connections between the inferred streambed composition from DC-IP imaging and spatial streambed temperature maps also corresponded well with the vertical head differences and the associated GW-SW exchange directions. Chargeability images indicated that all material within the top 0.6 m of the streambed contained negligible charge, inferring non-clayey soils such as sands and gravels, which was seen in the sieve analysis. And the connection between the qualitative and quantitative flux results and the associated sediment compositions, were determined as strong.

Overall, the concordance between DC-IP imaging and all the other traditional methods provides increased confidence in the ability of DC-IP to provide a valuable, non-invasive site tool to improve characterization of streambed heterogeneity and interpretation of GW-SW exchange patterns.

3.6 REFERENCES

Amaya, A. G., Dahlin, T., Barmen, G., & Rosberg, J. E. (2016). Electrical resistivity tomography and induced polarization for mapping the subsurface of alluvial fans: A case study in Punata (Bolivia). *Geosciences (Switzerland)*, *6*(4). https://doi.org/10.3390/geosciences6040051

Baker, D. B., Johnson, L. T., Confesor, R. B., Crumrine, J. P., Guo, T., & Manning, N. F. (2019). Needed: Early-term adjustments for Lake Erie phosphorus target loads to address western basin cyanobacterial blooms. *Journal of Great Lakes Research*, *45*(2), 203–211. https://doi.org/10.1016/j.jglr.2019.01.011

Binley, A., Hubbard, S. S., & Huisman, J. a. (2015). The emergence of hydrogeophysics for improved understanding of subsurface processes over multiple scales. *Water Resources Research*, 1–30. https://doi.org/10.1002/2015WR017016.Received

Briggs, M. A., Lautz, L. K., Buckley, S. F., & Lane, J. W. (2014). Practical limitations on the use of diurnal temperature signals to quantify groundwater upwelling. *Journal of Hydrology*, *519*(PB), 1739–1751. https://doi.org/10.1016/j.jhydrol.2014.09.030

Busato, L., Boaga, J., Perri, M. T., Majone, B., Bellin, A., & Cassiani, G. (2019). Hydrogeophysical characterization and monitoring of the hyporheic and riparian zones: The Vermigliana Creek case study. *Science of the Total Environment*, *648*, 1105–1120. https://doi.org/10.1016/j.scitotenv.2018.08.179

Buss SR, Cai Z, Cardenas MB, Fleckenstein JH, Hannah DM, Heppell K, H. P., Ibrahim T, Kaeser D, Krause S, Lawler DM, Lerner DN, Mant J, Malcolm IA, O. G., Parkin G, Pickup RJ, Pinay G, Porter J, Rhodes G, Richie A, Riley J, Robertson A, S. D., & Shields B, Smith JWS, Tellam JH, W. P. (2009). The Hyporheic Handbook A handbook on the groundwater – surface water interface and hyporheic zone for environment managers Integrated catchment science programme Science report : SC050070 The Environment Agency is the leading public body protecting and im. In *Hydrogeology Journal* (Vol. 11, Issue 3). https://assets.publishing.service.gov.uk/government/uploads/system/uploads/attachment_data/file/291621/scho1009brdx-e-e.pdf

Cardenas, M. B. (2010). Thermal skin effect of pipes in streambeds and its implications on groundwater flux estimation using diurnal temperature signals. *Water Resources Research*, *46*(3), 1–12. https://doi.org/10.1029/2009WR008528

Conant, B., Cherry, J. A., & Gillham, R. W. (2004). A PCE groundwater plume discharging to a river: Influence of the streambed and near-river zone on contaminant distributions. *Journal of Contaminant Hydrology*, *73*(1–4), 249–279. https://doi.org/10.1016/j.jconhyd.2004.04.001

Conant, B., Robinson, C. E., Hinton, M. J., & Russell, H. A. J. (2019). A framework for conceptualizing groundwater-surface water interactions and identifying potential impacts on water quality, water quantity, and ecosystems. *Journal of Hydrology*, *574*(January), 609–627. https://doi.org/10.1016/j.jhydrol.2019.04.050

Coscia, I., Greenhalgh, S. A., Linde, N., Doetsch, J., Marescot, L., GuNther, T., Vogt, T., & Green, A. G. (2011). 3D crosshole ERT for aquifer characterization and monitoring of infiltrating river water. *Geophysics*, *76*(2). https://doi.org/10.1190/1.3553003

Crook, N., Binley, A., Knight, R., Robinson, D. A., Zarnetske, J., & Haggerty, R. (2008). Electrical resistivity imaging of the architecture of substream sediments. *Water Resources Research*, *46*(4), 1–11. https://doi.org/10.1029/2008WR006968

Dara, R., Kettridge, N., Rivett, M. O., Krause, S., & Gomez-Ortiz, D. (2019). Identification of floodplain and riverbed sediment heterogeneity in a meandering UK lowland stream by ground penetrating radar. *Journal of Applied Geophysics*, *171*, 103863. https://doi.org/10.1016/j.jappgeo.2019.103863

Duvillard, P. A., Revil, A., Qi, Y., Soueid Ahmed, A., Coperey, A., & Ravanel, L. (2018). Three-Dimensional Electrical Conductivity and Induced Polarization Tomography of a Rock Glacier. *Journal of Geophysical Research: Solid Earth*, *123*(11), 9528–9554. https://doi.org/10.1029/2018JB015965

Earon, R., Riml, J., Wu, L., & Olofsson, B. (2020). Insight into the influence of local streambed heterogeneity on hyporheic-zone flow characteristics. *Hydrogeology Journal*, *28*(8), 2697–

2712. https://doi.org/10.1007/s10040-020-02244-5

Environment and Climate Change Canada, 2021. 1981-2010 Climate Normals & Averages [WWW Document]. URL http://climate.weather.gc.ca/climate_ normals/index_e.html (accessed 8.30.21).

Gordon, R. P., Lautz, L. K., Briggs, M. A., & McKenzie, J. M. (2012). Automated calculation of vertical pore-water flux from field temperature time series using the VFLUX method and computer program. *Journal of Hydrology*, *420–421*, 142–158. https://doi.org/10.1016/j.jhydrol.2011.11.053

Irvine, D. J., Kurylyk, B. L., & Briggs, M. A. (2020). Quantitative guidance for efficient vertical flow measurements at the sediment–water interface using temperature–depth profiles. *Hydrological Processes*, *34*(3), 649–661. https://doi.org/10.1002/hyp.13614

Irvine, D. J., & Lautz, L. K. (2015). High resolution mapping of hyporheic fluxes using streambed temperatures: Recommendations and limitations. *Journal of Hydrology*, *524*, 137–146. https://doi.org/10.1016/j.jhydrol.2015.02.030

Jarvie, H. P., Johnson, L. T., Sharpley, A. N., Smith, D. R., Baker, D. B., Bruulsema, T. W., & Confesor, R. (2017). Increased Soluble Phosphorus Loads to Lake Erie: Unintended Consequences of Conservation Practices. *Journal of Environmental Quality*, *46*(1), 123–132. https://doi.org/10.2134/jeq2016.07.0248

Kiberu, J. (2002). Induced polarization and Resistivity measurements on a suite of near surface soil samples and their empirical relationship to selected measured engineering parameters. *Interntional Institute for Geo-Information Science and Earth Observation Enschede, The Netherlands*, 119.

Kim, J.H., 2016. DC_2DPro: User's Manual. Geoelectric Imaging Laboratory: Korea Institute of Geoscience and Mineral Resources, Daejeon, South Korea.

Kurylyk, B. L., Irvine, D. J., Carey, S. K., Briggs, M. A., Werkema, D. D., & Bonham, M. (2017). Heat as a groundwater tracer in shallow and deep heterogeneous media: Analytical solution, spreadsheet tool, and field applications. *Hydrological Processes*, *31*(14), 2648–

2661. https://doi.org/10.1002/hyp.11216

Loke M. H. (2015). 2-D and 3-D Electrical Imaging Surveys. *Tutorial*, *May*, 51–52.

Nivorlis, A., 2017. Processing and Modeling of Induced Polarization Data. Masters Thesis. Aristotle University of Thessaloniki, Thessaloniki, Greece (January 2017).

Maurya, P. K., Balbarini, N., Møller, I., Rønde, V., Christiansen, A. V., Bjerg, P. L., Auken, E., & Fiandaca, G. (2018). Subsurface imaging of water electrical conductivity, hydraulic permeability and lithology at contaminated sites by induced polarization. *Geophysical Journal International*, *213*(2), 770–785. https://doi.org/10.1093/gji/ggy018

Moradifam, A., Nachman, A., & Tamasan, A. (2012). Conductivity imaging from one interior measurement in the presence of perfectly conducting and insulating inclusions. *SIAM Journal on Mathematical Analysis*, *44*(6), 3969–3990. https://doi.org/10.1137/120866701

Power, C., Tsourlos, P., Ramasamy, M., Nivorlis, A., & Mkandawire, M. (2018). Combined DC resistivity and induced polarization (DC-IP) for mapping the internal composition of a mine waste rock pile in Nova Scotia, Canada. *Journal of Applied Geophysics*, *150*, 40–51. https://doi.org/10.1016/j.jappgeo.2018.01.009

Rau, G. C., Andersen, M. S., McCallum, A. M., & Acworth, R. I. (2010). Analytical methods that use natural heat as a tracer to quantify surface water-groundwater exchange, evaluated using field temperature records. *Hydrogeology Journal*, *18*(5), 1093–1110. https://doi.org/10.1007/s10040-010-0586-0

Rosenberry, D. O., and J. W. LaBaugh (2008), Field techniques for estimating water fluxes between surface water and ground water, U.S. Geological Survey Techniques and Methods 4-D2, 128 pp, U.S. Geological Survey

Schmidt, C., Conant, B., Bayer-Raich, M., & Schirmer, M. (2007). Evaluation and field-scale application of an analytical method to quantify groundwater discharge using mapped streambed temperatures. *Journal of Hydrology*, *347*(3–4), 292–307. https://doi.org/10.1016/j.jhydrol.2007.08.022

Slater, L. D., & Lesmes, D. (2002). IP interpretation in environmental investigations. *Geophysics*, *67*(1), 77–88. https://doi.org/10.1190/1.1451353

Smits, K. M., Sakaki, T., Limsuwat, A., & Illangasekare, T. H. (2010). Thermal Conductivity of Sands under Varying Moisture and Porosity in Drainage–Wetting Cycles. *Vadose Zone Journal*, *9*(1), 172–180. https://doi.org/10.2136/vzj2009.0095

Sophocleous, M. (2002). Interactions between groundwater and surface water: The state of the science. *Hydrogeology Journal*, *10*(1), 52–67. https://doi.org/10.1007/s10040-001-0170-8

Soupios, P., & Kokinou, E. (2017). *Environmental geophysics: Techniques, advantages and limitations*. *February 2016*.

Stonestrom, D., & Constantz, J. (2003). Heat as a tracer to determine streambed water exchanges. *Water Resources Research*, *44*(4). https://doi.org/10.1029/2008WR006996

Tarnawski, V. R., Momose, T., & Leong, W. H. (2011). Thermal conductivity of standard sands II. Saturated conditions. *International Journal of Thermophysics*, *32*(5), 984–1005. https://doi.org/10.1007/s10765-011-0975-1

Woessner, W. W. (2000). Stream and Fluvial Plain Ground Water Interactions: Rescaling Hydrogeologic Thought. *Ground Water*, *38*(3), 423–429. https://doi.org/10.1111/j.1745-6584.2000.tb00228.x

Yatini, Y., Santoso, D., Laesanpura, A., & Sulistijo, B. (2018). Physical Modeling on Time Domain Induced Polarization (TDIP) Response of Metal Mineral Content. *Indonesian Journal of Applied Physics*, *8*(2), 57. https://doi.org/10.13057/ijap.v8i1.20648

Wang, C., Briggs, M. A., Day-Lewis, F. D., & Slater, L. D. (2021). Characterizing Physical Properties of Streambed Interface Sediments Using In Situ Complex Electrical Conductivity Measurements. *Water Resources Research*, *57*(2), 1–19. https://doi.org/10.1029/2020WR027995

Winter, T. C., LaBaugh, J. W., & Rosenberry, D. O. (1988). *The design and use of a hydraulic potentiomanometer direct measurement of differences in hydraulic head between groundwater and surface water*. *33*(5), 1209–1214.

4 SUMMARY AND CONCLUSIONS

4.1 SUMMARY

Accurate characterization of groundwater-surface water interactions is a crucial aspect in investigations pertaining to geology, hydrology, ecology, hydrogeology, geochemistry, and more. To determine the potential impacts that may be caused from GW-SW interactions, understanding the spatial and temporal variations in streambed heterogeneities and exchange fluxes is paramount. It is understood that exchange fluxes can impact the water quantity, quality and overall health of ecosystems within a GW-SW system (Dahl et al., 2007; Fleckenstein et al., 2010; Winter, 1999). Identifying and understanding the flow processes can aide in understanding the biogeochemical processes and biological processes present in various scales (Brunke & Gonser, 1997; Conant et al., 2019; Stefan Krause et al., 2017). Traditional hydrogeological techniques are often invasive, causing disturbances in the system, as well as potentially creating or affecting preferential flow paths. Furthermore, many techniques suffer from low sampling density. This results in the true spatial heterogeneity to be inaccurately characterized on a stream reach scale.

The goal of this thesis was to evaluate the potential of 3D DC resistivity and induced polarization (DC-IP) for complete characterization of streambed structural heterogeneities at a localized scale with high sampling resolution, and how this methodology can be used in contingence with traditional hydrogeological methods to improve the understanding of stream water-groundwater interactions at complex field sites.

As part of the research goal, three specific objectives were addressed. The *first* objective was to conduct a 3D DC-IP survey of the stream. A depth of investigation up to 1.5 m below the streambed was achieved, with surface area coverage of 47.8 m x 1.8 m. An additional 3D DC-IP survey was also conducted in the adjacent riparian zones, with a span of 48 m, intersecting through the stream. All surveys were successfully conducted and interpreted for characterizations of the intense spatial heterogeneities that exist in the subsurface. Consistencies between surveys were appropriately noted, adding confidence to the collection of raw data, as well as the interpretation of the inverted data. It was noted that the different survey types, using both DC and IP, added valuable information in regard to the composition sediments and the spatial distribution both laterally and vertically.

The *second* objective was to use traditional hydrogeological approaches to assess GW-SW exchanges. This was successfully completed through vertical head difference measurements, spatial temperature-mapping, sediment coring and grain size analysis, and the quantification of exchange fluxes with temperature-depth profiles. The preceding DC-IP surveys were also used to optimize the selection of sampling locations, showcasing the benefit of geophysical imaging as an early screening tool too. While the hydrogeological techniques provide limited spatial resolution, they still provide valuable information regarding stream reach characteristics and to help validate the information gather from the geophysical surveys. The improved characterization of the streambed with this integrated hydrogeological-geophysical approach was also used to enhance the selection of thermal properties for the temperature flux modeling performed to determine the temporal patterns in GW-SW exchanges. Therefore, while DC-IP directly improved spatial characterization of streambed composition, it can also indirectly improve analysis of associated GW-SW exchanges.

The *third* objective was to assess the connection between objectives 1 and 2. This objective was done throughout the entirety of the study as objectives 1 and 2 were closely interconnected. Initial interpretations of geophysical methods allowed for a preliminary characterization of the field site in relation to the expected GW-SW exchanges. As more traditional hydrogeological techniques were performed and more information was gathered, connections between traditional and geophysical methods were continuously made.

4.2 RECOMMENDATIONS

Chapter 3 evaluated how various traditional approaches were used at the field site in Kintore, Ontario, to evaluate high-resolution DC-IP imaging of streambed composition, and how it influences GW-SW exchange interactions. The following recommendations are suggested for improving the accuracy and detail of such characterizations, to improve overall understanding.

- High resolution DC-IP surveys were conducted during the summer of 2020. While this was sufficient to assess streambed heterogeneity, periodic surveys could have been performed to provide time-lapse monitoring of temporal variabilities in shallow streambed sediments and their connectivity to seasonal GW-SW interactions.

- The stream reach evaluated in the investigation was chosen with a partnered objective of evaluating phosphorus flux dynamics and periphyton abundance in the stream. Thorough analysis of that partner study can be evaluated.

- The spacing within the instrumentation used for temperature-depth profiling was decided upon using literature studies and therefore was not considered based on the model used to quantify the fluxes (Flux-LM).

4.3 REFERENCES

Brunke, M., & Gonser, T. (1997). The ecological significance of exchange processes between rivers and groundwater. *Freshwater Biology*, *37*(1), 1–33. https://doi.org/10.1046/j.1365-2427.1997.00143.x

Conant, B., Robinson, C. E., Hinton, M. J., & Russell, H. A. J. (2019). A framework for conceptualizing groundwater-surface water interactions and identifying potential impacts on water quality, water quantity, and ecosystems. *Journal of Hydrology*, *574*(March), 609–627. https://doi.org/10.1016/j.jhydrol.2019.04.050

Dahl, M., Nilsson, B., Langhoff, J. H., & Refsgaard, J. C. (2007). Review of classification systems and new multi-scale typology of groundwater-surface water interaction. *Journal of Hydrology*, *344*(1–2), 1–16. https://doi.org/10.1016/j.jhydrol.2007.06.027

Fleckenstein, J. H., Krause, S., Hannah, D. M., & Boano, F. (2010). Groundwater-surface water interactions: New methods and models to improve understanding of processes and dynamics. *Advances in Water Resources*, *33*(11), 1291–1295. https://doi.org/10.1016/j.advwatres.2010.09.011

Krause, S., Lewandowski, J., Grimm, N. B., Hannah, D. M., Pinay, G., McDonald, K., Martí, E., Argerich, A., Pfister, L., Klaus, J., Battin, T., Larned, S. T., Schelker, J., Fleckenstein, J., Schmidt, C., Rivett, M. O., Watts, G., Sabater, F., Sorolla, A., & Turk, V. (2017). Ecohydrological interfaces as hot spots of ecosystem processes. *Water Resources Research*, *53*(8), 6359–6376. https://doi.org/10.1002/2016WR019516

Winter, T. C., Harvey, J. W., & Alley, W. M. (1998). *Ground water and surface water a single resource: U* (Issue May). https://doi.org/10.3133/cir1139

APPENDIX A: ADDITIONAL MATERIAL FOR MONITORING GW-SW EXCHANGES

Appendix A presents additional results from spatial streambed temperature mapping, temperature-depth profiles and exchange flux calculations and errors.

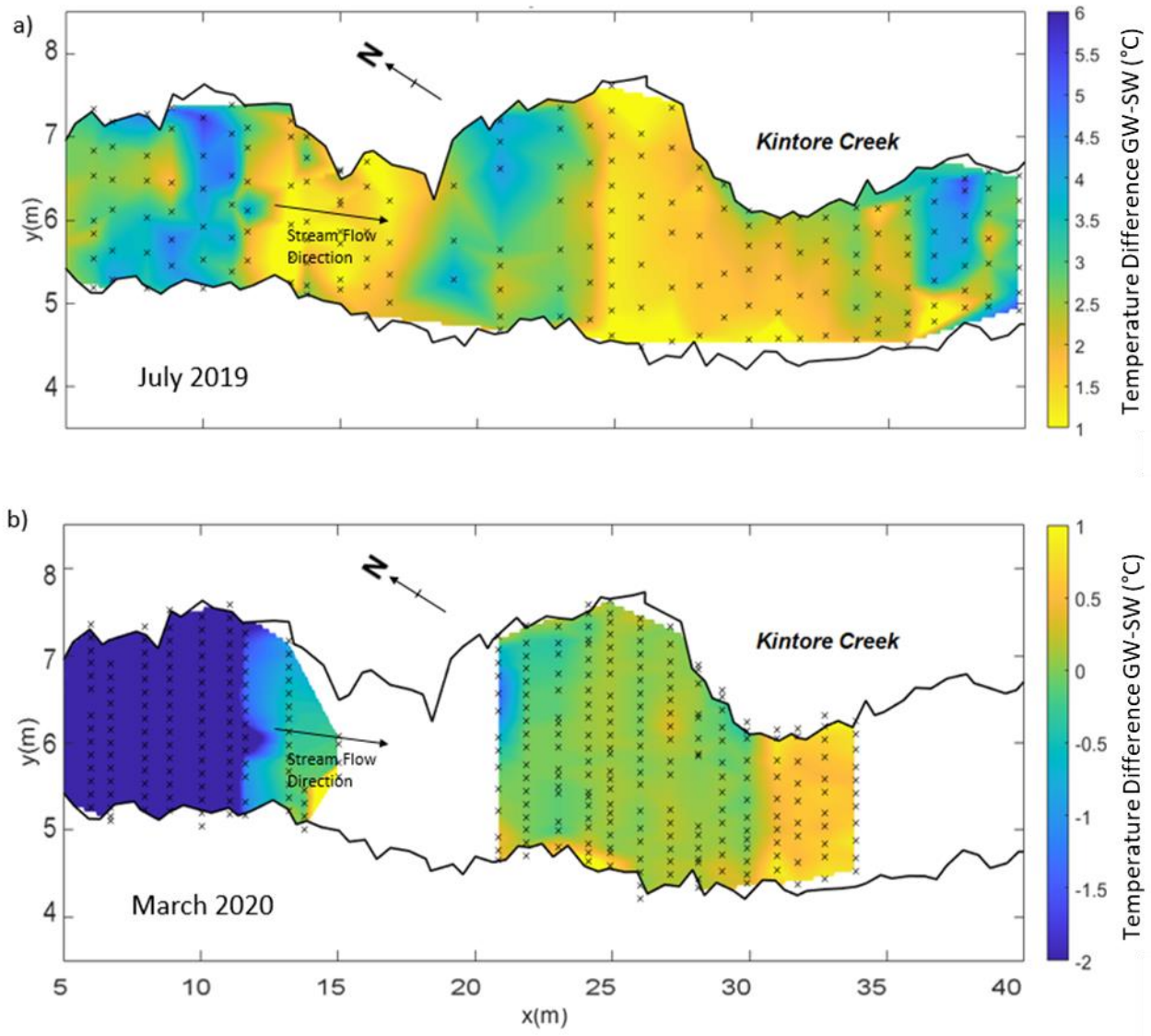

Figure A-1: Spatial maps of temperature difference between groundwater and surface water during (a) summer baseflow conditions, and (b) winter baseflow conditions (note the different colour scales). The location of each temperature measurement is indicated by a black 'x'. Stream outline based on summer (low-flow) conditions; the stream width extended beyond this in places during the winter assessment.

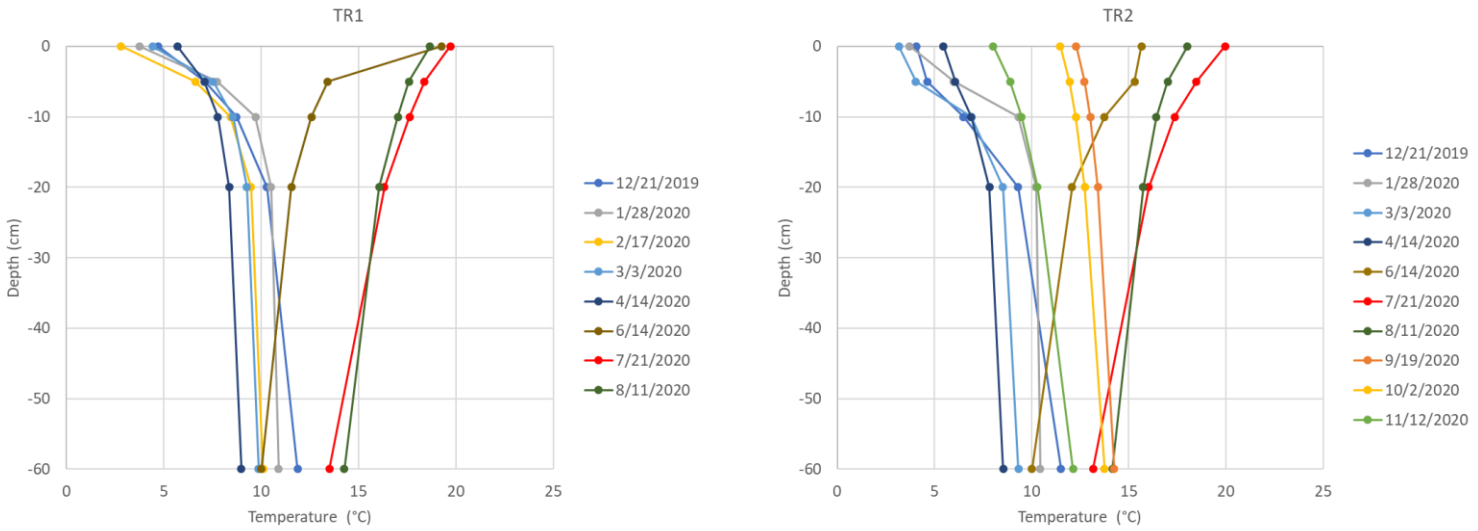

Figure A-2: Temperature versus depth profiles at (TR1, and TR2 over a year of collected data. Dates omitted are due to instrumental error.

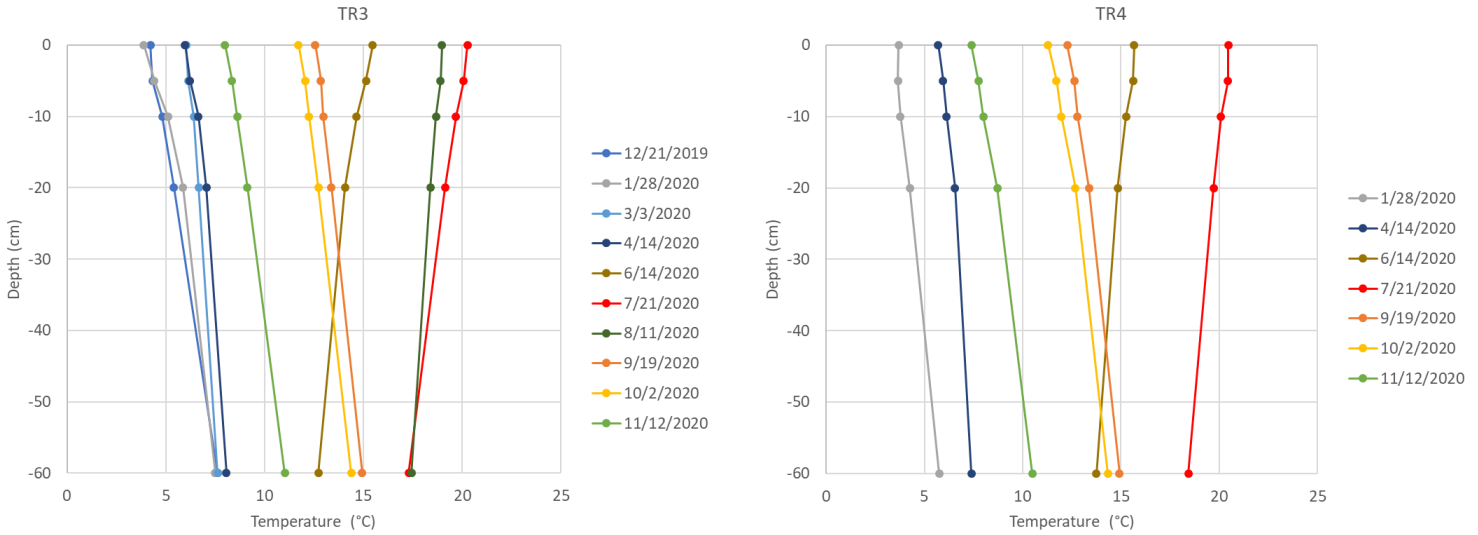

Figure A-3: Temperature versus depth profiles at TR3, and TR4 over a year of collected data. Dates omitted are due to instrumental error.

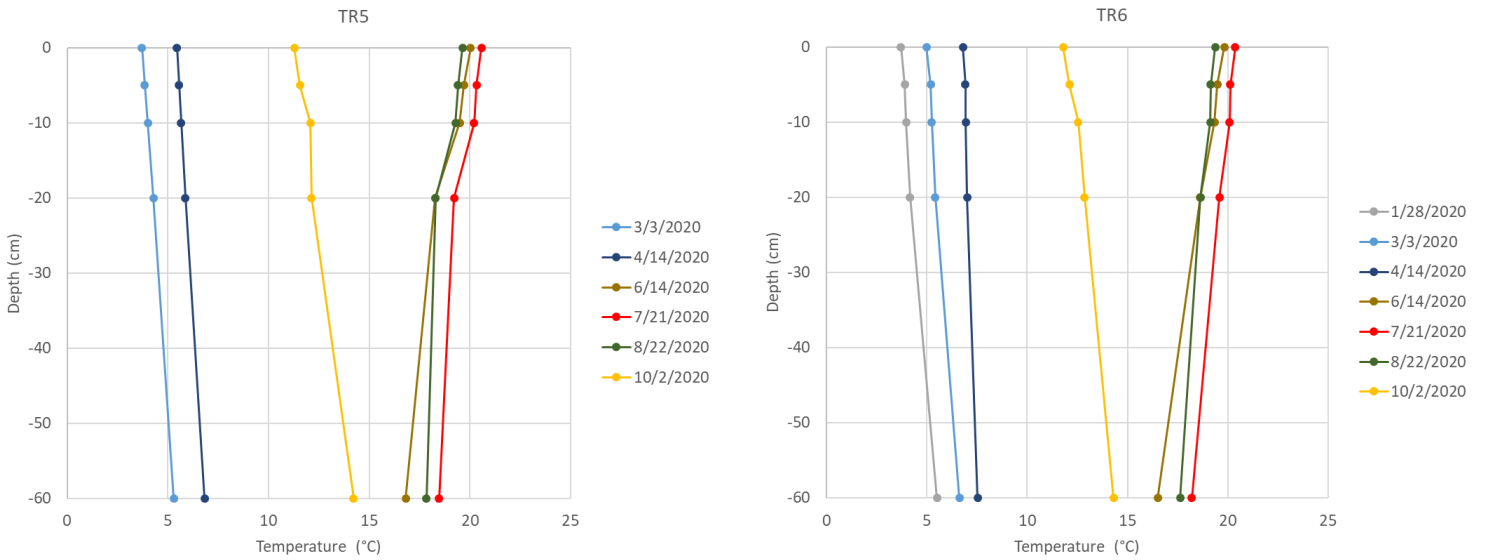

Figure A-4: Temperature versus depth profiles at TR5, and TR6 over a year of collected data. Dates omitted are due to instrumental error.

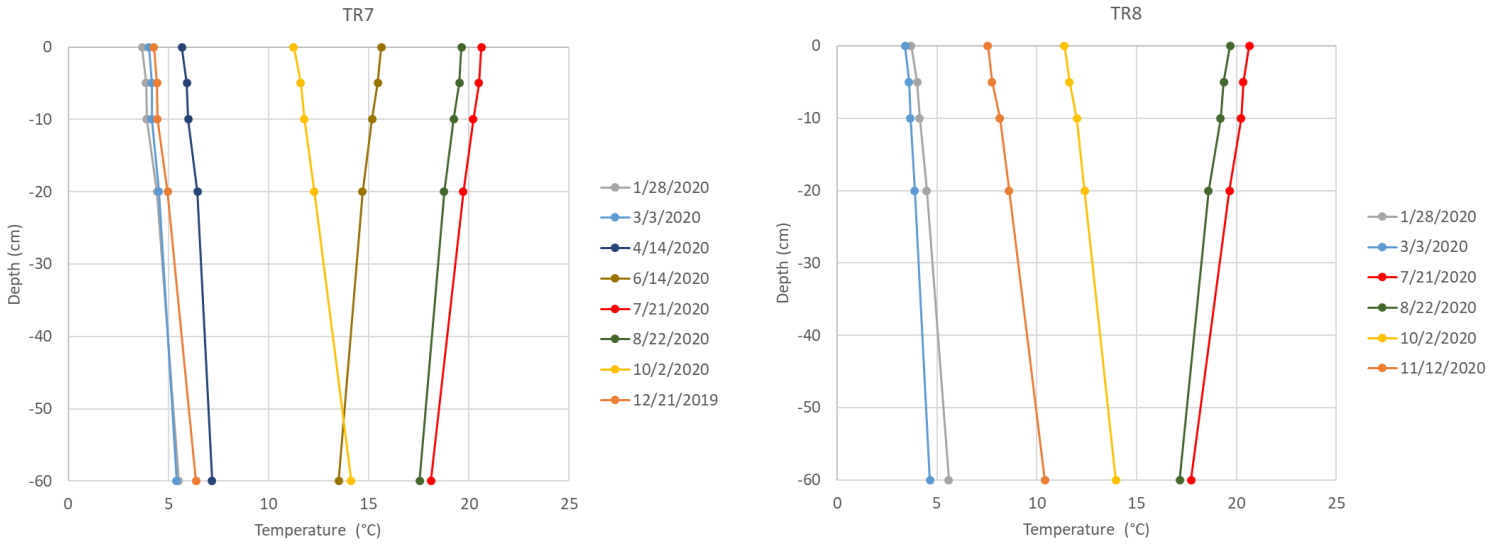

Figure A-5: Temperature versus depth profiles at TR7, and TR8 over a year of collected data. Dates omitted are due to instrumental error.

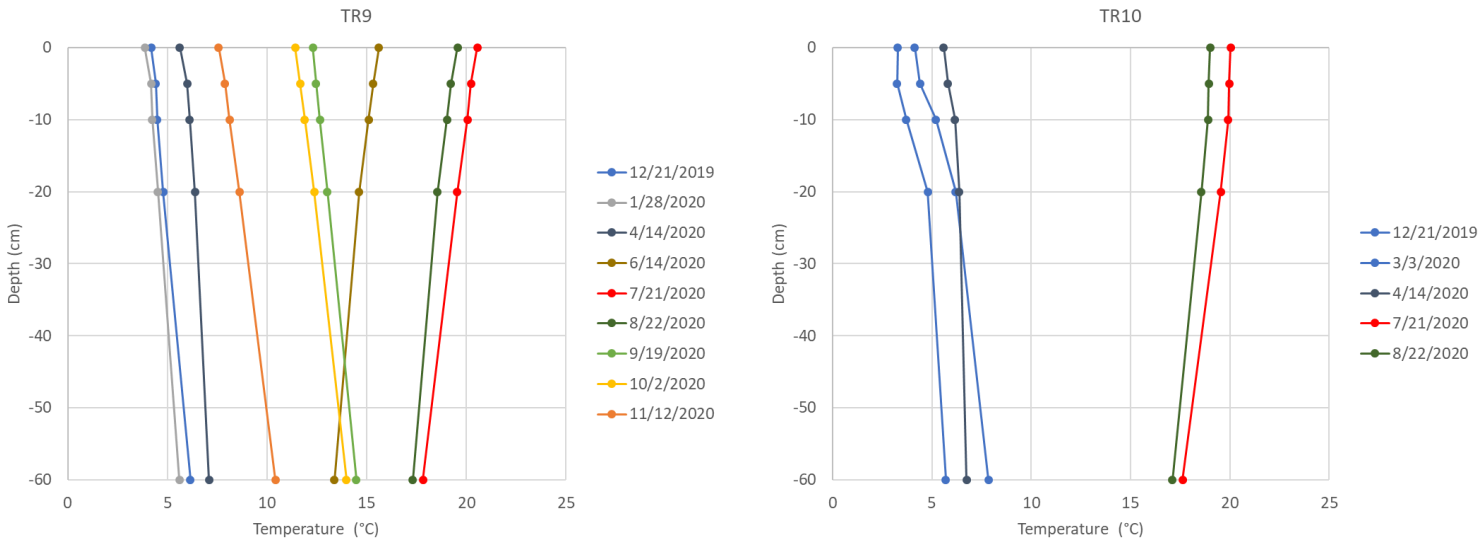

Figure A-6: Temperature versus depth profiles at TR9, and TR10 over a year of collected data. Dates omitted are due to instrumental error.

TR		1						2					
Parameter		Flux (m/yr)			RMSE (°C)			Flux (m/yr)			RMSE (°C)		
Measuring Period		Model			Model			Model			Model		
Start	End	1	2	3	1	2	3	1	2	3	1	2	3
12/21/2019	12/27/2019	-240.50	-241.45	-242.83	0.079	0.077	0.043	-122.57	-	-97.86	0.543	-	0.122
12/29/2019	1/4/2020	-230.21	-231.26	-232.43	0.123	0.121	0.088	-82.46	-	-63.09	0.787	-	0.670
1/28/2020	2/2/2020	-511.55	-511.57	-512.44	0.097	0.097	0.085	-394.36	-	-357.19	0.543	-	0.419
2/17/2020	2/21/2020	-441.44	-441.49	-442.82	0.102	0.102	0.079	-412.44	-	-376.25	0.242	-	0.133
3/3/2020	3/7/2020	-456.64	-456.65	-457.19	0.185	0.185	0.171	-234.66	-	-203.95	0.574	-	0.457
3/23/2020	3/27/2020	-432.17	-432.22	-433.36	0.076	0.075	0.064	-166.19	-	-139.74	0.270	-	0.207
4/14/2020	4/17/2020	-300.56	-300.96	-302.95	0.085	0.085	0.072	-183.59	-	-154.98	0.121	-	0.062
4/21/2020	4/26/2020	-257.05	-257.74	-259.40	0.081	0.081	0.072	-156.29	-	-129.38	0.039	-	0.002
6/14/2020	6/18/2020	-113.74	-460.60	-459.60	0.687	0.687	0.667	-106.76	-	-85.09	0.335	-	0.247
6/24/2020	6/27/2020	-60.70	-246.55	-248.15	0.455	0.454	0.427	-130.28	-	-105.91	0.209	-	0.111
7/21/2020	7/27/2020	-104.13	-107.79	-103.06	0.114	0.110	0.096	-122.42	-	-97.60	0.114	-	0.225
8/11/2020	8/15/2020	-128.01	-130.99	-127.88	0.094	0.091	0.081	-137.59	-	-111.22	0.123	-	0.189
8/22/2020	8/25/2020	-101.40	-105.14	-100.18	0.071	0.068	0.061	-109.96	-	-86.03	0.082	-	0.145
9/19/2020	9/23/2020	-	-	-	-	-	-	-117.19	-	-92.75	0.033	-	0.065
10/2/2020	10/5/2020	-	-	-	-	-	-	-107.84	-	-84.13	0.036	-	0.073
10/17/2020	10/21/2020	-	-	-	-	-	-	-99.96	-	-76.77	0.045	-	0.081
10/26/2020	10/29/2020	-	-	-	-	-	-	-119.98	-	-95.07	0.079	-	0.130
11/12/2020	11/17/2020	-	-	-	-	-	-	-107.91	-	-84.14	0.074	-	0.141
11/22/2020	11/25/2020	-	-	-	-	-	-	-109.72	-	-85.75	0.105	-	0.192
12/16/2020	12/22/2020	-229.04	-230.01	-231.47	0.151	0.158	0.123	-169.82	-	-138.88	0.229	-	0.279
1/3/2021	1/7/2021	-254.75	-255.25	-257.63	0.106	0.104	0.096	-193.57	-	-161.13	0.168	-	0.214
1/29/2021	2/5/2021	-224.03	-224.98	-226.55	0.157	0.164	0.146	-258.65	-	-224.11	0.203	-	0.267
2/17/2021	2/24/2021	-210.98	-212.02	-213.39	0.148	0.154	0.113	-197.92	-	-165.34	0.177	-	0.226
2/26/2021	3/4/2021	-145.03	-146.86	-146.35	0.058	0.056	0.059	-208.88	-	-176.11	0.171	-	0.229
3/12/2021	3/16/2021	-245.12	-245.94	-247.85	0.281	0.283	0.293	-	-	-	-	-	-

Figure A-7: Exchange flux [m/year] and RMSE [°C] results for Model 1 (Surficial interpretation), Model 2 (Geophysical Interpretation) and Model 3 (Soil Core) for TR1 and TR2.

TR		3						4					
Parameter		Flux (m/yr) Model			RMSE (°C) Model			Flux (m/yr) Model			RMSE (°C) Model		
Measuring Period													
Start	End	1	2	3	1	2	3	1	2	3	1	2	3
12/21/2019	12/27/2019	-0.89	8.04	-10.03	0.088	0.085	0.088	-	-	-	-	-	-
12/29/2019	1/4/2020	-12.09	-2.62	-20.42	0.097	0.094	0.097	-	-	-	-	-	-
1/28/2020	2/2/2020	-89.50	-75.68	-92.89	0.051	0.051	0.054	57.12	34.96	42.05	0.098	0.102	0.097
2/17/2020	2/21/2020	-74.00	-61.14	-78.22	0.049	0.050	0.053	41.73	21.23	28.35	0.127	0.132	0.125
3/3/2020	3/7/2020	-29.46	-19.12	-36.44	0.040	0.040	0.041	-	-	-	-	-	-
3/23/2020	3/27/2020	-56.09	-44.31	-61.35	0.042	0.042	0.043	-	-	-	-	-	-
4/14/2020	4/17/2020	-75.74	-62.78	-79.88	0.043	0.043	0.044	-68.54	-78.77	-70.74	0.020	0.023	0.020
4/21/2020	4/26/2020	-24.95	-14.85	-32.24	0.040	0.040	0.040	-	-	-	-	-	-
6/14/2020	6/18/2020	-70.03	-57.41	-74.52	0.035	0.034	0.036	-29.30	-42.81	-35.40	0.074	0.078	0.070
6/24/2020	6/27/2020	-56.65	-44.83	-61.84	0.039	0.043	0.042	-24.77	-38.69	-27.67	0.113	0.117	0.115
7/21/2020	7/27/2020	-16.79	-7.09	-24.74	0.043	0.041	0.043	-6.80	-22.38	-15.05	0.077	0.080	0.074
8/11/2020	8/15/2020	-12.10	-2.63	-20.41	0.040	0.039	0.040	-	-	-	-	-	-
8/22/2020	8/25/2020	-45.86	-34.62	-51.86	0.042	0.040	0.042	-31.19	-44.53	-37.25	0.095	0.098	0.092
9/19/2020	9/23/2020	-6.11	3.09	-14.76	0.028	0.031	0.029	-33.02	-46.18	-38.33	0.041	0.042	0.043
10/2/2020	10/5/2020	-21.77	-11.81	-29.29	0.031	0.034	0.032	-51.92	-63.46	-55.51	0.039	0.041	0.042
10/17/2020	10/21/2020	-1.85	7.15	-10.80	0.031	0.034	0.032	-33.96	-47.04	-39.19	0.037	0.038	0.039
10/26/2020	10/29/2020	-15.23	-5.59	-23.19	0.030	0.033	0.031	-40.26	-52.80	-44.95	0.035	0.039	0.036
11/12/2020	11/17/2020	-21.09	-11.17	-28.65	0.024	0.028	0.026	-35.85	-48.77	-40.99	0.035	0.041	0.034
11/22/2020	11/25/2020	-19.67	-9.82	-27.33	0.029	0.035	0.032	-19.47	-33.87	-26.24	0.060	0.069	0.056
12/16/2020	12/22/2020	-58.86	-48.22	-59.35	0.098	0.098	0.113	-13.06	-25.11	-20.91	0.119	0.110	0.117
1/3/2021	1/7/2021	-96.62	-83.52	-95.49	0.113	0.121	0.125	-8.42	-20.69	-16.58	0.048	0.049	0.046
1/29/2021	2/5/2021	-66.39	-55.27	-66.51	0.097	0.099	0.112	-3.20	-16.30	-12.23	0.141	0.130	0.140
2/17/2021	2/24/2021	-41.97	-32.35	-43.35	0.085	0.087	0.096	2.30	-11.27	-7.30	0.128	0.117	0.127
2/26/2021	3/4/2021	-48.27	-38.25	-49.38	0.078	0.083	0.088	-9.21	-21.56	-17.39	0.077	0.068	0.076
3/12/2021	3/16/2021	-102.92	-89.31	-49.38	0.069	0.073	0.088	-45.34	-54.68	-49.82	0.083	0.071	0.081

Figure A-8: Exchange flux [m/year] and RMSE [°C] results for Model 1 (Surficial interpretation), Model 2 (Geophysical Interpretation) and Model 3 (Soil Core) for TR3 and TR4.

TR		5						6					
Parameter		Flux (m/yr)			RMSE (°C)			Flux (m/yr)			RMSE (°C)		
Measuring Period		Model			Model			Model			Model		
Start	End	1	2	3	1	2	3	1	2	3	1	2	3
12/21/2019	12/27/2019	-	-	-	-	-	-	-	-	-	-	-	-
12/29/2019	1/4/2020	-	-	-	-	-	-	-	-	-	-	-	-
1/28/2020	2/2/2020	-	-	-	-	-	-	15.45	42.62	30.89	0.044	0.052	0.048
2/17/2020	2/21/2020	-	-	-	-	-	-	-1.25	22.14	12.01	0.040	0.052	0.047
3/3/2020	3/7/2020	-11.19	-11.19	-8.37	0.039	0.023	0.031	13.31	40.02	28.48	0.048	0.055	0.052
3/23/2020	3/27/2020	-	-	-	-	-	-	-	-	-	-	-	-
4/14/2020	4/17/2020	11.19	11.19	28.61	0.030	0.031	0.030	0.04	23.82	13.51	0.033	0.037	0.035
4/21/2020	4/26/2020	-	-	-	-	-	-	-	-	-	-	-	-
6/14/2020	6/18/2020	-45.12	-45.12	-33.91	0.173	0.185	0.164	-4.56	18.10	8.29	0.055	0.049	0.051
6/24/2020	6/27/2020	-45.88	-45.88	-34.78	0.180	0.193	0.169	-27.06	-8.79	-16.76	0.016	0.031	0.024
7/21/2020	7/27/2020	-63.75	-63.75	-54.13	0.167	0.175	0.162	-1.67	21.59	11.52	0.052	0.048	0.050
8/11/2020	8/15/2020	-	-	-	-	-	-	-	-	-	-	-	-
8/22/2020	8/25/2020	-87.32	-87.32	-79.43	0.186	0.195	0.183	-16.98	3.24	-5.55	0.058	0.054	0.056
9/19/2020	9/23/2020	-	-	-	-	-	-	-25.45	-6.95	-15.02	0.069	0.078	0.074
10/2/2020	10/5/2020	-5.63	-5.63	9.72	0.144	0.136	0.151	-34.69	-17.85	-25.21	0.070	0.080	0.075
10/17/2020	10/21/2020	-	-	-	0.000	0.000	0.000	-22.91	-3.95	-12.21	0.076	0.085	0.081
10/26/2020	10/29/2020	12.55	12.55	30.23	0.137	0.131	0.143	-29.86	-12.18	-19.90	0.078	0.089	0.084
11/12/2020	11/17/2020	-	-	-	0.000	0.000	0.000	-28.51	-10.61	-18.43	0.111	0.123	0.117
11/22/2020	11/25/2020	-	-	-	-	-	-	-24.65	-5.99	-14.13	0.086	0.102	0.095
12/16/2020	12/22/2020	-22.13	-22.13	-10.84	0.100	0.108	0.113	-18.46	-3.56	-6.23	0.124	0.165	0.123
1/3/2021	1/7/2021	-26.73	-26.73	-15.78	0.106	0.111	0.115	-22.01	-7.71	-10.13	0.106	0.133	0.106
1/29/2021	2/5/2021	-18.03	-18.03	-6.40	0.061	0.068	0.071	-16.16	-0.96	-3.78	0.084	0.119	0.085
2/17/2021	2/24/2021	-17.16	-17.16	-5.43	0.068	0.075	0.079	-12.27	3.62	0.71	0.092	0.126	0.092
2/26/2021	3/4/2021	-20.98	-20.98	-9.56	0.090	0.096	0.101	-14.78	0.73	-2.02	0.100	0.129	0.099
3/12/2021	3/16/2021	-22.33	-22.33	-10.96	0.087	0.093	0.095	-14.18	1.32	-1.51	0.064	0.085	0.066

Figure A-9: Exchange flux [m/year] and RMSE [°C] results for Model 1 (Surficial interpretation), Model 2 (Geophysical Interpretation) and Model 3 (Soil Core) for TR5 and TR6.

TR		7						8					
Parameter		Flux (m/yr)			RMSE (°C)			Flux (m/yr)			RMSE (°C)		
Measuring Period		Model			Model			Model			Model		
Start	End	1	2	3	1	2	3	1	2	3	1	2	3
12/21/2019	12/27/2019	14.64	22.15	12.18	0.067	0.063	0.066	-	-	-	-	-	-
12/29/2019	1/4/2020	-22.33	-16.17	-24.05	0.065	0.060	0.064	-	-	-	-	-	-
1/28/2020	2/2/2020	-12.41	-5.91	-14.32	0.059	0.055	0.058	-35.30	-30.40	-31.85	0.039	0.040	0.052
2/17/2020	2/21/2020	-23.50	-17.38	-25.20	0.063	0.058	0.062	-41.32	-36.65	-37.49	0.038	0.040	0.058
3/3/2020	3/7/2020	3.04	10.13	0.83	0.046	0.044	0.045	-27.33	-22.13	-24.27	0.033	0.034	0.043
3/23/2020	3/27/2020	-	-	-	-	-	-	-	-	-	-	-	-
4/14/2020	4/17/2020	-56.86	-51.80	-57.98	0.046	0.043	0.045	-79.44	-76.04	-73.28	0.024	0.025	0.037
4/21/2020	4/26/2020	-	-	-	-	-	-	-	-	-	-	-	-
6/14/2020	6/18/2020	-35.09	-29.35	-36.56	0.039	0.034	0.038	-	-	-	-	-	-
6/24/2020	6/27/2020	-9.62	-2.93	-11.53	0.030	0.031	0.030	-	-	-	-	-	-
7/21/2020	7/27/2020	-2.80	4.09	-4.88	0.044	0.039	0.043	-0.20	6.11	0.29	0.042	0.042	0.039
8/11/2020	8/15/2020	-	-	-	-	-	-	15.83	22.86	15.00	0.037	0.037	0.034
8/22/2020	8/25/2020	-21.71	-15.53	-23.44	0.053	0.049	0.053	-29.35	-24.22	-26.78	0.040	0.039	0.032
9/19/2020	9/23/2020	9.78	17.30	7.50	0.052	0.054	0.052	-6.70	-0.67	-5.55	0.034	0.035	0.042
10/2/2020	10/5/2020	-10.78	-4.10	-12.66	0.035	0.039	0.035	-27.41	-22.22	-24.72	0.036	0.037	0.052
10/17/2020	10/21/2020	-	-	-	0.000	0.000	0.000	-3.17	3.01	-2.19	0.039	0.040	0.048
10/26/2020	10/29/2020	-	-	-	0.000	0.000	0.000	-10.86	-5.00	-9.45	0.033	0.033	0.043
11/12/2020	11/17/2020	-	-	-	0.000	0.000	0.000	-16.24	-10.60	-14.46	0.035	0.035	0.045
11/22/2020	11/25/2020	-	-	-	-	-	-	-7.46	-1.46	-6.36	0.037	0.036	0.046
12/16/2020	12/22/2020	-	-	-	-	-	-	50.27	58.16	50.80	0.208	0.212	0.196
1/3/2021	1/7/2021	-	-	-	-	-	-	20.96	27.38	23.21	0.145	0.150	0.136
1/29/2021	2/5/2021	-	-	-	-	-	-	34.86	41.96	36.43	0.178	0.182	0.168
2/17/2021	2/24/2021	-	-	-	-	-	-	0.85	6.41	4.56	0.145	0.148	0.139
2/26/2021	3/4/2021	-29.99	-24.93	-31.14	0.059	0.062	0.057	5.66	11.39	9.15	0.118	0.121	0.113
3/12/2021	3/16/2021	-	-	-	-	-	-	-9.22	-4.14	-4.74	0.105	0.108	0.102

Figure A-10: Exchange flux [m/year] and RMSE [°C] results for Model 1 (Surficial interpretation), Model 2 (Geophysical Interpretation) and Model 3 (Soil Core) for TR7 and TR8.

TR		9						10					
Parameter		Flux (m/yr) Model			RMSE (°C) Model			Flux (m/yr) Model			RMSE (°C) Model		
Measuring Period													
Start	End	1	2	3	1	2	3	1	2	3	1	2	3
12/21/2019	12/27/2019	3.42	13.57	-2.38	0.037	0.036	0.035	-81.12	-84.56	-61.86	0.152	0.154	0.087
12/29/2019	1/4/2020	-27.75	-21.24	-32.92	0.034	0.036	0.033	-112.42	-115.14	-88.26	0.207	0.209	0.125
1/28/2020	2/2/2020	-25.74	-19.35	-31.08	0.059	0.054	0.054	-	-	-	-	-	-
2/17/2020	2/21/2020	-45.69	-41.44	-50.69	0.074	0.065	0.067	-	-	-	-	-	-
3/3/2020	3/7/2020	-	-	-	0.000	0.000	-	-67.77	-71.62	-52.41	0.248	0.250	0.207
3/23/2020	3/27/2020	-	-	-	-	-	-	-	-	-	-	-	-
4/14/2020	4/17/2020	-76.97	-75.76	-81.55	0.060	0.052	0.054	-167.22	-168.85	-134.51	0.048	0.048	0.043
4/21/2020	4/26/2020	-	-	-	-	-	-	-	-	-	-	-	-
6/14/2020	6/18/2020	-35.66	-29.92	-40.66	0.006	0.020	0.015	-	-	-	-	-	-
6/24/2020	6/27/2020	-21.32	-13.74	-26.46	0.037	0.053	0.049	-	-	-	-	-	-
7/21/2020	7/27/2020	-14.01	-5.85	-19.40	0.027	0.031	0.028	78.22	69.37	69.93	0.038	0.040	0.027
8/11/2020	8/15/2020	-2.59	6.99	-8.18	0.022	0.024	0.023	40.23	32.91	38.85	0.042	0.043	0.034
8/22/2020	8/25/2020	-38.25	-32.87	-43.24	0.024	0.028	0.024	59.11	51.05	54.28	0.041	0.042	0.032
9/19/2020	9/23/2020	1.49	11.66	-4.14	0.008	0.019	0.017	-	-	-	-	-	-
10/2/2020	10/5/2020	-12.91	-4.58	-18.30	0.001	0.017	0.013	-	-	-	-	-	-
10/17/2020	10/21/2020	3.92	14.30	-1.81	0.004	0.009	0.006	-	-	-	-	-	-
10/26/2020	10/29/2020	-8.44	0.33	-13.96	0.016	0.015	0.013	-	-	-	-	-	-
11/12/2020	11/17/2020	-12.60	-4.31	-18.03	0.016	0.018	0.014	-	-	-	-	-	-
11/22/2020	11/25/2020	-6.80	2.21	-12.33	0.023	0.027	0.022	-	-	-	-	-	-
12/16/2020	12/22/2020	-7.24	-2.14	-14.17	0.076	0.086	0.000	-	-	-	-	-	-
1/3/2021	1/7/2021	-7.36	-2.48	-14.25	0.048	0.045	0.043	-	-	-	-	-	-
1/29/2021	2/5/2021	-9.76	-4.94	-16.63	0.078	0.088	0.078	-	-	-	-	-	-
2/17/2021	2/24/2021	-22.36	-19.19	-28.98	0.095	0.097	0.092	-	-	-	-	-	-
2/26/2021	3/4/2021	-5.70	-0.38	-12.97	0.101	0.108	0.102	-96.14	-98.94	-72.38	0.142	0.143	0.135
3/12/2021	3/16/2021	-8.21	-3.62	-15.43	0.066	0.068	0.066	-115.98	-118.46	-87.82	0.123	0.122	0.117

Figure A-11: Exchange flux [m/year] and RMSE [°C] results for Model 1 (Surficial interpretation), Model 2 (Geophysical Interpretation) and Model 3 (Soil Core) for TR9 and TR10.

Curriculum Vitae

Name:	Kyle Robinson
Post-secondary Education and Degrees:	The University of Western Ontario London, Ontario, Canada 2014-2019 B.E.Sc. The University of Western Ontario London, Ontario, Canada 2019-2021 M.E.Sc
Honours and Awards:	AER Global Opportunities Award in Environment and Sustainability Studies 2017
Related Work Experience	Graduate Teaching Assistant The University of Western Ontario 2020-2021